UNIVERSITÀ DEGLI STUDI DI PADOVA
FACOLTÀ DI INGEGNERIA

Tesi di Laurea Magistrale in Ingegneria Civile Curriculum Idraulica

Analisi sperimentale sulla probabilità di erosione e di trasporto delle particelle solide in correnti idriche

Particle entrainment, erosion time probability and particle motion

Laureando: **Matteo Cesaro**

Relarote: **Prof. Andrea Marion**
Correlatore: **Prof. Vladimir Nikora**
Correlatore: **Ing. Matthew James Witz**

Anno Accademico 2012/2013

ABSTRACT

Sediment entrainment mechanisms were studied using a high-frequency particle image velocimetry (PIV) measurement system, tracking the motion of a single entrained spherical particle. The experiments were carried out in two sections. The first one deals with the entrainment time in relation to the particles protrusion. The second one is about the particle tracking at the point of entrainment. These tests were developed in flume with a fixed rough bed; spherical particles were used to create the rough bed layer. The two sections were performed with different flow conditions and target particles density. The study aimed to improve the understanding of particle entrainment looking at the influence of some main parameters as protrusion, flow depth, particle density.

Particle's protrusion was set for every combination of flow depth and particle density in order to have three chosen mean times of erosion in each case. The experimental mean erosion time distribution was described theoretically using the exponential probability distribution. Density and the particle's protrusion were found to be very influential in the erosion time probability distribution, noticing the scattering increase for greater mean time of erosion due to the turbulent flow motion.

Particle's tracking was performed by means of particular software to detect particle in the images and producing time-series of the particle position. From these was carried out the particle motion analysis. It looked at trajectories, jumps, velocities and accelerations. It has been found the important role of particle density in the motion and the close relation between particle and flow motion.

ACKNOWLEDGMENT

This thesis has been written with the experimental work made in the University of Aberdeen, I have to thank Prof. Vladimir Nikora, Prof. Andrea Marion, Dr. Nina Nikora and the Erasmus Offices for the opportunity to develop my thesis abroad within LLP-Erasmus. I have also to thank my supervisors Eng. Matthew James Witz and Dr. Mohammad Amir for the help they gave me with this work, and all the people that worked in the Laboratory "Aberdeen Open Channel Facility" and on the PIV system.

Finally I have to express my gratitude to my family that supported me during my time in Aberdeen. A big thanks to all the friends I made during my stay, my "Erasmus Family", for their friendship and patience, and help my English improves. Another big thank to my university mates and all the other friends who supported me so far.

INDEX

LIST OF TABLES

x

LIST OF FIGURES

List of symbols

ρ = fluid density

γ = fluid specific weight

t = time

$\bar{u}$ = velocity vector $[u, v, w]$

$u_i = i^{th}$ variable component

$\bar{u}_i$ = time-averaged variable

$\langle \bar{u}_i \rangle$ = double-averaged variable

$\tilde{u}_i$ = spatial-fluctuation variable

u'_i = time-fluctuation variable

$\bar{a}$ = acceleration vector

p = pressure

ρ_S = grain density

μ = dynamic viscosity coefficient

v = kinematic viscosity coefficient

$i, j = [x, y, z]$ components

div = divergence

ϕ = roughness function

V_f = fluid volume in the spatial averaged volume

V_0 = spatial-averaged volume

S_{int} = roughness-fluid surface interface

n_i = normal component to the surface element dS directed into the fluid

F_D = drag force

F_L = lift force

C_D = drag resistant coefficient

C_L = lift resistant coefficient

A = projected area of the particle

B = width of the flume

d = particle diameter

Π = particle protrusion

e = particle exposure

φ = pivoting angle

R_e = particle Reynolds number

Re_b = bulk Reynolds number

R_e^* = roughness Reynolds number

k_s = roughness height

u^* = shear velocity

τ_0 = shear bed stress

z^* = dimensionless wall unit

k = Von Karman parameter

Fr = Froude number

C_M = mass coefficient

m = mean value

σ = standard deviation

m = particle mass

I_i = Impulse over T_i

T_i = time duration

SF = shape factor

θ = Shields stress

θ_c = Critical Shields stress

U = stream-wise uniform velocity

$\wedge$ = logical AND

1. Introduction

This thesis deals with solid transport and erosion occurring in hydraulic structures, streams, rivers, canals, bridge piers, dams and so on. Erosion is the difference between the entrainment and the deposition. Usually it is caused by water streams and it's one of the most important problems concerning slopes and creeks. It can produce rare and dangerous events of solid transport as debris-flow, but also in ordinary events the erosion of the river's bottom can produce problems of stability in bridge piers and obstruction of dam drainages.

This topic is still not well known due to the complexity of the processes that regulate a particle entrainment, i.e. the motions of a particle form its position on the bed, while in suspension, saltation or rolling. There are many parameters involved in the entrainment like those related to the water steam like the near wall velocity, its profile and fluctuations from the mean value; there are also parameters related to the particles in top bed layer as size, shape, orientation and weight. All these variables can influence the forces of magnitude on the stones in the top bed layer.

The main forces on stones are of either stabilizing or destabilizing nature in relation to the motion of the particles. The flow creates destabilizing forces as drag and lift forces that can reach extreme values due to the flow fluctuations. On the other hand the stabilizing forces are developed by the particles from the top bed layer as the stone's own weight, boundary constraints due to nearby stones and shear stress.

This research project is focused on the analysis of particle entrainment in a turbulent rough open channel flow; the main goal is to improve the understanding of the physical process that makes the particles move. In order to, it is necessary to monitor the flow's motion, with its near bed velocities and pressures to get the instantaneous values that cause the cohesion-less particle entrainment

We can also analyze the particle entrainment with a probabilistic approach to deal with the flow fluctuations uncertainty and to try to evaluate the entrainment rate of bed materials linked to the turbulent flow motion and the generated coherent structures.

This thesis project is related to a part of the whole research project and it's divided into two main sections: one deal with particles entrainment probability, the other looks at the tracking and the motion of the particles after entrainment

2. Problems of sediment entrainment

The flow in rivers and channels is the main cause of the particle motion and the entrainment; thus, studying flow that develops sediment transport is one of the most beneficial researches to be carried out in order to understand the mechanism that starts the motion of the particles. The flow conditions in rivers and streams have almost the same behaviour of turbulent flow in a rough bed condition, and most of the time they flow on a mild slope bed creating a sub-critical state.

The main problem about the particle entrainment is caused by the turbulence in flow, it can create unpredictable flow motions, various flow circulations and flow structures, which can induce forces of a wide range of magnitudes on walls and against sediments.

2.1. Flow equations for an open channel

Herein is adopted a right-hand coordinate system (x, y, z) which places x-axis in stream-wise direction, y-axis in span-wise and z-axis in the upwards perpendicular to the bed. Considering the velocity components (u, v, w) in their respective directions, we can start describing the flow behaviour from its basic equations, mass conservation equation (continuity equation):

$$div\,(\bar{u}) = \frac{\partial u_i}{\partial x_i} = 0$$

and Navier-Stokes momentum conservation equations:

$$\rho \left(\frac{\partial u_i}{\partial t} + u_j \frac{\partial u_i}{\partial x_j} \right) = -\frac{\partial p}{\partial x_i} + \gamma + \mu \frac{\partial^2 u_i}{\partial x_i \partial x_j}$$

where:

$\rho =$ fluid density

$\gamma =$ fluid specific weight

$t =$ time

$\bar{u} =$ velocity vector [u, v, w]

$p =$ pressure

$\mu =$ dynamic viscosity coefficient

$\nu =$ kinematic viscosity coefficient

$i, j =$ [x, y, z] components

These equations are connected to the instantaneous flow, using Reynolds decomposition it's possible to point out the terms controlled by the turbulence and the ones controlled by the average values of the flow. Reynolds decomposition is the result of analysis on the equations terms and their variations in time. They can be expressed as the sum of a mean value and a fluctuating one.

$$\begin{cases} u_i = \bar{u}_i + u'_i \\ p = \bar{p} + p' \end{cases}$$

The equation can be simplified to this form:

$$\frac{\partial \bar{u}_i}{\partial t} + \bar{u}_j \frac{\partial \bar{u}_i}{\partial x_j} = -\frac{1}{\rho} \frac{\partial \bar{p}}{\partial x_i} + g_i + \frac{\partial}{\partial x_j} \left(\nu \frac{\partial \bar{u}_i}{\partial x_j} \right) - \frac{\partial \overline{u'_i u'_j}}{\partial x_j}$$

it can be developed a spatial average over a volume big enough to eliminate the local variation caused by the topography, as previously made with the temporal average. The terms can be expressed with a mean value over space, a fluctuating value over space and the same one over time.

$$u_i = \bar{u}_i + u'_i = \langle\bar{u}_i\rangle + \tilde{u}_i + u'_i$$

The mass conservation equations and the Navier-Stokes conservation equations, for a flow over a fixed or slowly changing bed, after the double average (in time and space), can be written as follows (Nikora et al., 2007):

$$\frac{\partial \phi}{\partial t} + \frac{\partial \phi \langle\bar{u}_\iota\rangle}{\partial x_i} = 0$$

and

$$\frac{\partial \langle\bar{u}_i\rangle}{\partial t} + \langle\bar{u}_j\rangle \frac{\partial \langle\bar{u}_i\rangle}{\partial x_j} = -\frac{1}{\rho\phi}\frac{\partial \phi\langle\bar{p}\rangle}{\partial x_i} + g_i - \frac{1}{\phi}\frac{\partial \phi\langle\tilde{u}_i\tilde{u}_j\rangle}{\partial x_j} - \frac{1}{\phi}\frac{\partial \phi\overline{\langle u'_\iota u'_\jmath\rangle}}{\partial x_j} +$$

$$+\frac{1}{\phi}\frac{\partial}{\partial x_j}\phi\left(\langle v\frac{\partial \bar{u}_i}{\partial x_j}\rangle\right) + \frac{1}{\rho V_f}\overline{\int\int_{S_{\iota nt}} pn_\iota dS} - \frac{1}{V_f}\overline{\int\int_{S_{\iota nt}} v\frac{\partial u_\iota}{\partial x_\jmath}n_\jmath dS}$$

where:

$\phi = \dfrac{V_f}{V_0}$ = roughness function

V_f = fluid volume in the spatial averaged volume

V_0 = spatial averaged volume

S_{int} = roughness-fluid surface interface

$n_i = i^{th}$ normal component to the surface element dS directed into the fluid

$$\langle f_{pi}\rangle = \frac{1}{V_f}\overline{\int\int_{S_{\iota nt}} pn_\iota dS}$$

$$\langle f_{vi}\rangle = \frac{1}{V_f}\overline{\int\int_{S_{\iota nt}} \mu\frac{\partial u_\iota}{\partial x_\jmath}n_\jmath dS}$$

These represent the spatially averaged pressure and viscous skin friction interfacial forces per unit fluid volume.

2.2. Turbulent flow

The turbulence flow was studied in relation to the wall roughness. This can influence the formation of viscous sub-layer in the near bed flow. Reynolds roughness number, $R_e^* = \frac{k_s u^*}{v}$, is used to classify the flow boundaries, where u^* is the shear velocity and k_s roughness height, based on Prandtl theories and Nikuradse experiences. The flow can be affected by the roughness in three ways: roughness elements are not protruding over the viscous sub-layer and their effects are negligible, $R_e^* < 5$ (hydraulically smooth bed); roughness elements protrude beyond the viscous sub-layer, $5 < R_e^* < 70$ (incompletely rough beds); when roughness elements disturb the logarithmic layer and viscous effect are negligible, $R_e^* > 70$ (hydraulically rough bed).

2.2.1. Rough bed velocity distribution

The spatial flow average can be used to describe velocity profiles for atmospheric flows above a wavy bed (Wilson and Shaw, 1977) and for open channel flows (Gimenez-Curto et al., 1996). Considering this the rough bed open channel flow can be divided into five distinct layers (Nikora et al., 2001; Nikora, 2008).
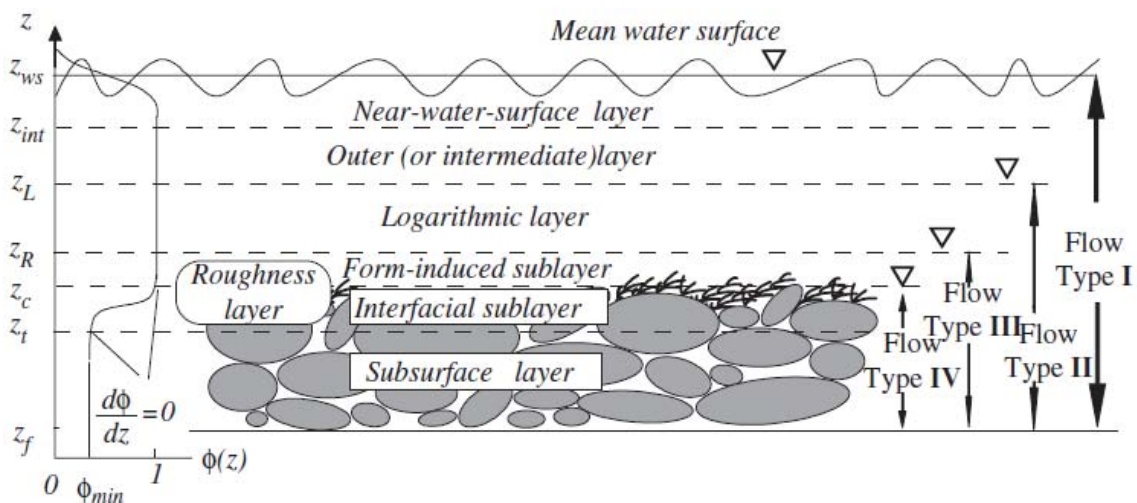
Figure 2-1 Subdivision of flow into layers and flow types.

Above the bed rough layer it can be found four more layer:
- Type I, flow of high relative submergence,
- Type II, flow of intermediate relative submergence,
- Type III, flow of low relative submergence,
- Type IV, flow in which roughness element are partially submerged.

In the logarithmic layer the velocity profile can be described by the log-law:

$$\frac{\langle \bar{u} \rangle}{u^*} = \frac{1}{k} \ln \frac{z}{k_s} + b$$

where:

$k = 0.4$, Von Karman parameter

b = constant from boundary conditions

$u^* = \sqrt{\frac{\tau_0}{\rho}}$ = shear velocity

τ_0 = shear bed stress

The log-law is valid above the viscous layer and up to the top of the logarithmic layer $(z/H < 0.2)$, above which a wake function ω (Coles, 1956) has to be superimposed to correct the velocity profile in the outer layer:

$$\omega = \frac{2\Pi}{k} cos^2 \left(\frac{\pi}{2} \frac{z}{H} \right)$$

where:

Π = Coles' wake strength parameter

H = water depth

The interfacial sublayer velocity profile in the double averaged equations can take several different forms, due to the influence of roughness elements near the roughness layer, it's typically considered linear.

The bed location is placed beneath the roughness within a distance δ, identified defined by the ratio of the following values (Nezu and Nakagawa, 1993):

$$0.15 < {}^{\delta}\!/_{z} < 30$$

2.2.2. Coherent structures

Despite the random nature of turbulent flow, recurrent and organized flow patterns occur in both smooth and rough bed flow condition. These self-sustaining flow patterns are called coherent structures if they are present for a relatively long time compared to the viscous scale time, so they are not a transient phenomenon. The solid transport in low rates is caused by extreme values of the fluctuating forces. These forces can be linked to the flow structures and a bed protection model can be developed based on the characteristics of those patterns (e.g. size, intensity, occurrence frequency, etc.). Coherent structures are supposed to be responsible for production and dissipation of turbulence in flow, so they are very influential on bed erosion.

These structures can be classified by the analysis of the Reynolds stress term, whose decomposition in four quadrants depends on the velocity components fluctuations (Willmarth and Lu, 1972). Considering the stream-wise velocity u' and the vertical velocity w', these are the four classes:

- Q1 - Outward interaction, $u' > 0$ and $w' > 0$
- Q2 - Ejection, $u' > 0$ and $w' > 0$
- Q3 - Inward interaction, $u' > 0$ and $w' < 0$
- Q4 - Sweep, $u' < 0$ and $w' < 0$

Statistical analysis over the velocity components shows a typically negative correlation between, u' and w', pointing out that the Reynolds stress term is particularly influenced by Sweep event near to the wall and Ejection events relatively far from the wall, above 12 wall units $z^* = zu^*/\upsilon$.

Looking at the smooth bed flows with the hydrogen bubble method (Kline et al., 1967; Kim et al., 1971) it can be noticed that in the turbulent boundary layer region $5 < z^* < 70$ there is a strong activity, with near-wall low-speed streaks with a span-wise dimension of 100 wall units. They start gradually, lift from the

bed, and after certain oscillation they create an ejection event into the outer boundary layer, and due to the mass conservation a sweep event may occur immediately after pushing high-velocity fluid towards the wall. This series of events is called "bursting cycle". Low speed streaks were visualized in near-wall rough bed flows with a span-wise distance of four roughness sand height (Defina, 1996).

The model of the horse-shoe vortex (Theodorsen, 1952) describes this bursting phenomenon, originating from undulations of the laminar sublayer, which create two counter-rotating stream-wise vortices and a low speed flow in between. The top of this structure is stream-wise inclined causing the low-speed flow ejection. This model was confirmed by some multidimensional flow visualization experiments in a smooth bed flow (Adrian, 2007).
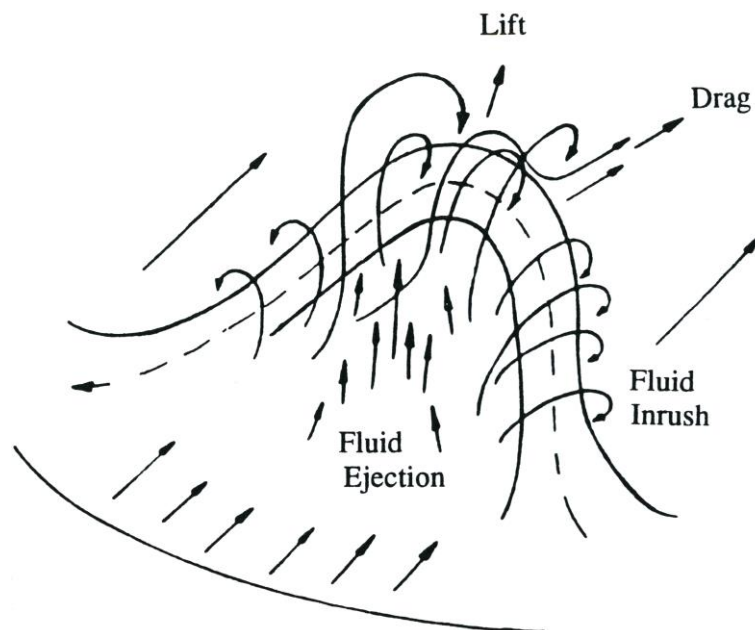
Figure 2-2 Theodorsen's model of horse-shoe vortex

This structures aspect depends on Reynolds number that makes them more stretched the higher the value of the Reynolds number. This is called a hairpin vortex. It was observed also that hairpin vortex frequently occurs in groups with the tops aligned and propagating with close stream-wise velocities, creating the so called hairpin vortex packages (HVP) (Adrian et al., 2000).

9

For a rough bed flow the mechanism responsible for the coherent structures is slightly different. The roughness height can induce small vortices that can cause turbulent structure formation (Arcalar and Smith, 1987).

2.2.3. Turbulence wall pressure

In a fully developed flow the magnitude of the fluctuations is greater than the mean quantities, and the viscous forces are smaller compared to the pressure forces (Hill and Thoroddsen, 1997) so according to Navier-Stokes equations the maximum forces are associated to pressure fluctuations, the other terms are negligible .

Considering the mean flow in x direction, $\bar{v}, \bar{w} \ll \bar{u}$:

$$\rho \frac{\partial u'}{\partial t} + \rho \bar{u} \frac{\partial u'}{\partial x} = -\rho \frac{\partial p'}{\partial x}$$

The pressure increment is comparable to the velocity fluctuations and the product with the mean velocity.

The pressure fluctuations generated by turbulent eddy can contribute to the forces on the particle to start the particle entrainment, the pressures caused by eddies are called turbulence wall pressure (TWP). These pressures were studied in some experiments developed in a wind tunnel (Schewe, 1983; Emmerling, 1973) and they are characterized by maximum peaks six times greater than the standard deviation, $p_{max} = 6\sigma_p$, so they must be considered in the particle entrainment issue.

Some experiments proved the relevance of TWP on particle entrainment especially for shielded particles more affected by eddies' influence (Hofland, 2005).

2.3. Forces on particles

The main forces generated from the flow that can make a stone move from its original position on the bed river are of two types: lift forces and drag forces defined as the vertical and stream-wise components of the hydrodynamics forces.

2.3.1. Drag forces

The drag force is determined by Reynolds number $R_e = \frac{du}{v}$ in relation to the particle dimension d and the flow velocity u. The flow motion is dominated by viscous stresses (skin drag) for $R_e \lesssim 1$, the laminar flow separates from the particle until becoming unstable for higher Reynolds number $R_e \lesssim 10^2$ and for a turbulent flow $R_e \gtrsim 10^3$ the skin drag becomes negligible and the instantaneous drag force is given by:

$$F_D = \overline{F_D} + F_D{}'(t) = \frac{1}{2}C_D\rho Au^2$$

If the flow is accelerating the particle is keeping the fluid around from that, and an additional mass term has to be added to consider this:

$$F_D = \frac{1}{2}C_D\rho Au^2 + \rho(1 + C_M)Va$$

where:

C_D = drag coefficient, $C_D(particle\ shape,\ R_e)$

A = exposed particle area perpendicular projection to the flow velocity

C_M = mass coefficient, $C_D(flow\ pattern)$

V = particle volume

a = fluid acceleration

Applying Reynolds decomposition to the drag force:

$$F_D = (\overline{F_D} + F_D{}') \propto (\bar{u}^2 + u'^2 + 2\bar{u}u')$$

$$\overline{F_D} \propto \left(\bar{u}^2 + \overline{u'^2}\right)$$

$$F_D{}' \propto 2\bar{u}u' + \left(u'^2 - \overline{u'^2}\right)$$

Looking at the fluctuating drag force terms $\overline{u'^2} = \sigma_u^2$ is the variance of u and if the flow is rather uniform it is reasonable assuming $\bar{u} \gg |u'|$, so the second term can be neglected, but this is not possible in a near-bed flow because various experiments showed the same order of magnitude between $\bar{u}$ and $|u'|$, showing $\sigma_{F_D}/\overline{F_D} \propto (0.4 \div 0.8)$ (Chepil, 1959; Xingkui and Fontijin, 1993). Remember that the drag coefficient C_D can be calculated only by knowing the exposed area and the flow velocity, which presents a near bed strong gradient, the magnitude of the drag force depends also on those factors, and different methods suggest different reference parameters.

2.3.2. Lift forces

The mechanism behind the lift forces is not well understood, but they are generated by the high velocity gradient between the top and the bottom of a particle, and this induces a pressure difference in the two surfaces. In fact for a non-viscous flow the velocity increase is linked to a pressure decrease. The lift force can be described for a flatbed in a similar way to the drag one:

$$F_L = \frac{1}{2}C_L\rho A u^2$$

And for the fluctuating part the following expression was proposed (Radecke and Schulz-DuBois,1988):

$$F_L{}' \propto \mathrm{a}\bar{u}u' + \mathrm{b}\bar{u}w'$$

where:

C_L = lift coefficient, $C_L(particle\ shape,\ R_e)$

a, b = constants

In the previous equation the first term is responsible for the main variance and represents the Bernoulli effect, while the second is similar to a vertical drag due to the eddy shedding. The fluctuating lift force effects were studied in experiments for near bed particle (Einstein & El-Samni, 1949; Xingkui & Fontijn, 1993, natural stone) and they showed the same order of magnitude between fluctuations and mean force, $\sigma_{F_L}/\overline{F_L} \propto (0.36 \div 1.0)$. The same uncertainty about the comparison between different methods relative to the drag forces is present in computation of the lift forces, in relation to the lift coefficient C_L and the reference velocities.

2.3.3.   Force duration

After the magnitude, force duration must also be considered. This aspect was suggested by some experiment results comparing the maximum stream-wise velocities fluctuations to the particle event of entrainment (Diplas et al., 2008). The erosion events required velocity peaks but the opposite wasn't true.

The combination of the two aspects of the fluctuating force can be resumed by the impulse I_i over the force duration T_i:

$$I_i = \int_{t_i}^{t_i+T_i} F'_i(t)dt$$

According to Newton's second law:

$$F = m\frac{du_p}{dt} \longrightarrow Fdt = mdu_p$$

The equation above shows the impulse relevance in the particle motion. It is equal to the product of particle mass and velocity variation.

The impulse importance was also considered in a recent study, (Dwivedi et al., 2011), it was confirmed that it's an important factor to start the sediment erosion, an optimum combination of magnitude and duration is required to produce the critical impulse.

2.4. Particle parameters

The particles that create the bed layer of a river can be of various types and can be organized in different ways. According to the sediment transport problem, the flow drag and lift forces are mainly influenced by particle features. The stones can be described by the following main parameters: shape, size, position amd orientation.

2.4.1. Shape

The particle shape can influence the flow near-bed velocity and fluctuations, but in particular it's important for the magnitude of drag and lift forces, e.g. a flat stone is more likely to be entrained by a lift force rather than a drag force. Shape can be described referring to the principal dimension of a box a, b, c respectively in increasing length order. For indicating the sediment flatness it can be used the shape factor $SF = a/\sqrt{bc}$. Sharpness of the edges can be better described visually.

2.4.2.   Size

Usually a diameter is taken to represent the size of the particle; the two main options are considering the sieve diameter dimension or deducing it from the particle volume value.

- Sieve diameter d_s: it is the dimension of the smallest sieve mesh through which the particle is able to pass. It is typically used to classify the granulometry of the ground, indicating the diameter corresponding to the percentage of ground passer-by, e.g. d_{50} it's the 50% of passer-by's diameter.

- Nominal diameter d_n: it is the edge length of and equivalent cube with the same volume of the particle, $d_n = \sqrt[3]{m/\rho_s}$.

2.4.3.   Position

The particle location in relation to the other sediment can be summarized by exposure e, protrusion Π, and pivoting angle φ.

- protrusion Π: the top particle height from the mean bed level,
- exposure e: the top particle height form the local mean upstream bed layer,
- pivoting angle φ: the maximum angle the bed can be tilted without moving the particle.

The drag and lift forces are influenced by the particle position. It depends on the ratio Π/d or e/d, if the unity value is assumed, $\Pi/d = 1$, the sediment is completely exposed and large drag forces will occur on it. The opposite, if it present a null value, $\Pi/d = 0$, the stone is completely shielded and it can be raised only by a big lift force. The pivoting angle can indicate the magnitude of the resisting forces moment about the point of rotation.
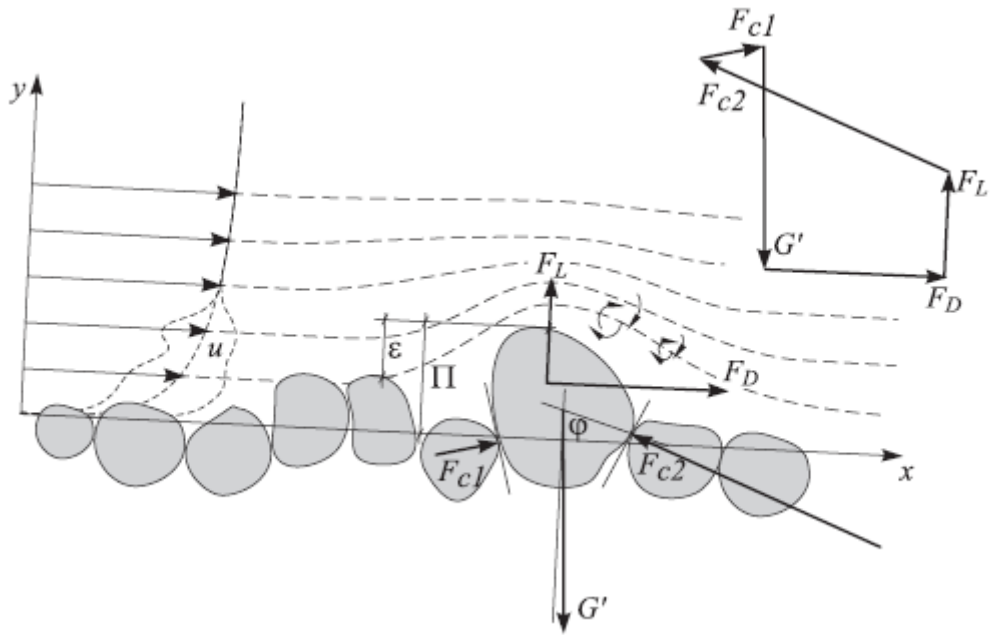
This Figure 2-3 The picture shows the stone position and the forces that act over it.

The effect of the relative protrusion over the entrainment was studied in relation to the dimensionless shear critical stress θ_c (Shields, 1936) and those experiments showed that for a positive value of protrusion $0 \div 0.8$ the dimensionless Shields parameter vary between $0.15 \div 0.1$ (Fenton and Abbot, 1977).
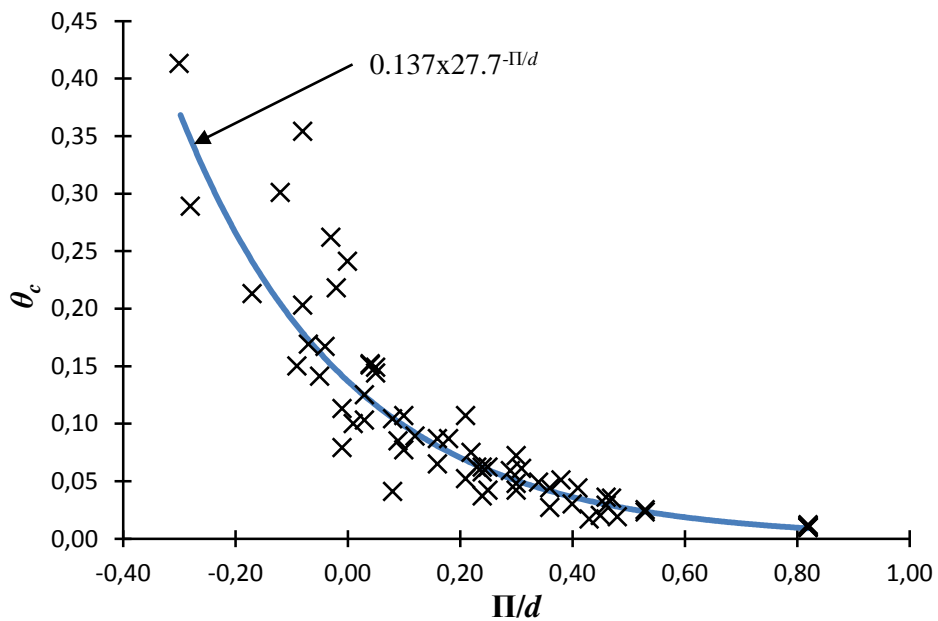
Figure 2-4 Fenton and Abbot experiments results, dimensionless Shields parameter against relative protrusion.

2.4.4. Orientation

Generally, we can describe the orientation referring to the two angles, the one between the longest particle dimension axis and the flow main direction, and the other with the shortest particle axis.

Studying the particles orientation on a stable bed it has been observed that they tend to assume two positions with the long axis perpendicular (Nikora et al., 1998) and parallel (De Boer, 1998) to the flow direction. And after entrainment the particle tend to roll with the longest axis span-wise to the flow (Carling et al., 1992).

2.4.5. Relative influence

The following table compares the relative importance between the above described parameters with their influence over the shear stress value at which the particle becomes unstable, using a range for parameters within a bed protection values (Hofland, 2005).

Characteristic	Approximate influence factor	Source(s)
Position ($\Pi/d=0$–0.5)	5	(Fenton & Abbot, 1977)
Orientation	>10	(Carling et al., 1992)
Size ($d_{85}/d_{15} = 1.5$)	2	(Shields, 1936)
Shape (when d_n is used)	0.2	(Breusers, 1965; Carling et al., 1992)

Table 2-1 Approximate parameters influence on particle stability, (Hofland, 2005).

2.5.   Particle entrainment prediction

The main purpose of studying the particle entrainment is to develop a method to predict the flow conditions that make a sediment move. As previously stated, there is a lot of factors contributing to this mechanism. The hydrodynamic forces of drag and lift, and their duration due to the flow fluctuations determined by the turbulence as the coherent structures and turbulence wall pressures must be considered. On the other hand it must not be forgotten to regard the stone parameters, which characterize the likelihood entrainment.

2.5.1.   Critical shear stress

One of the older and most used approaches is the one developed by Shields (1936), who introduced the concept of critical shear stress θ_c to indicate the beginning of the sediment particle motion. Shields considered the forces acting on the particle with a ratio between destabilizing and stabilizing forces, as the load on the particle and the gravitational force, developing the Shields parameter θ, a dimensionless shear stress:

$$\theta = \frac{\tau_0}{(\rho_s - \rho)gd} = \frac{u^{*2}}{\Delta gd}$$

$$\theta_c = \theta_c(R_e^*) = \theta_c\left(\frac{u^*d}{v}\right)$$

According to Shields cohesion-less particle motion starts above the threshold condition, so $\theta > \theta_c$. Shields' critical threshold value is $\theta_c = 0.06$ for rough turbulent flow. However, this value was based on limited experiments and it contains high levels of uncertainty, further experiments report the value of $\theta_c = 0.045$ (Miller et al., 1977; Buffington and Montgomery, 1997).
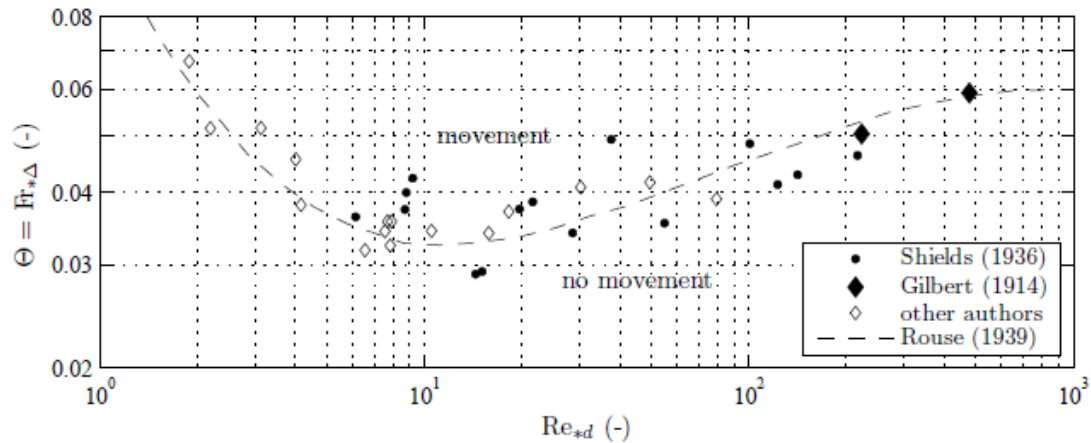
Figure 2-5 Shields' results representation, redraft.

Others experiments proved that sediment moves also for conditions below the shear critical stress (Grass, 1970; Lavelle and Mojfeld, 1987).

The critical shear stress parameter involves the computation of a temporal and special averaging over the fluctuations of the near-bed shear stress, and it does not account for the bed variability, but it becomes popular due to its simplicity.

2.5.2.   Stochastic approach

Thinking about the hydrodynamic load on a particle and the resisting forces on the particle are both stochastic processes, they change respectively in space and time and with the particle features. According to a stochastic approach to the sediment entrainment proposed by Grass (1970), the beginning of sediment movement can be considered a stochastic process that occurs due to the overlapping of the probability distribution tails between the turbulent flow load, τ_b and the resistance of a random bed geometry, τ_c. The overlapping in the following graph can be explained also as the greatest fluctuating flow loads are able to move the less resistant particles.

19
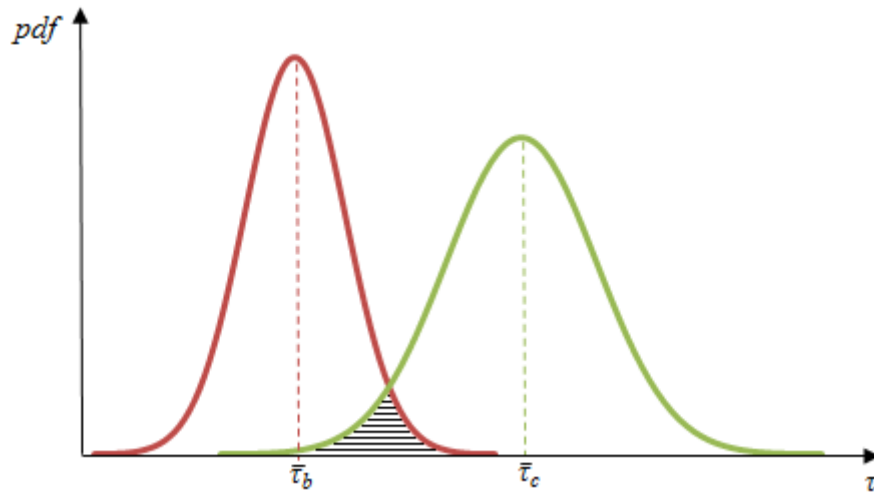
Figure 2-6 Pdf graph of flow load τ_b and particle resistance τ_c.

The dashed area in the graph represents the probability of entrainment and can be expressed by the following equation:

$$P(\tau_b > \tau_c) = \int\limits_{0}^{\infty} P(\tau_c) \int\limits_{\tau_c}^{\infty} P(\tau_b)\, d\tau_b\, d\tau_c$$

Experiments with a probabilistic approach were made by Zanke (2003) showing that they coincide with shields curve $(R_e^* \approx 10 \div 200)$ for an entrainment probability risk of 10%, the ones developed by McEwan et al. (2004), for uniformly sized beds, show that for $\theta_c = 0.06$, the $1 \div 2$ % of the bed's weight surface is mobile.

In relation to some test on moving particles and the linked near bed velocity developed by Bottacin-Busolin et al. (2008). It has been suggested to use this velocity rather than the shear stress as the significant parameter in Grass's stochastic approach, due to its greater influence in grain entrainment.

2.6. Role of coherent structures

Coherent structures are the main cause of the big fluctuations in the flow due to turbulences; this means that the instantaneous hydrodynamic forces over the particle are influenced by those structures. Research has focused on the event of Ejection (Q2) and Sweep (Q4) for the negative correlation between u' and w' that is responsible for the biggest positive values on the Reynolds shear stress $(\propto -u'w')$.

Interactions between sediment motion and bursting events were measured with a synchronized Laser Doppler Velocimetry (LDV) by Nelson et al. (1995) discovering that sweep events cause most of the entrainments and some outward interactions too. In contrast, inward interactions and ejections are less important. This means that the Reynolds shear stress is not strongly correlated to the entrainment.

The use of PIV 2D technique allowed Hofland and Booij (2004) to measure the flow during the entrainment of a single stone, and they found two main structures responsible for the entrainments. The first one, a small-scale vertical vortex, lifted the particle and the second one, a large-scale sweep, moved the stone stream-wise over the pivoting point. Analysing local stream-wise velocities near the particle's top, it can be noticed that sweep events dominate the particle entrainments (Cameron, 2006).

Some studies over the near bed stream-wise velocity were carried out and they showed a strong positive correlation between that and the sediment movement, on the contrary both Reynolds stress and vertical velocity component are widely variable at the point of entrainment (Schmeeckle and Nelson, 2003; Cameron, 2006). So the sediment entrainment threshold related to the forces is more likely caused by the maximum values instead of the mean values.

2.7.   Particle motion

The sediment particles transported in a water flow can be of a bed-load or suspended-load type depending on the flow condition and the particle. Comparisons between smooth-bed and rough-bed flow showed that particle motion in those cases is similar keeping the same Reynolds number value and entrained particle (Sumer and Deigaard, 1980). Furthermore, sediment transport in rough-bed conditions typically occurs in nature. This is the reason for more interest about this phenomenon.

The suspended-load transport occurs when the particle is fully supported by a succession of upward impulses by turbulent eddies, otherwise the bed-load transport is a succession of contacts with the bed's particles and gravity plays the main role in controlling these motions (Bagnold, 1973).

 Usually, particle motion is classified into three categories:

- Rolling and sliding
- Saltation motion
- Suspended particle motion

These processes are regulated by the bed shear velocity. If this velocity exceeds the critical value, the particle will start to roll and slide over the bed. For higher values of it, the stone will start to bounce above the bed creating more or less regular jumps. When the shear bed velocity exceeds the particle fall velocity, the sediment can be lifted upwards, the turbulent force magnitude is of the same order or bigger than the submerged weight the particle may go in suspension.

The saltation motion is governed by gravity forces while the effect of the turbulence has a minor role on the overall trajectory. This means that the particle paths would describe a wavy line within a maximum height, due to the turbulent flow conditions. It is reasonable to consider the height and length of a jump trajectory as random variables in dependence of the flow conditions and the particle features.

3. Project goals

The main purpose of this research project is to study the behavior of the turbulent open channel flow in relation to the particle entrainment on the bottom layer, looking at the influence of few different parameters.

The work of this thesis is part of a research project focusing on the motion of the entrained particle without considering the flow data records to study the behavior of the particle in the first stages of the solid transport.

This can be done through laboratory experiments in a flume, creating the conditions for the particle motion, recording the sediment movements in the turbulent flow and all the other useful data. By reproducing the experiments over different settings it is possible to investigate the influence of the different parameters with the following objectives:

- To study the probability of occurrence of a particle's motion in relation to the particle's density, protrusion and the flow rate.
- To study the main behavior of a particle's motion, looking at its displacement, velocities and accelerations into the turbulent flow.
- To examine the beginning of a particle motion analyzing the starting forces of the sediment transport.

4. Methodology

The aims of the experiments carried out in laboratory had the main purpose of reproducing a simple case of sediment transport in a turbulent open channel flow, and to monitor this event with data recording. These laboratory tests were developed to reduce the complexity of the phenomenon and to focus only on the main aspects of the topic. These experiments have been realized with a rectangular section open channel, the particles used in it were spheres of the same dimension, and only one of them was left free to be entrained by the flow using a light one. All the others were made of glass, too heavy for being moved by the used flows, with them was realised the bottom layer roughness.

This way the complexity of the sediment transport caused by the usual big amount of parameters is lowered in those tests. Moreover, the channel can be set with all the instruments pointed at the target particle and the flow around it.

The flow motion can be checked by using the PIV method (Particle Image Velocimetry) to find out flow and particles displacements, velocities and accelerations. It can also be useful to have some pressure sensors placed in the bottom layer, to register the instantaneous variations in the flow.

In this thesis the PIV data collection is used for tracking the target sediment motion from the time just before the stone's entrainment, until its exit from the control area.

4.1.   Principles of Particle Image Velocimetry, PIV

The PIV method is a velocity measurement technique with the ability to record the high frequency velocity components of a large section of a flow field simultaneously. It consists of record images of the flow motion with a group of cameras, this can be done with a laser light precisely directed to the target flow field zone, in this section the laser beam lights up the tracer particles in the water and shows them clearly. Thus, the flow motion can be recorded by the

cameras. All PIV systems contain a number of essential components (Prasad 2000a) (Figure 4.1-1).
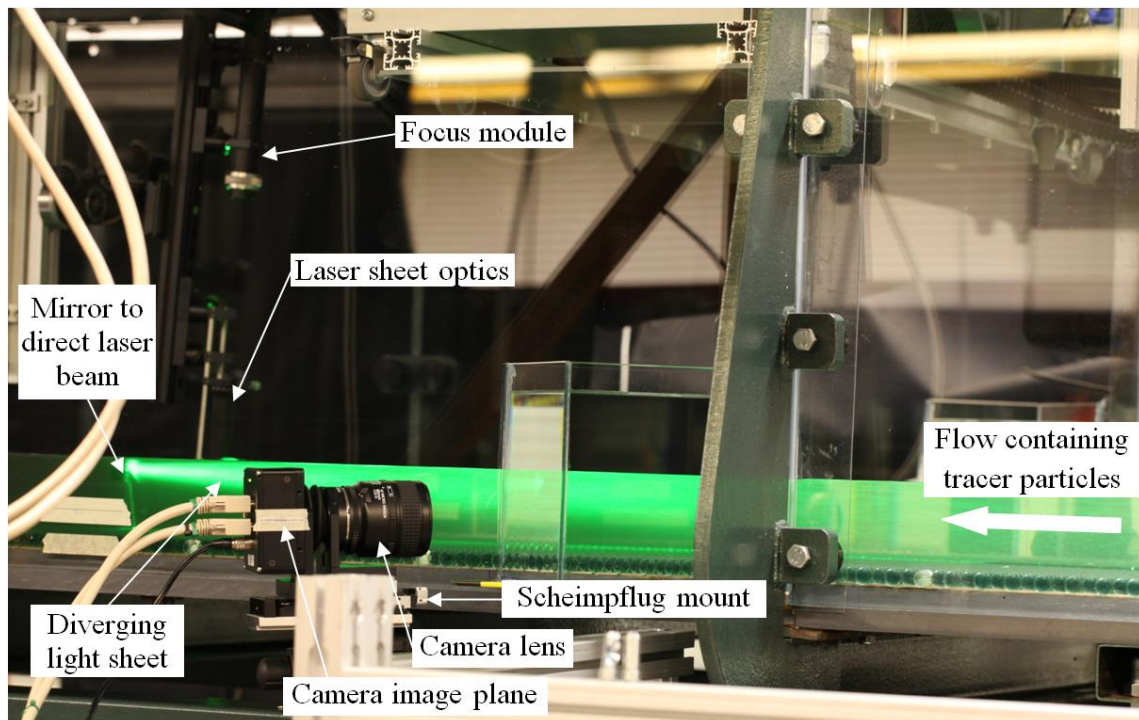
Figure 4-1 Experimental arrangement of PIV.

Firstly, an optically transparent test section of the flow, usually containing tracer particles which have been added specifically for PIV, is illuminated, typically by a laser, at least twice within a short time interval. The tracer particles in the illuminated section scatter the incident light; the pattern of the scattered light is recorded at both pulses using high resolution digital cameras and the recorded images are divided into a large number of small windows called interrogation areas. The content of each interrogation area is analysed to determine the displacement of the tracer particles between the illuminations which, together with the time between illuminations, is used to calculate the velocity of the tracer particles, and indirectly the velocity of the flow (Raffel et al. 1998). The procedure is repeated for all interrogation areas, combining the results to generate a velocity map for the entire flow field.

4.1.1.   Panoramic PIV

The classical method of PIV involves the imaging of light scattered by tracer particles in a two dimensional plane, and analysis of the results to calculate the two in-plane components of velocity (2C2D).

Cross-correlation is performed on PIV recordings to determine the mean particle displacements. The cross-correlation function, $C(S)$, is defined by:

$$C(S) = \int_{area} I_1(X)I_2(X+S)dx$$

where I_1 and I_2 are the intensity patterns for the first and second exposures respectively. Direct computation of the auto-correlation function from this formula is laborious; computational demands can be significantly reduced by performing calculations using a two dimensional Fast Fourier Transform (FFT) of the intensity pattern:

$$C(S) = F^{-1}\{F\{I_1(X)\}\} \cdot F^*\{I_{12}(X)\}$$

where * represents the convolution operation (Prasad 2000). The procedure for cross-correlation is outlined in (figure).
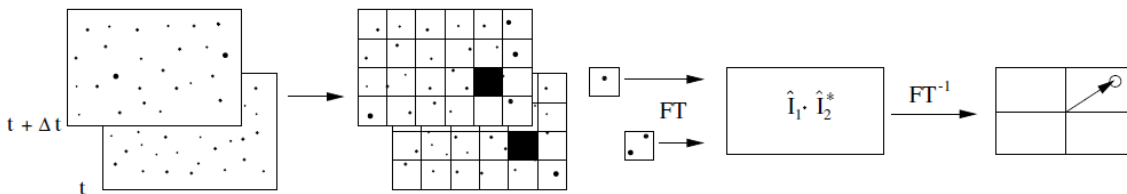
Figure 4-2 Analysis of PIV recording using cross-correlation function (Raffel et al. 2007).

The cross-correlation function produces a signal peak that is displaced from the origin by the average spatial displacement between the two illumination pulses of all particles within the interrogation area. Noise present within the recordings reduces the height of the signal peak, relative to the background, while velocity

gradients within the interrogation area broaden the signal peak (Willert and Gharib 1991).

Investigation has led to the development of several advanced interrogation algorithms including: multiple pass interrogation, coarse-to-fine interrogation, and window deformation interrogation. Multiple pass systems use the results of standard interrogation to offset the interrogation area in the second frame, before repeating the interrogation. This results in more pairs and a higher signal-to-noise ratio. Coarse-to-fine interrogation uses a multiple pass system with the addition of decreasing the interrogation area size between passes and leads to an increase in the dynamic spatial range. Window deformation allows the shape of the interrogation area on the second image to move and deform in order to maximise the number of image pairs, it exhibits increased robustness and accuracy in highly sheared flows.

4.1.2.   Stereoscopic PIV

Stereoscopic PIV was developed later than panoramic PIV. It allows all three components of velocity to be measured, whilst still considering a two dimensional plane (3C2D). Stereoscopic PIV uses at least two cameras to simultaneously record two views of the illumination pulse from different angles (Prasad 2000b).

Each camera view in stereoscopic analysis must be individually interrogated using cross-correlation analysis in order to create the velocity map on the Cartesian grid for each camera. In order for the particle velocities to be calculated, simultaneously recorded images from the two or more cameras have to be precisely matched (Grant 1997). Reconstruction is the process of obtaining three dimensional data by mapping the displacements from each image plane onto the object plane (Prasad 2000b); reconstruction can be performed based on 3D calibration, a method which requires no knowledge of geometry, and generates a mapping function. This mapping function is

28

calculated from images taken on all cameras of a calibration target placed in the flow slightly in front of, at and slightly behind the object plane. Perspective error found in classical PIV, due to a single camera (when recording particles off the camera's axis) incorrectly mapping an out-of-plane displacement as an in-plane displacement (Prasad 2000b; Grant 1997) is eradicated during the reconstruction process.

5. Instruments and facilities

The recently developed Aberdeen Open Channel Facility (AOCF) was designed and built at the University of Aberdeen. It consists of an open channel flume, along the top of which runs an instrumental carriage carrying an advanced particle image velocimetry (PIV) system.

5.1.   Open Channel Flume

The flume has working dimensions of 18 m in length and 1.18 m in width. It is a re-circulating flume with a flow powered by two pumps, and has a maximum total flow rate of 150 l/s. The flow rate is measured by an electromagnetic flow meter (consisting of Siemens SITRANS F M MAG 5100W and MAG 5000 transmitter) located in the inflow pipe prior to the flume entrance. Several automatic jacks allow the bed slope to be altered over a range of $-0.5°$ to $2.5°$. The flow rate and bed slope are both computer controlled allowing a high level of accuracy and the generation of repeatable flow conditions. The bed of the flume has been laid over its entire working area with artificial roughness elements, in the form of glass spheres, in a hexagonal close packing arrangement. To achieve this layout stainless steel plates with holes drilled in the required arrangement were attached to the bed. Lighter roughness elements, of two densities, were purchased to undertake entrainment experiments under a variety of flow conditions.

One further roughness element type coloured black was required for the area of the bed around the PIV measurement section, to avoid an extra-reflection of the laser light in the control zone and to reduce the noise in the data recording.

Special roughness elements have been manufactured at the University of Aberdeen, inside each of which is a small modified differential pressure sensor (Honeywell Piezo resistive sensor, 24PCE series). Two types of these special roughness elements have been made: drag sensors, in which the ports of the

pressure sensor align parallel to the bed; and lift sensors, in which the ports of the pressure sensor align perpendicular to the bed (figure). The wires connecting the pressure sensors to the data logger pass through the bed of the flume. In order to enable the required orientation of the parts, each lift sensor consists of three roughness elements, with the end one containing the pressure sensor.
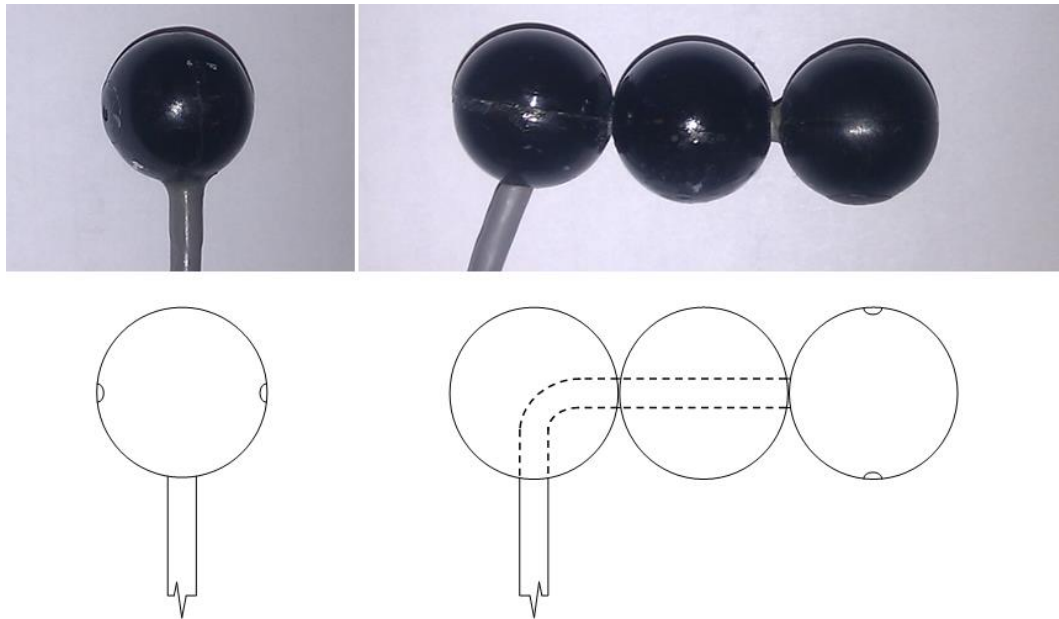
Figure 5-1 Photo and diagram of drag pressure sensor (left) and lift pressure sensor (right).

5.2.   Instrumental Carriage

An instrumental carriage approximately 1.8 m long and weighing up to 250 kg runs along the length of the flume on rails attached to the top of the side walls. The carriage is capable of housing the complete PIV system, ultrasonic range finders and an R&D Vision signal generator that emits a trigger synchronizing the start of water surface, pressure and PIV measurements. The carriage is motorized with a maximum speed of 1.1 m/s. It is controlled by a computer located on the carriage (that can be remotely connected to from any other networked computer) and can be moved to precise positions along the flume.

Three ultrasonic range finders (URFs), two Baumer UNAM 12U9914/S14 sensors and one Banner U-GAGE S18U sensor, are installed on the carriage to measure the water surface, and flume bed profiles. The Baumer sensors are referred to as URF1 and URF2, and the Banner sensor as URF3 hereon. URFs 1 and 2 have a range of 20-200 mm and URF3 a range of 30-300 mm. URF3 has built-in temperature compensation, whereas URFs 1 and 2 do not. Therefore, air temperature measurements must be made in order to allow for compensation of temperature changes. These measurements are made automatically throughout the day using a Testo 735 air temperature probe, which collects data at fixed intervals for a set duration as determined by the user.

5.3. Particle Image Velocimetry System

The PIV system is comprised of five key elements: 1) tracer particles, 2) laser system, 3) camera system, 4) synchronization system and 5) software.

5.3.1. Tracer Particles

The flow itself cannot be directly measured therefore neutrally buoyant hollow glass spheres of 10-20 μm in diameter are added to the water. These are designed to follow the flow and have a reflective coating applied.

5.3.2. Laser System

The laser system consists of the laser head, an articulated laser arm, and a focus module. The laser head comprises twin Nd:Yag frequency doubled lasers, emitting radiation at frequencies of 532 nm (visible green light utilised during PIV) and 1064 nm. The lasers operate independently of one another in pulsed modes with the pulse separation (between lasers) and the repetition rate set by

the user. The laser beam has a diameter of 4mm with a divergence of less than 2.0 mrad.

The laser head is situated on the carriage and the emitted beam is passed through a highly flexible articulated laser arm. This arm transmits the light safely to the focus module, the position of which varies greatly depending on the experimental set-up.

The focus module itself consists of a cylindrical lens that diverges the beam into a sheet and a pair of spherical lenses that can be adjusted to control the focal point of the light sheet thickness. The cylindrical lens is adjustable, allowing the rotation of the light sheet relative to the bed to be set. There are three options for the cylindrical lens (-25, -50 or -100 mm) depending on the divergence required.↑

5.3.3.   Camera System

Four cameras each consisting of a Dalsa Falcon 4M60 CMOS sensor, a Nikon lens and a Scheimpflug mount, combine to create the camera system. The Dalsa Falcon 4M60 has a resolution of 2352 x 1728 pixels (4 mega pixels), a pixel size of 7.4 µm and a maximum frame rate of 62 fps at full resolution.

The lens is a Nikon AF Micro-Nikkor 60mm f/2.8D with a fixed focal length of 60 mm. The Scheimpflug mount provides a stand for each lens and sensor combination, allowing for lens movement in the horizontal plane, along two perpendicular axes, and a rotation of ±15° between the sensor and the lens to enable non-orthogonal viewing.

5.3.4.   Synchronization System

The final key element of the PIV system is the accurate timing of the laser pulses and camera operation. This is provided by a sync generator (R&D Vision programmable, 6 channel signal generator).

5.3.5. Software

A software package entitled Slugflow has been developed by Dr S Cameron in-house at the university. This package is capable of performing image pre-processing, image analysis and post processing. Pre-processing includes calibration, to map the position of each camera relative to the light sheet, and corrections to account for any deviation of the light sheet from perpendicular, relative to the bed. The image analysis is an iterative process that takes pairs of images and uses them to compute an instantaneous vector field of the flow measurement area. This analysis is based on the use of fast Fourier transforms (FFT) and utilises multiple pass interrogation with window deformation. Finally, post processing calculates flow parameters (e.g. double averaged flow properties).

The software is also capable of creating a rough tracking of the particle. To check analyse images and to produce the results in simple files allowing an easy data elaboration with other software such as Matlab.

6. Experimental set-up

The entrainment experiments were carried out with different parameter settings. Those settings considered various flow rates, target particle protrusions and densities.

The open channel flume was prepared as previously described, by creating a roughness bottom layer with glass marbles and settling in the PIV target zone black marbles and pressure sensors. Thus, the position of the target particle was provided by a device for changing its protrusion and a fixed ring of black marbles around it to be sure of the boundaries stability.

6.1.   Bed Layer Layout

The bed layer was created using only one layout, the Hexagonal Close Packing structure, with only one layer of marbles (HCP-1). The heavy glass marbles were settled on stainless steel plates with holes specially drilled in them, creating the roughness fixed bed. In further tests it is possible to arrange bed layer with different packing structures checking the influence of it in the flow motion.

Material	Colour	Shape	Sample size	Density, ρ, g/cm³		Diameter, d, (mm)	
				m	σ	m	σ
Glass	Green	Sphere	200	2.52	0.021	15.98	0.101
Delrin	White	Sphere	50	1.37	0.005	15.99	0.006
Nylon	White	Sphere	50	1.11	0.003	15.96	0.005

Table 6-1 Properties of roughness elements.

In addition to the glass spheres other two types of lighter roughness elements (Delrin, "D" and Nylon, "N") were purchased to undertake entrainment experiments under a variety of flow conditions. Those last two types were used as the target particle in the tests. The properties of the roughness elements were measured from random samples and are outlined in the table.

6.2. Flow Conditions

A range of three different flow conditions were considered with the relative depths H of 12 - 3 cm, the Particle Reynolds Number (Re-t) referred to the flow depth in the range 1260 - 5045 and the value of Froude Number (Fr) always less than one, in the range 0.40 - 0.66, creating a subcritical flow. Further details are showed in the following table.

$$Re_b = \frac{H \cdot U}{v} \qquad Re_\tau = \frac{H \cdot u^*}{v} \qquad Fr = \frac{U}{\sqrt{gH}}$$

Run	D, m	H, m	H/D	Sb	Q, m3/s	Re_b	Re_τ	Fr	U, m/s	u^*, m/s
A	0,016	0,030	1,875	0,00600	0,01261	10683	1261	0,656	0,35608	0,04202
E	0,016	0,070	4,375	0,00257	0,03387	28699	2941	0,495	0,40999	0,04201
H	0,016	0,120	7,500	0,00150	0,06353	53839	5043	0,414	0,44866	0,04202

Table 6-2 Run Table

The mean velocity computations in the table are made using Manning Equation by assuming the value of Manning Number, n=0.021 (Strickler Number Ks= 47,62 m$^{1/3}$/s). These chosen flows rate covers the whole range available with a high degree of accuracy in the Open Channel Flume.

6.3. PIV Layout

Panoramic and stereoscopic PIV was used in different PIV modes. During all the tests the flow water depth, from bed roughness tops to water surface, was recorded. In lower water depths, due to the small control zone, the frame rate of the cameras can be increased and the frequency of PIV recordings were set at the maximum possible setting for each water depth (to balance the huge amount of information collected allowing a reasonable amount of time for data processing). During entrainment experiments the recordings were cut to a length of approximately 10 s before, and 30 s after the point of entrainment.

6.3.1. Panoramic PIV

Panoramic PIV mode was pointed directly over the target particle with the light sheet parallel to the flow direction.
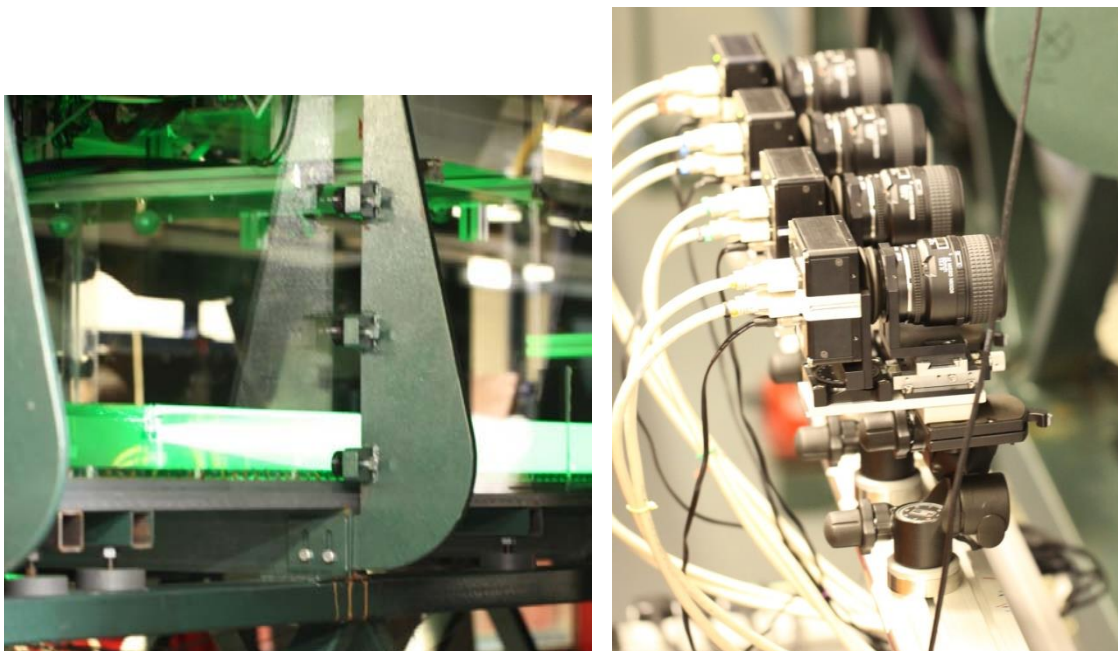

Figure 6-1 Photos of expanding laser light sheet (left) and camera set-up (right)

The measurement section (the area of the light sheet seen in the cameras) is approximately 800 mm in length and is centred on the target particle (figure).

The primary advantage of the panoramic set-up is the large measurement section recorded without the loss of spatial resolution.
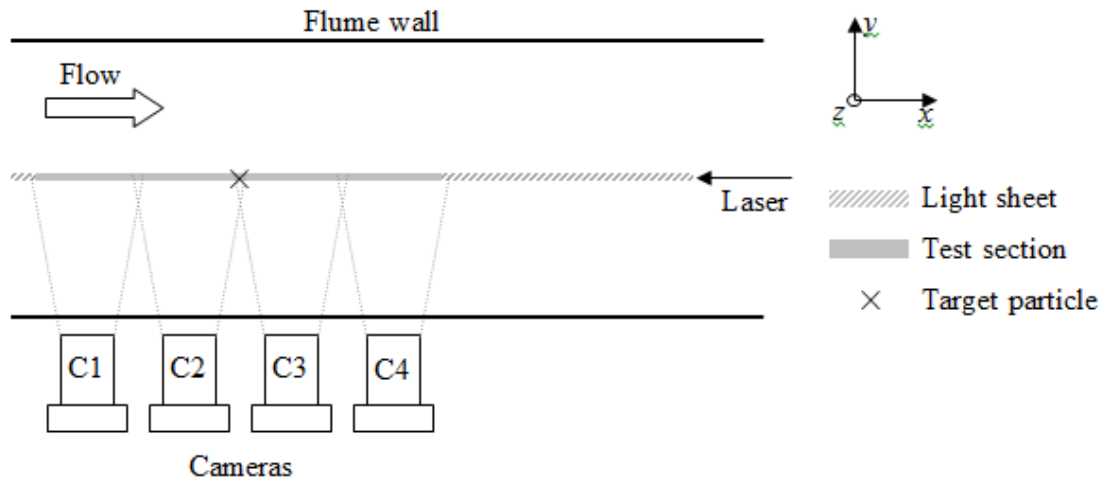
Figure 6-2 Plan view of panoramic PIV arrangement.

6.3.2. Stereoscopic PIV

To perform the stereoscopic PIV only two cameras are required, however the arrangement uses four cameras in order to reduce noise by building some data redundancy into the system. Prasad (2000b) highlighted that when recording at large off-axis angles through a thick liquid layer, image distortions can occur caused by the light refractions. Therefore, water filled prisms are attached to the outside of the flume wall in order to reduce this distortion (Prasad 2000b), and prevent the issues from arising from the internal reflection.

The light sheet can be pointer stream-wise in the flow opposite direction or span-wise, however, the measurement section is smaller, approximately 300 mm in length, since all four cameras are focused on the same point (figure).
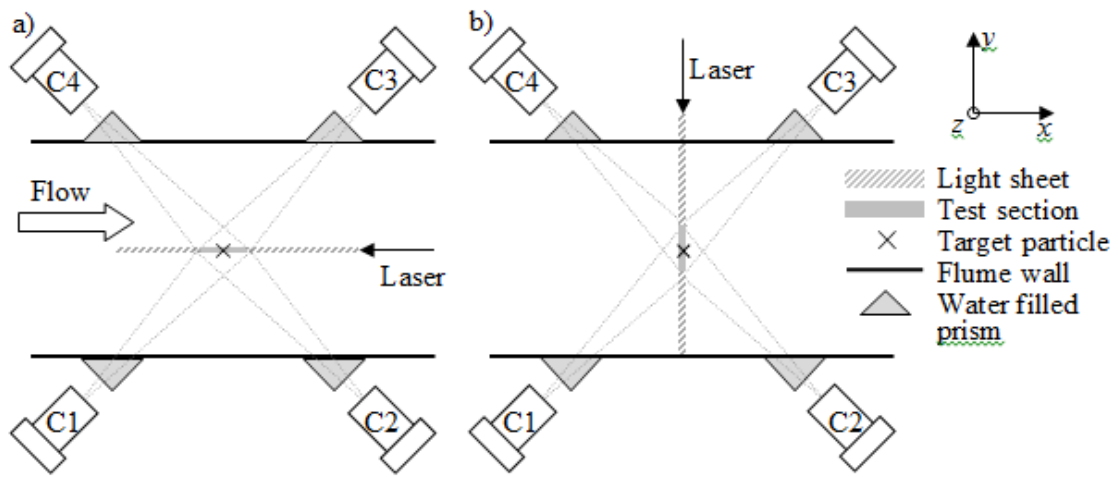
Figure 6-3 Plan view of a) mode and b) mode PIV arrangements.

The following photos demonstrate this arrangement in the laboratory:
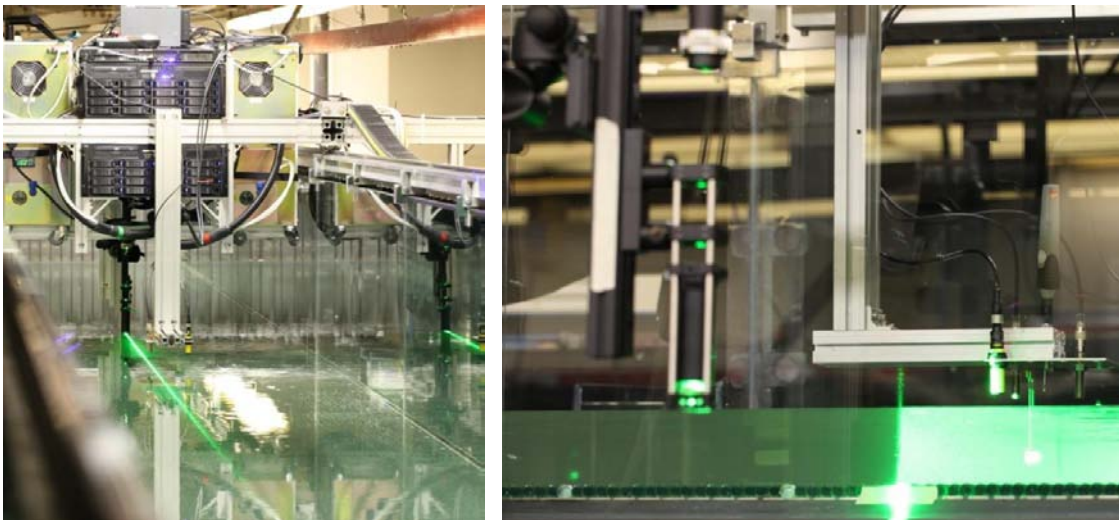
Figure 6-4 Laser and URF arrangement photos taken looking downstream for mode a) (left) and from the side of the flume for mode b) (right).
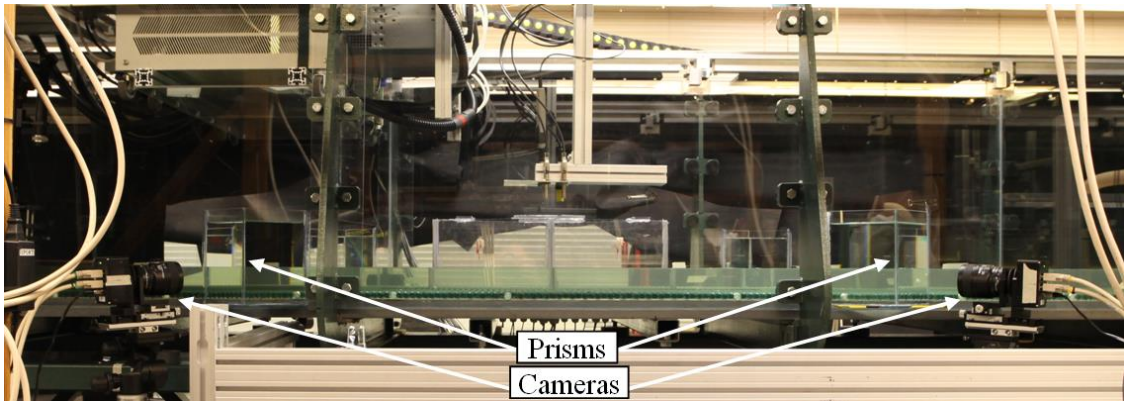
Figure 6-5 Camera positioning for stereoscopic PIV.

After testing some different arrangements, for the following experiments have been chosen to use the stereoscopic PIV configured in mode 6, i.e. a stream-wise laser beam a) with the records of two cameras, C2 and C3.

6.4.   Pressure Sensor Layout

The pressure sensors were laid in the bottom layer between the roughness glass spheres, to record variations in the flow motion nearby the entrained particle. The arrangement consists of 24 pressure sensors, 17 drag and 7 lift, as shown in figure. Those are settled in a cross shape around the target particle in the two main directions: stream-wise and span-wise.

In the analysis of this thesis project the pressure sensors were not considered, but they were useful in the whole research project, to match the pressure variations with the velocities vectors obtained from the PIV analysis.
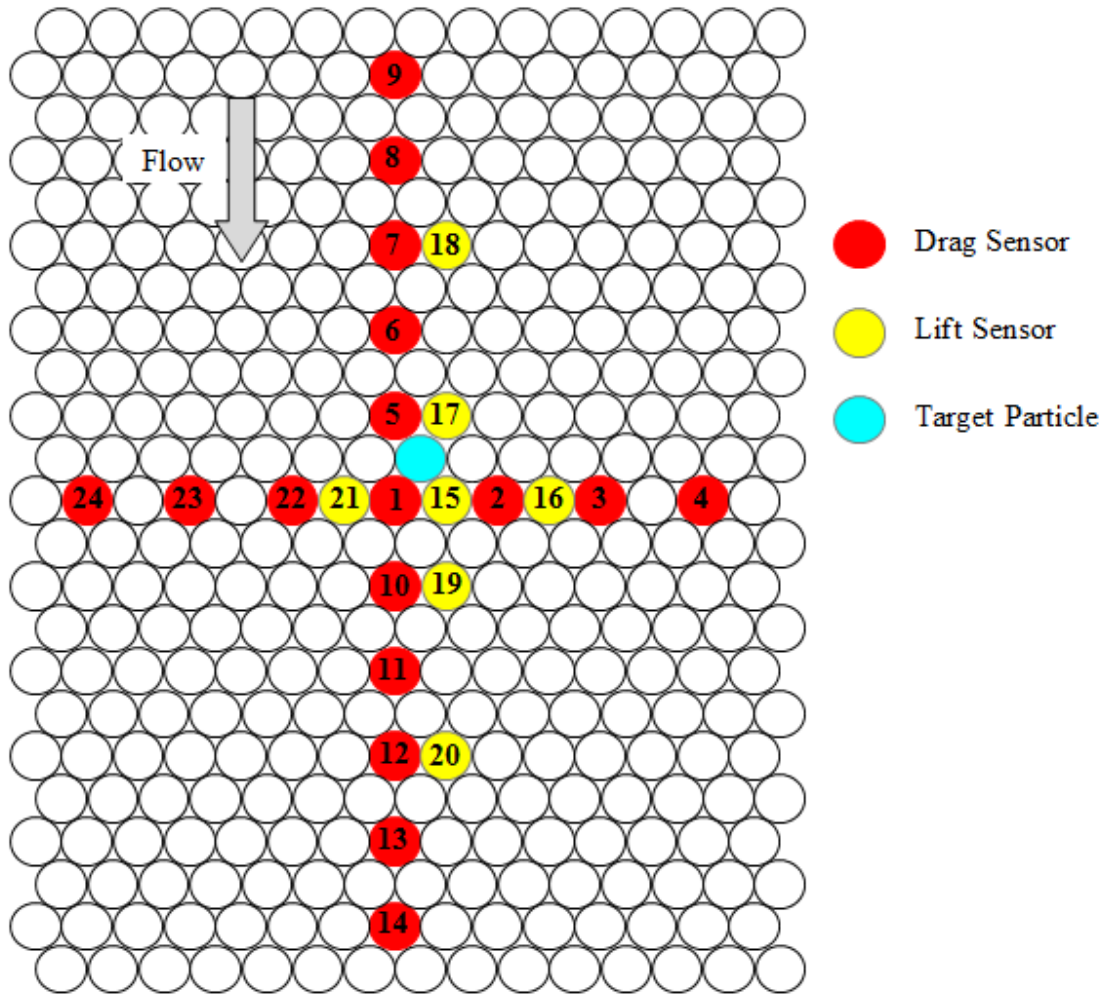
Figure 6-6 Arrangement of pressure sensors.

7. Experimental analysis and results

The thesis project is focused on the motion of the entrained particle and it's divided in two main sections. The first concerns the study of the erosion time's probability, the second deals with the tracking of the moving particle during the erosion process.

7.1. Erosion Time's Probability

In order to investigate the probability of the erosion time, a large sample of entrainments was simulated in the lab. Every combination of target particle density and flow rate was studied for protrusion influence, with the purpose of finding out the right condition to have a definite mean time of entrainment. The chosen mean times are 40 s, 120 s, 200 s, for each combination of flow rate (H,E,A) and target particle density (D,N).

Target Particle Protrusion (mm)						
				Mean Time (s)		
Run	H (m)	H/d	Ball	40	120	200
H	0,120	7,500	D	6,680	6,450	6,120
H	0,120	7,500	N	1,920	1,650	1,550
E	0,070	4,375	D	7,040	6,660	6,540
E	0,070	4,375	N	2,250	2,050	1,750
A	0,030	1,875	D	8,140	8,050	7,550
A	0,030	1,875	N	2,820	2,670	2,600

Table 7-1 Protrusion – Mean Time Summary Table

Afterwards, for each one of these combinations a sample was collected whose size was at least one hundred entrainments. In order to do this, experiments were performed in different days and considering reliability only the events of erosion occurred at least after 10 seconds from the settling of the target particle.

To ensure that the samples collected in different days for the same parameters set belong to the same statistical distribution, they were checked with a statistical test over them. Namely, a Kolmogorov-Smirnov test was performed between two samples.

Comparing the values shown on the Table 7.1-1, it can be seen that the big protrusion's influence on the erosion's mean time with other conditions being equal. The bigger density of Delrin is useful for the particle stability, so for reaching the same erosion's mean time it has to be settled in a higher position in relation to the roughness bed tops. The submergence of the ball is another factor that can help to grow the destabilizing forces on the sediment, indeed the flow's depth influences the velocity flow profile.
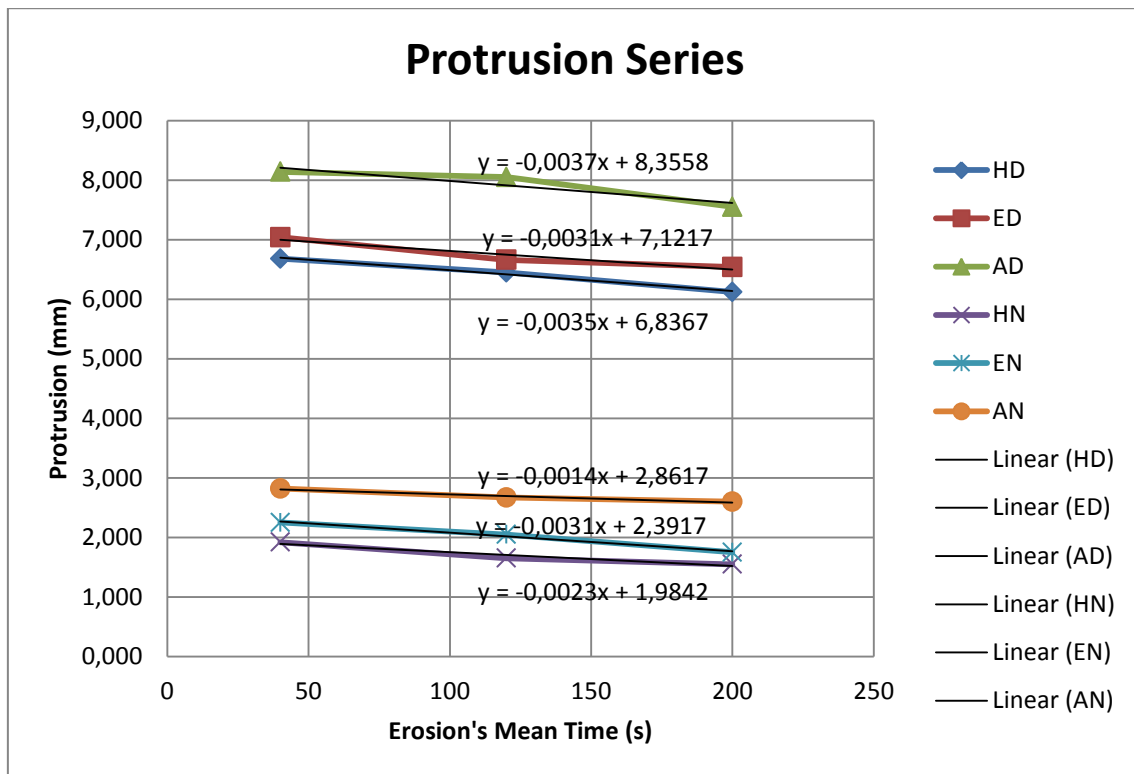
Figure 7-1 Protrusion series graph (summary graph) and related linear trend line.

The linear trend line in the Protrusions Series graph, for each dataset, seems to have the same slope for each sediment density. For Delrin tests the slope value on the mean time - protrusion is approximately -0,0034 mm/s and for Nylon seems around -0,0023 mm/s. This behaviour can indicate a major influence of the protrusion's value in the heavier particles that are more stable to the flow forces.

7.1.1. Statistical distribution

The samples obtained were statistically analysed, and a frequency distribution graph was created. Looking at the sample's erosion time frequency distribution it is easy to note a recurrent shape. In a second place some simple theoretical pdf's (probability density function) were taken into consideration and compared to the sample ones with the purpose of describing the same behaviour.
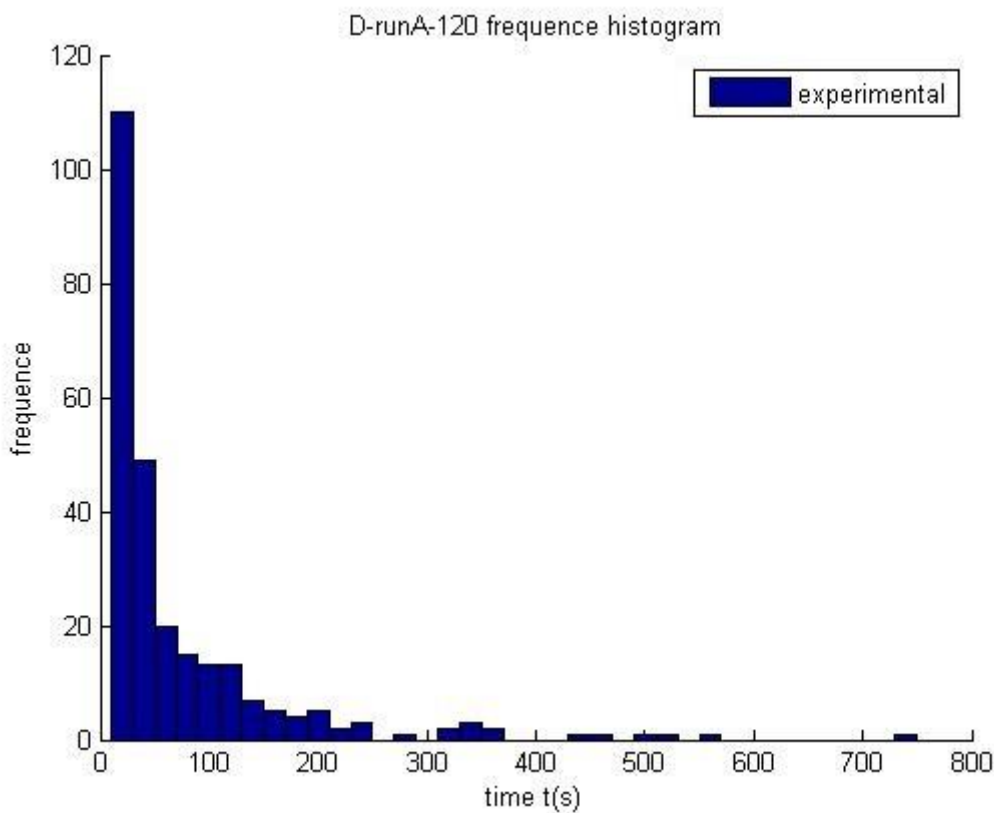
Figure 7-2 Frequency distribution histogram: Run A, Delrin, Mean Time=120 s.

Above are presented the theoretical pdf distributions:

- Exponential distribution $\quad\quad f(x) = \frac{1}{\mu} e^{-\frac{x}{\mu}}$

- Poisson distribution $\quad\quad\quad\quad f(x) = \frac{\mu^x}{x!} e^{-\mu}$

- Power's Law distribution $\quad\quad f(x) = cx^{-a}$

$$a = 1 + \frac{n}{\Sigma_1^n \, ln\left(\frac{x}{x_{min}}\right)} \quad\quad c = (a-1)x_{min}{}^{a-1}$$

It is important to remember at the time of implementing these distributions that the samples were obtained discarding the erosion events quicker than ten seconds.
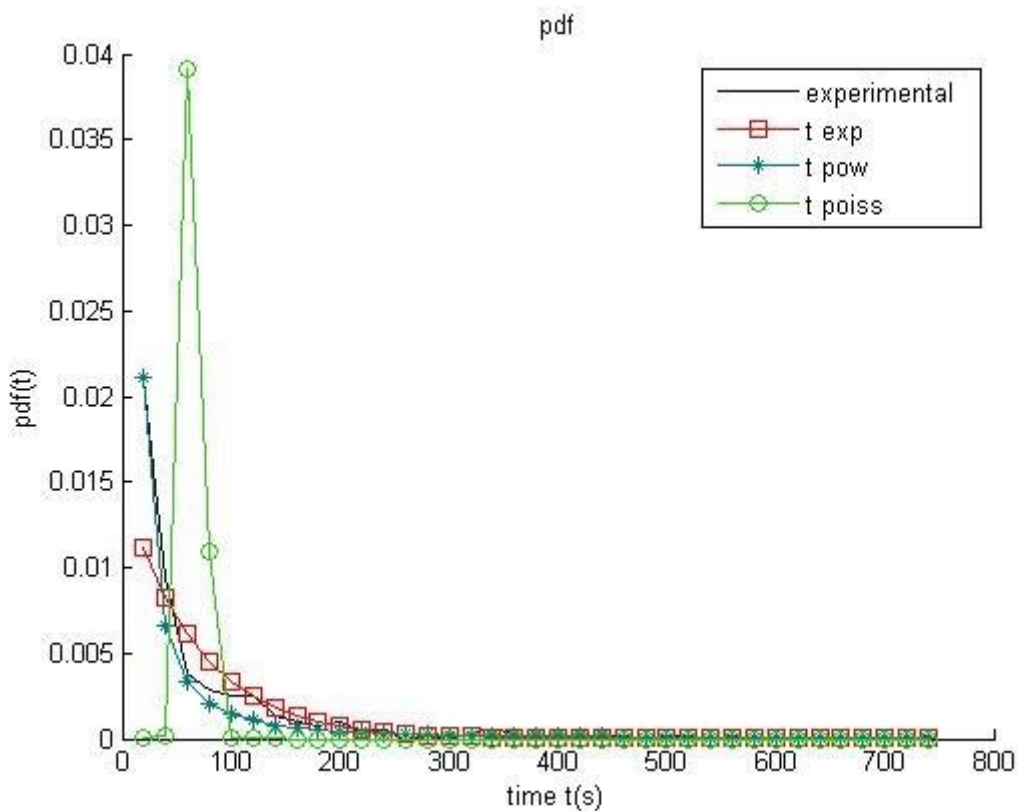
Figure 7-3 Comparison between experimental theoretical pdf: Run A, Delrin, Mean Time=120 s.
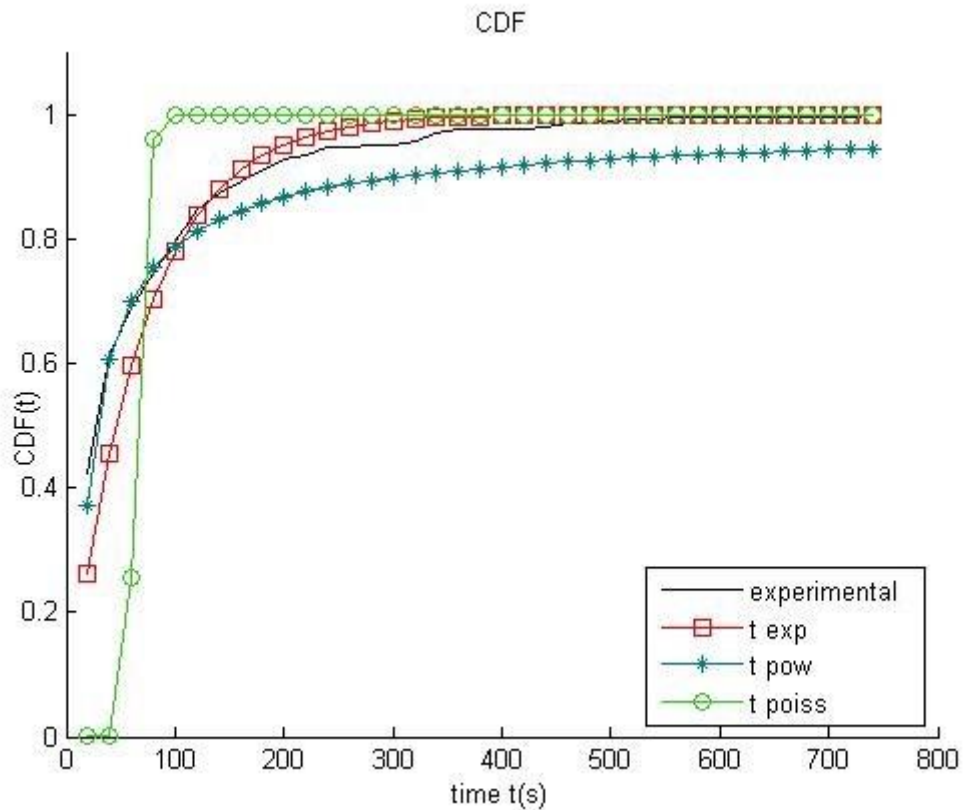
Figure 7-4 Comparison between experimental theoretical CDF: Run A, Delrin, Mean Time=120 s.

After some comparisons between distributions, the exponential one was taken to describe the experimental sample. This is due to the better matching and its simplicity; it only needs one parameter, the sample mean.

7.1.2.   Comparisons

These analyses can be matched with the occurrence probability of a turbulent phenomenon in the flow with the minimum intensity able to lift the target particle and start its motion into the channel flow. In relation to this it is useful to have a look to some comparisons between different erosion's mean times for the same flow and particle.
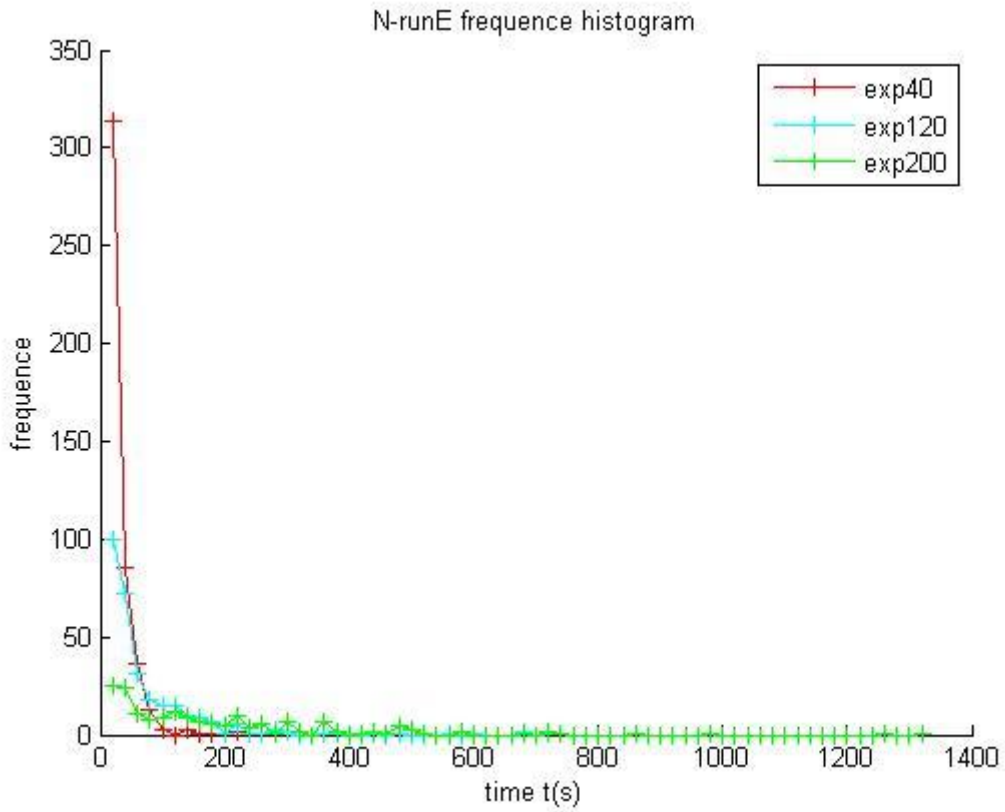
Figure 7-5 Frequency distribution graph: Run E, Nylon, Mean Time comparisons.
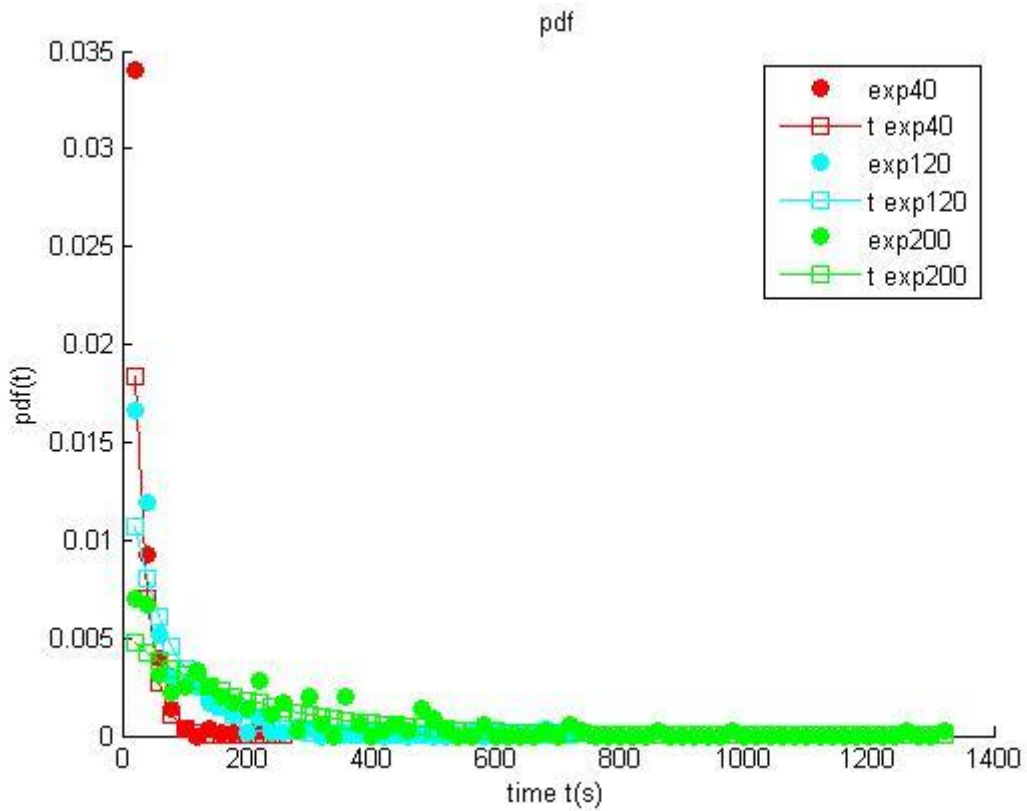
Figure 7-6 Mean Time comparisons, Pdf graph: Run E, Nylon.
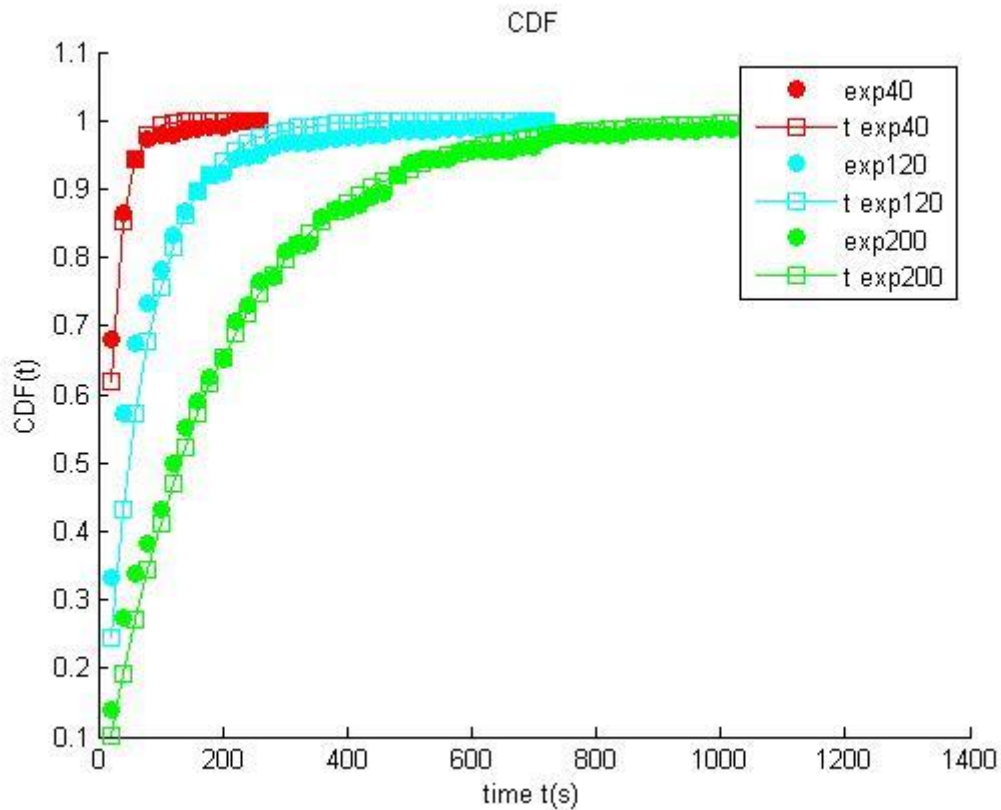
Figure 7-7 Mean Time comparisons, CDF graph: Run E, Nylon.

From the previous figures it is evident that protrusion of the target particle is very influent on the erosion mean time. The difference between the protrusions is very small, and this controls the particles erosion time.

Target Particle Protrusion (mm)				
		Mean Time (s)		
Run	**Ball**	40	120	200
E	N	2,250	2,050	1,750

Table 7-2 Protrusion Summary Table, Run E, Nylon

The particle protrusion is an indicative value for describing the particle exposed area to the flow motion. The drag and lift forces are more intense on the particle with higher protrusion's values due to the bigger exposed area. It can be stated that the same turbulent event that is strong enough to move the stone with the higher protrusion, it may be less intense for a protruded particle. In this way we

can analyse the occurrence probability for a turbulent event greater than the critical one, for a precise combination of flow, particle and protrusion.

Analysing the same mean time for different data series it is clear that they follow the same distribution, pointing out a wider deviation from the exponential distribution for the higher erosion's mean time.
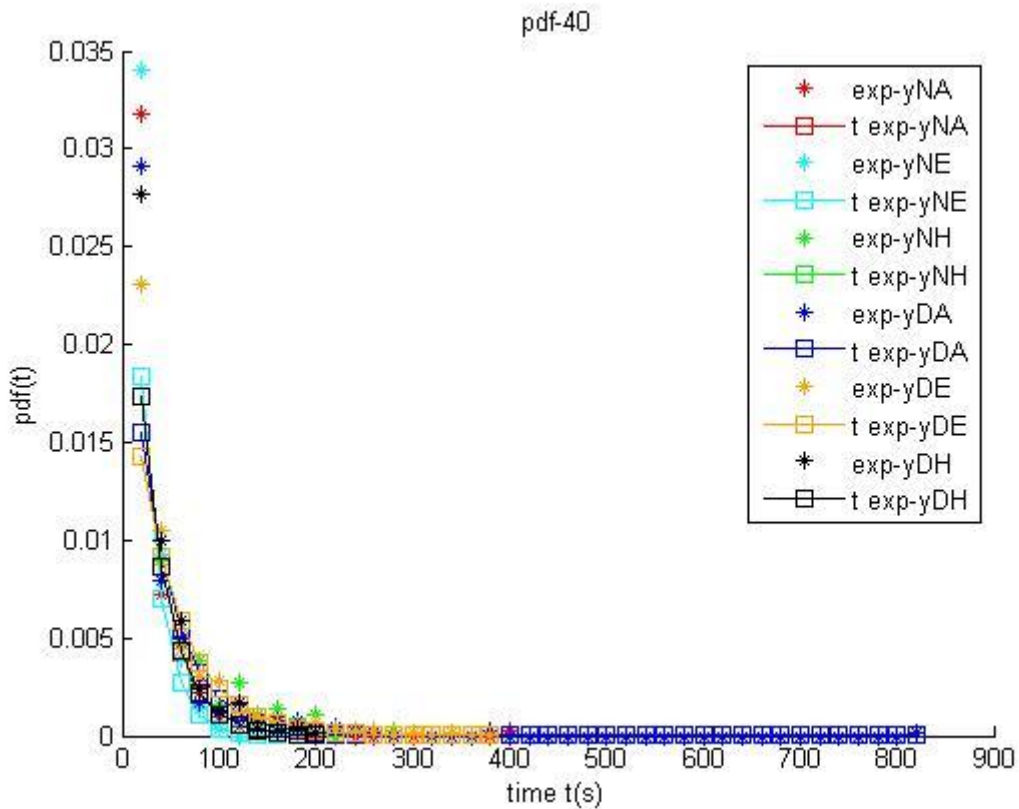
Figure 7-8 Comparisons pdf graph, erosion's mean time 40 s
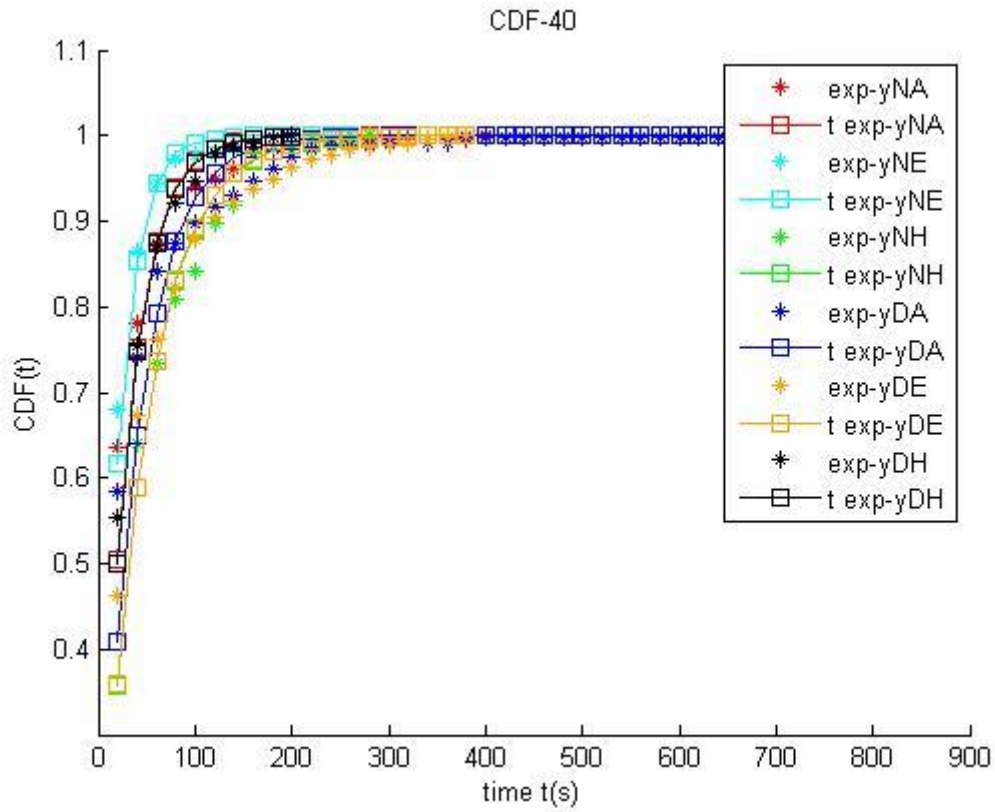
Figure 7-9 Comparisons CDF graph, erosion's mean time 40 s
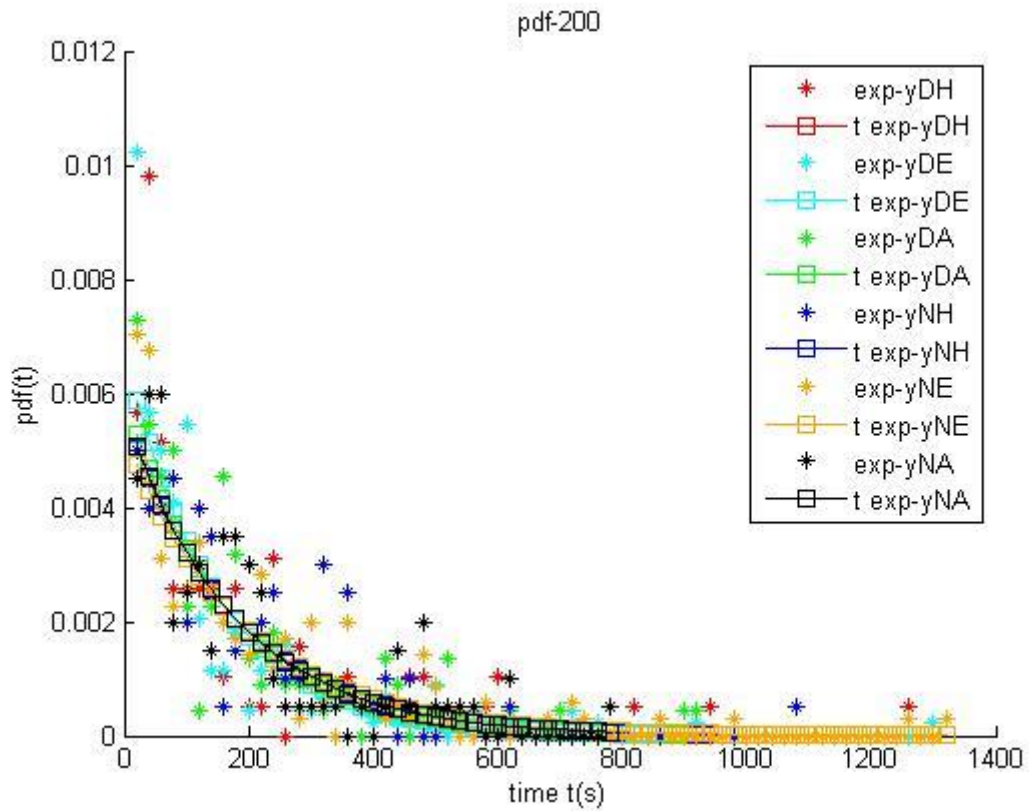
Figure 7-10 Comparisons pdf graph, erosion's mean time 200 s
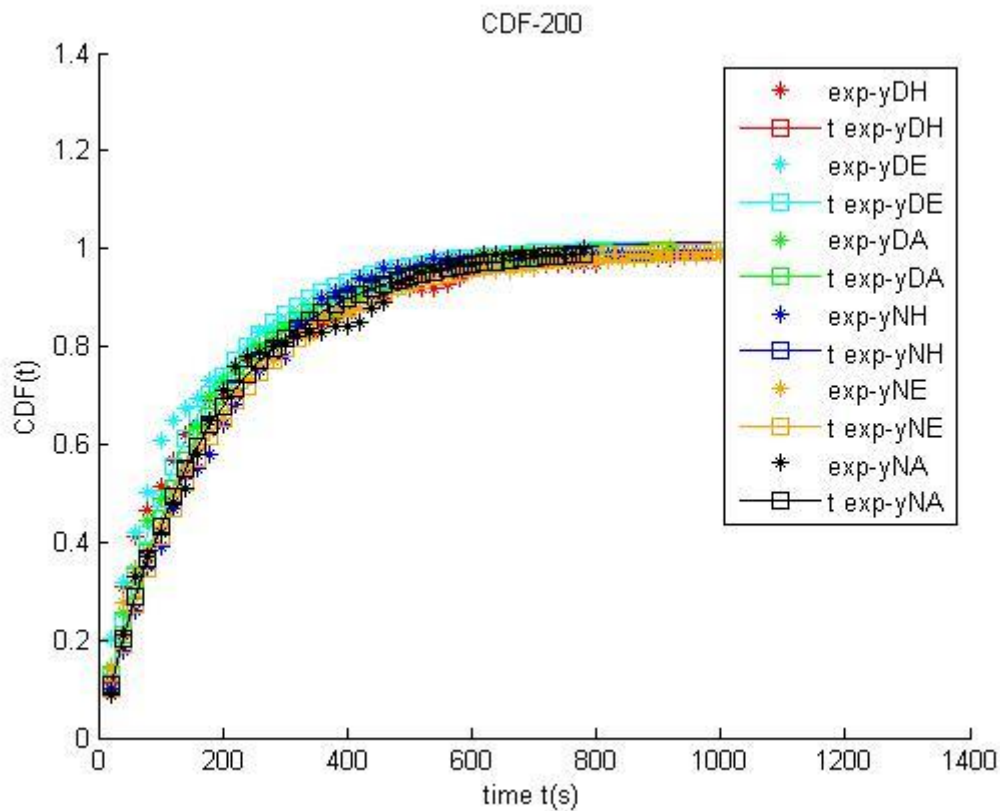
Figure 7-11 Comparisons CDF graph, erosion's mean time 200 s

In the previous graphs all the distributions are from different datasets but with equal erosion mean times and they are arranged on the same curve, in the CDF graphs this is more evident. On pdf graphs the biggest scattering of the data in samples is the erosion's mean time of 200 s instead of the ones with 40 s.

7.2. Particle Tracking

This second part of the thesis concerns the particle's tracking process. The samples used in this section are smaller than previous due to the large amount of data required from the PIV system to develop the particle motion tracking.

While monitoring the flow motion with the PIV method, the particle can also be studied, tracking its movements during the time when it is still in the laser light

plane. As for the flow, the cameras in PIV system can record the motion of the stone enlightened by the laser and combining the images from different cameras the sediment path can be obtained.

7.2.1.   Data sets

The purpose of this experiment set was to look into different flow conditions (H, E, A), using the two different sediments, Nylon (N) and Delrin (D) previously described, but this time the protrusion was set for having always the same mean time of entrainment (120 s) for all those tests. The bed packing was still arranged with one layer of marbles in Hexagonal Close Packing (HCP-1). The PIV mode 6 (Cam 2 and Cam 3 with stream-wise laser light) was used in the following tracking.

The tests used in this thesis are only a part of the initial data set, because the PIV elaboration required a long time to develop its results. Therefore taken into consideration the full data set for Delrin to compare different flows and the run H with Nylon to have some results with different particle density.

The captions process of the laser system is increased in frequency lowering the water flow due to having more information in a smaller depth creating a small controlled section.

PIV-mode	Run	H(m)	dt (L1-L2) (ms)	freq. L1 (Hz)	T (ms)
6	H	0,12	2,10	32	31,25
6	E	0,07	2,10	50	20,00
6	A	0,03	3,00	100	10,00

Table 7-3 Laser system caption sets.

Test Scenario	Run	Packing	PIV Mode	Repitions	rp/rf	D, m	H/D	Sb	П/D	Re*	B/H	Re_b	Re_τ	Fr	Q, m3/s	H, m	U, m/s	u^*, m/s
1	A	HCP-1	6	25	1,11	0,016	1,875	0,00600	0,160	672	39,3	10683	1261	0,66	0,0126	0,030	0,356	0,042
2	A	HCP-1	6	25	1,37	0,016	1,875	0,00600	0,483	672	39,3	10683	1261	0,66	0,0126	0,030	0,356	0,042
3	E	HCP-1	6	25	1,11	0,016	4,375	0,00257	0,117	672	16,9	28699	2941	0,49	0,0339	0,070	0,410	0,042
4	E	HCP-1	6	25	1,37	0,016	4,375	0,00257	0,417	672	16,9	28699	2941	0,49	0,0339	0,070	0,410	0,042
5	H	HCP-1	6	25	1,11	0,016	7,5	0,00150	0,098	672	9,8	53839	5043	0,41	0,0635	0,120	0,449	0,042
6	H	HCP-1	6	15	1,37	0,016	7,5	0,00150	0,391	672	9,8	53839	5043	0,41	0,0635	0,120	0,449	0,042
7	H	HCP-1	6	25	1,37	0,016	7,5	0,00150	0,394	672	9,8	53839	5043	0,41	0,0635	0,120	0,449	0,042
8	H	HCP-1	6	25	1,37	0,016	7,5	0,00150	0,412	672	9,8	53839	5043	0,41	0,0635	0,120	0,449	0,042
9	A	HCP-1	3	25	1,11	0,016	1,875	0,00600	0,161	672	39,3	10683	1261	0,66	0,0126	0,030	0,356	0,042
10	A	HCP-1	3	25	1,37	0,016	1,875	0,00600	0,484	672	39,3	10683	1261	0,66	0,0126	0,030	0,356	0,042
11	E	HCP-1	3	25	1,11	0,016	4,375	0,00257	0,110	672	16,9	28699	2941	0,49	0,0339	0,070	0,410	0,042
12	E	HCP-1	3	25	1,37	0,016	4,375	0,00257	0,416	672	16,9	28699	2941	0,49	0,0339	0,070	0,410	0,042
13	H	HCP-1	3	25	1,11	0,016	7,5	0,00150	0,099	672	9,8	53839	5043	0,41	0,0635	0,120	0,449	0,042
14	H	HCP-1	3	15	1,37	0,016	7,5	0,00150	0,387	672	9,8	53839	5043	0,41	0,0635	0,120	0,449	0,042
15	H	HCP-1	3	25	1,37	0,016	7,5	0,00150	0,394	672	9,8	53839	5043	0,41	0,0635	0,120	0,449	0,042
16	H	HCP-1	3	25	1,37	0,016	7,5	0,00150	0,410	672	9,8	53839	5043	0,41	0,0635	0,120	0,449	0,042

Table 7-4 Entrainment Run Table

This table reports the whole set of entrainments planned for the PIV monitoring, but this second part of the thesis deals with only four of them corresponding to the Test scenario numbers 2, 4, 5, 8.

7.2.2. Tracking issues

After getting the images form the camera system, the aim at this stage of the experiment was to clearly identify the flow field, to continue with the PIV analysis. This was done to separate the flow enlightened by the laser form the rest of the image in each frame of each video. It involves also to locate precisely the particle in the frames and to take into account the shadow created by the laser light.

For those tasks the software SlugFlow was used to detect the target sediment during a small video cut off aiming at the entrainment event. The blurred video from the camera produced after the process of detection was a tracking time series file with the position of the particle's center and its radius seen during the time in the frames. But those files were not ready to be processed in the next stage due to problems with the video analysis. Videos presented some problems for good software detection.

Figure 7-12 (Cam2, Run E, Delrin) Image of particle settled in the flow bottom at his protrusion before entrainment, on the right the same particle after the particle detection, showing with the blue lines the target sediment and an area behind it for limiting the shadow flow field.
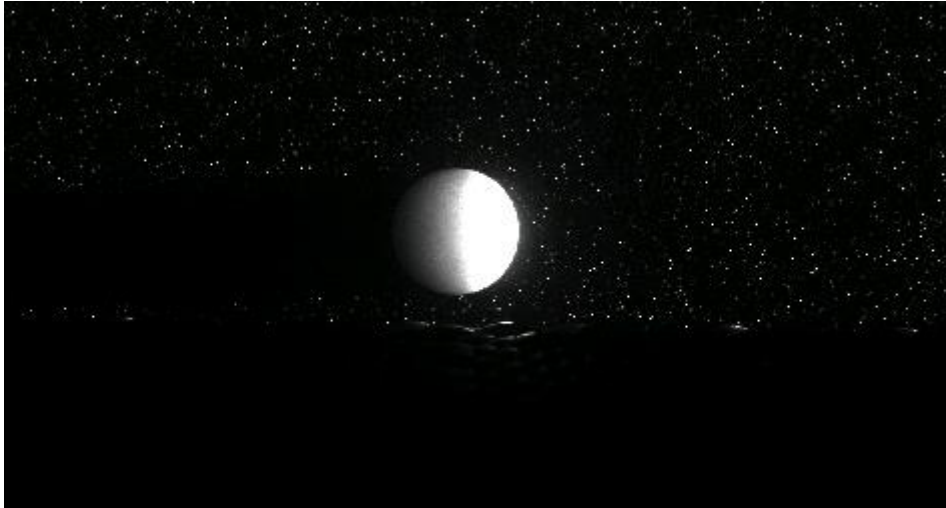
Figure 7-13 (Cam2, Run E, Delrin) Image of particle motion

Ball movements outside the laser sheet far from the camera caused a scattering phenomenon of the laser beam light over the particle, so the light gradient used for locating the sediment in the images was not large enough between the edge of the particle and the flow.

Figure 7-14 (Cam2, Run A, Delrin) Scattered light phenomenon

On the other side, the ball moving too close to the camera created a shadow by screening the laser light and reflecting most of it on the opposite side of the channel.
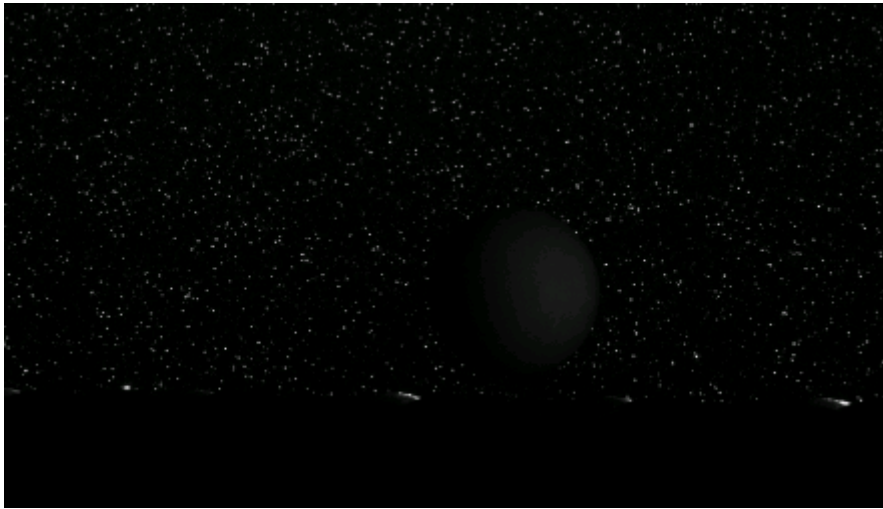
Figure 7-15 (Cam2, Run E, Delrin) Screening light phenomenon

Moreover, sometimes the software locates multiple balls on the images or it doesn't perform any detection cause of those issues about the laser light.
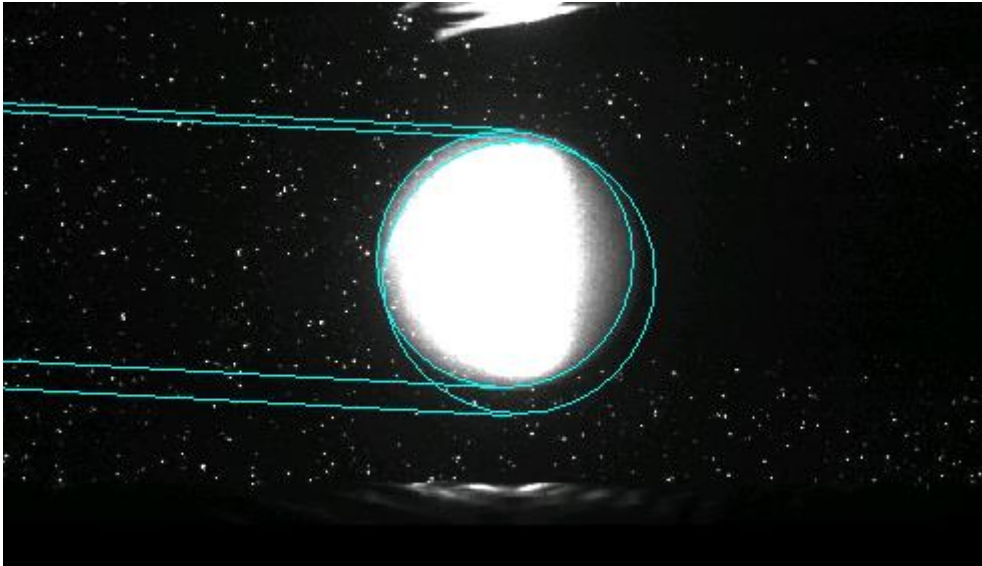
Figure 7-16 (Cam3, Run A, Delrin) *Multiple balls detection*

Figure 7-17 (Cam2, Run A, Delrin) No detection

The location of the ball had to be checked and changed manually for those frames that presented some problems in order to perform a clear tracking of the particle. After a correct detection of the ball position, it had to be developed also the location the non-fluid field area had to be developed. This simply implies to set a good radius in the ball tracking part and to set the right angle to indicate the direction of the ball's shadow cone.
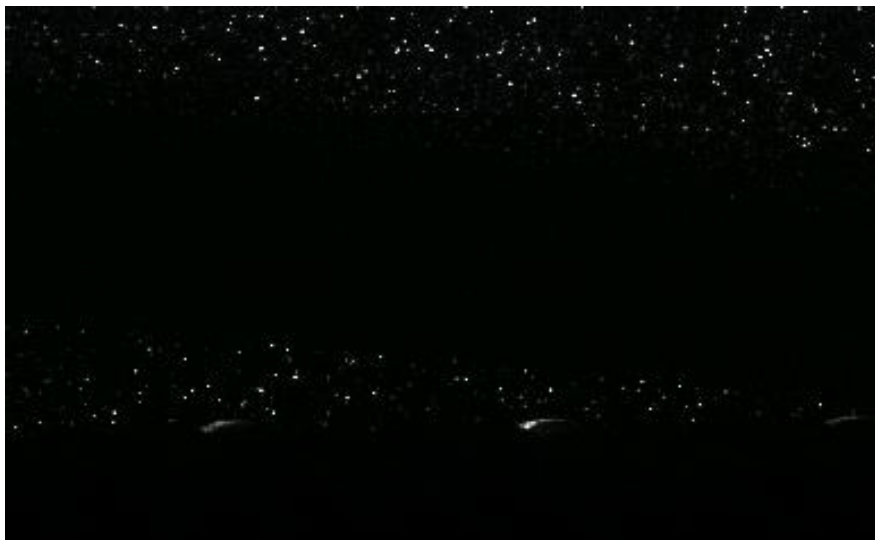
Figure 7-18 (Cam3, Run H, Delrin) Shadow cone

Figure 7-19 (Cam3, RunH, Delrin) Ball detection without shadow area location
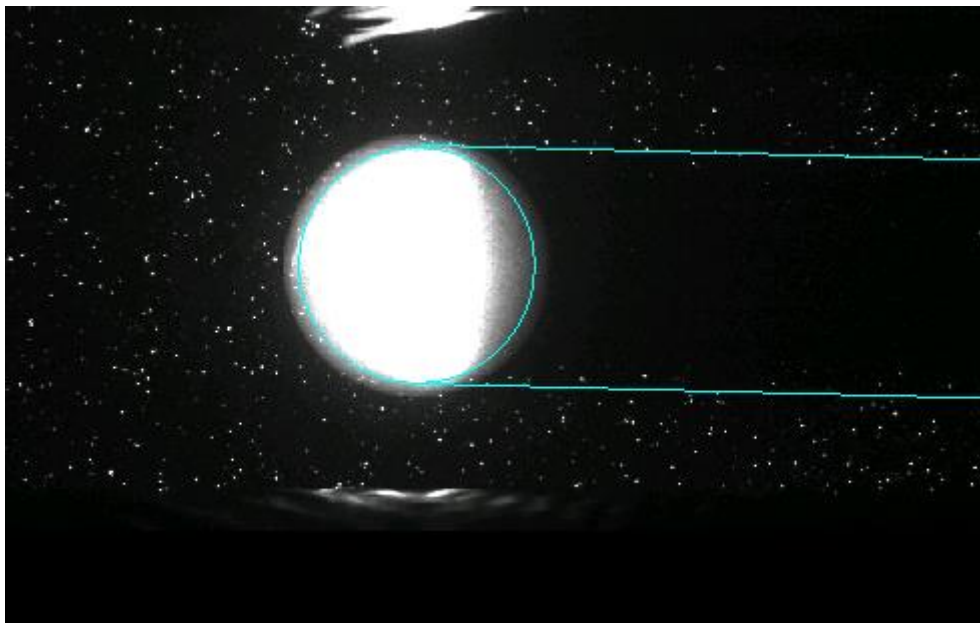
Figure 7-20 (Cam3, Run A, Delrin) Frame tracking complete

Finally, the entrainment records can be processed by the software to obtain the PIV method, the flow field motion over the control section monitored by the camera system and shown by the laser system, those data also produced the full tracking of the particle moving into the controlled area.

7.2.3.   Tracking analysis

With the position of the particle paths over space in the event of entrainment, it is useful to look at its velocity and acceleration to get a complete description of its motion. To do this, a few different methods of computation were used.

First of all, for a better use of the information collected by the use of two laser impulses, it is useful to consider the fact that between the two impulses there is a very short time in comparison to the single laser impulse period. Therefore it is better to avoid those data as a single time series, but as two different records of the same event of entrainment averaging the position between the two lasers impulse caption. This way also the systematic errors occurred in the tracking can be averaged.
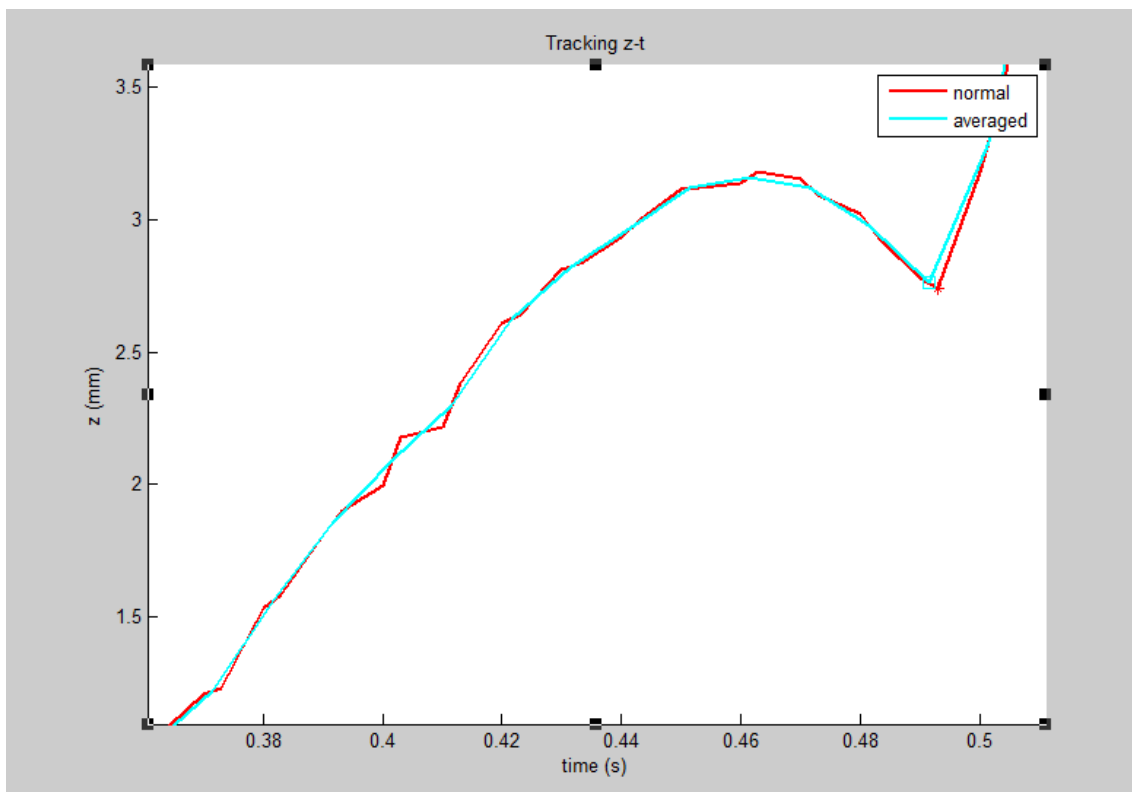

Figure 7-21 Graph position z-t, differences between normal and averaged analysis, the averaged results more smooth and describes a clear path.

Afterwards, to get the velocity out of the position during time there are different methods as the direct method or the central finite difference method.

The direct one is computing the ratio between the displacement and its own the time gap from two close point, but this way the result would be an average velocity for a time in the middle of that short period. Using the central finite difference method the instant taken into consideration would be from both side of the analysed point, and the velocity would be referring to the same instant of the position. This method can be used with different orders of accuracy, that means to consider more point close to the analysed one and it also can be used to compute derivate with different order.
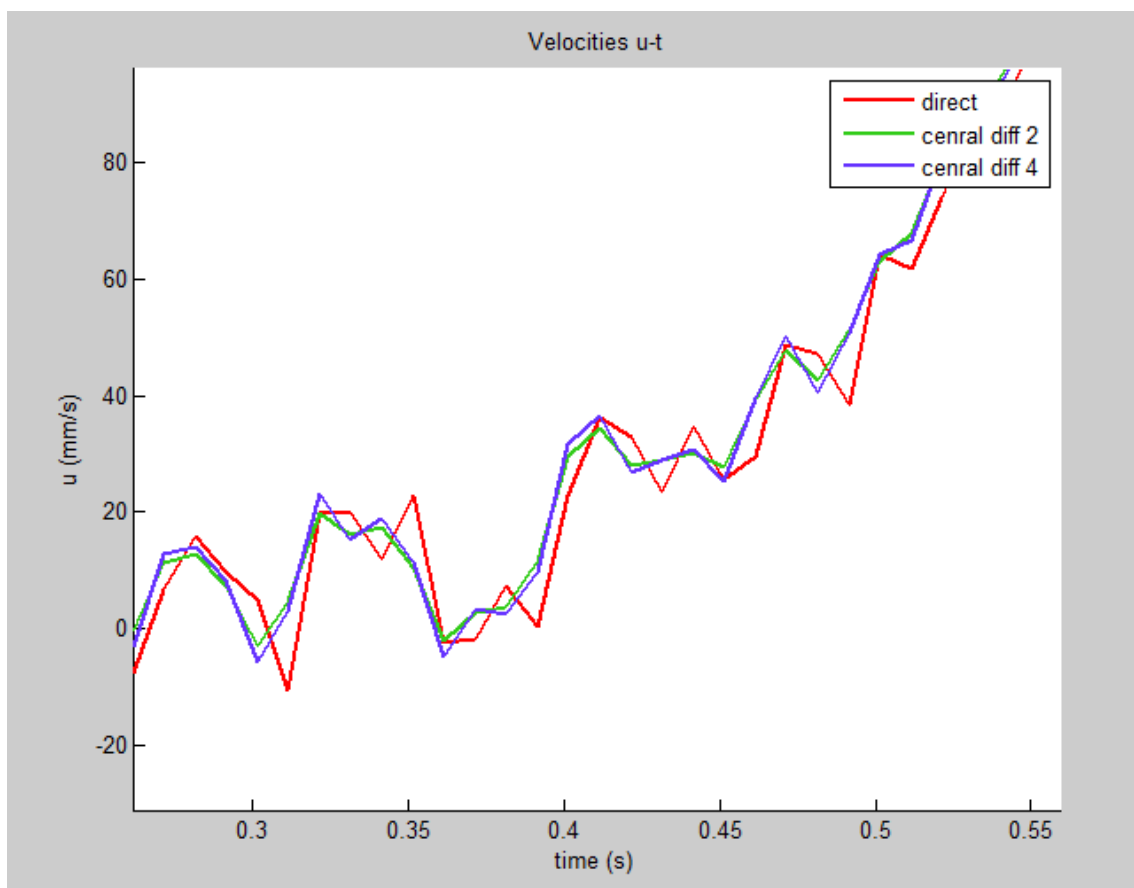

Figure 7-22 Graph position u-t, differences between direct method (red) and central finite difference method with second (green) and fourth (blue) order of accuracy, the green line results more smooth and it's more close to a continuous line

63

The rest of the analyses hereafter are carried out using an average between the lasers position time series, and using the central finite difference with a second order of accuracy for computing the second derivate and acceleration.

Looking into the paths described by the particles, it can be seen that the motion type of the particles describe the typical wavy path of a saltation motion, for this type of trajectory jumps can be detected and analysed by computing their height and length.
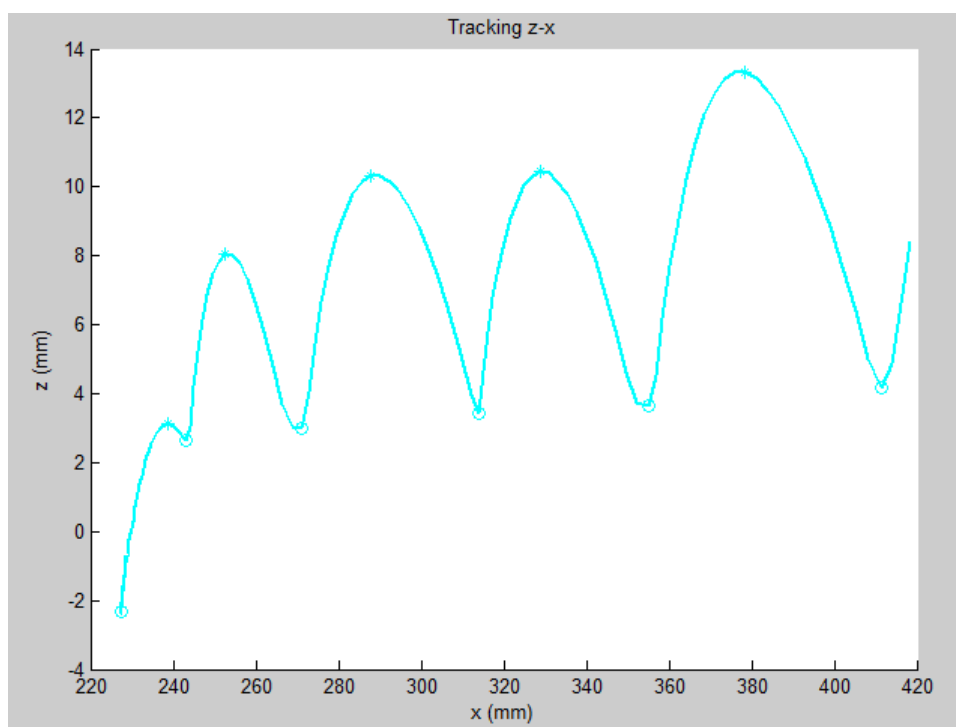
Figure 7-23 Graph position z-x, showing the particle saltation motion and the detection of the jumps limits '*o*' and tops '*∗*'.

The jumps detection was carried out with a simple check on the z-position over time, taking into account those close variations big enough to describe the line concavity. The criteria were developed considering a variation of 0.4 mm more on z-direction for both side, before and after each point, or a second condition checking the increment of z-position immediately before and after and on at least one side a successive variation of more than 0.6 mm.

Definition of jump used in the detection script:

64

$$z(i-1) - z(i) > 0.4\,mm \ \wedge \ z(i+1) - z(i) > 0.4\,mm$$

$$z(i-1) - z(i) > 0\,mm \ \wedge \ z(i+1) - z(i) > 0\,mm \ \wedge \ z(i-2) - z(i) > 0.6\,mm$$

$$z(i-1) - z(i) > 0\,mm \ \wedge \ z(i+1) - z(i) > 0\,mm \ \wedge \ z(i+2) - z(i) > 0.6\,mm$$

Those conditions were chosen as compromises between two needs to not to consider as jumps some fluctuations caused by noise in the data and at the same time to detect most of the real bounces.

7.2.4.   Results

The paths described by the particles motion are clearly a saltation motion type, as it can be noticed looking at the next graphs. This motion is controlled by the gravity forces and is carried out by the flow motion. At the beginning of the entrainment the trajectories seem the same but after few bounces on the bed layer, they start to deviate in a random way. This is obviously connected to the collisions over the flume bottom.

The following graphs use to plot the main quantities against position instead of time to avoid the problems that entrainments did not occur at the same time, but according to our data collection they started from the same position. This choice can show better the removing particles moments, most of the graphs represent "Run A" because it is the condition with the high record frequency, so it can show better the fluctuation and the general behavior of the entrainments.
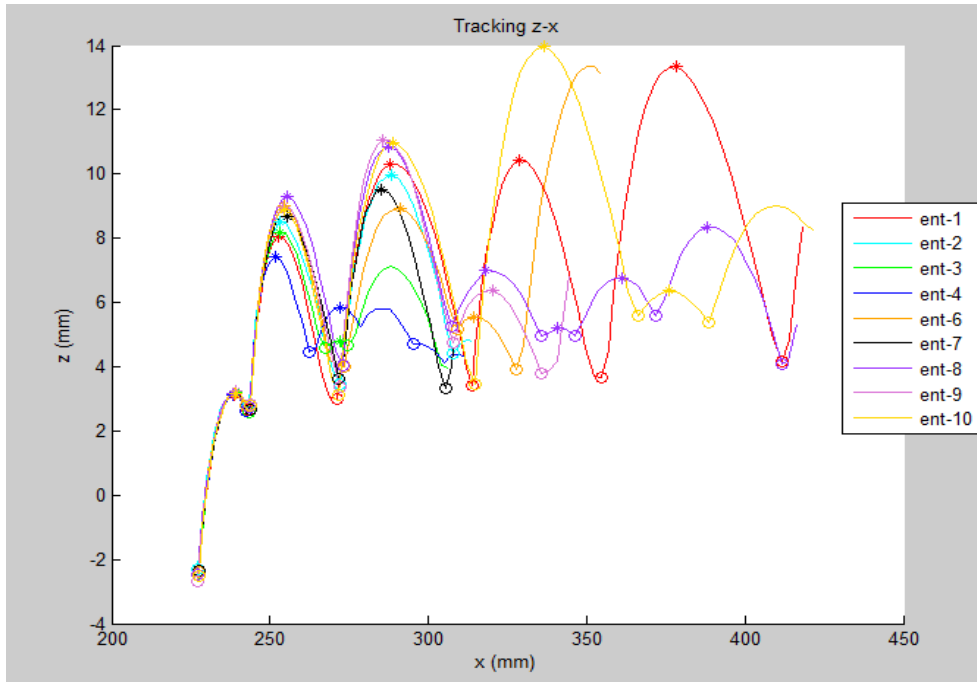
Figure 7-24 (Run A, Delrin) Graph position z-x, shows some entrainments paths, the typical wavy trajectory seems to be similar for all those tests.
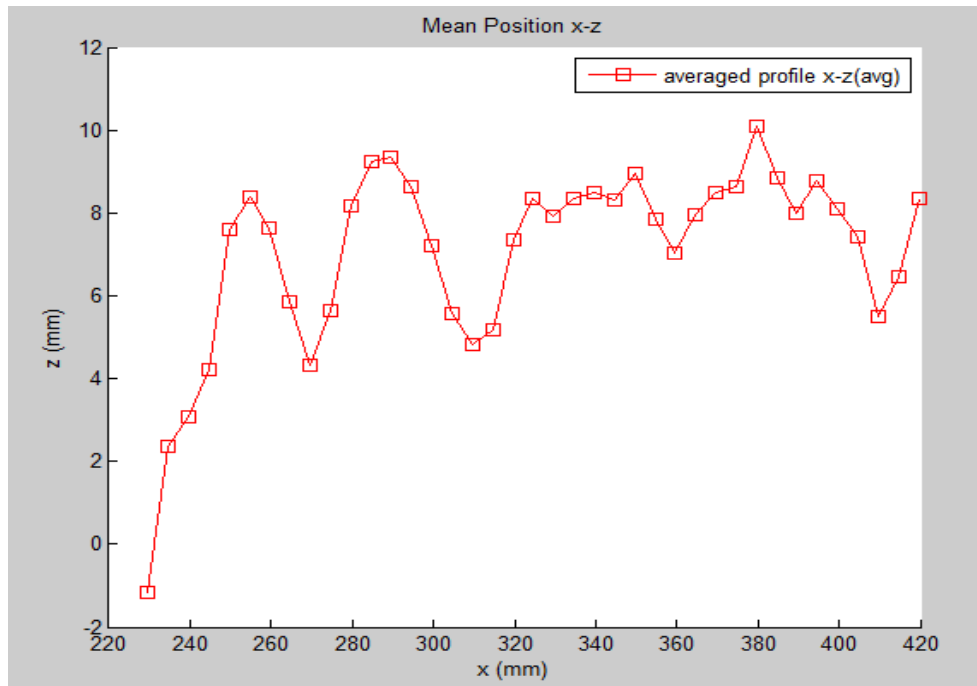

Figure 7-25 (Run A, Delrin) Graph position z-x, mean z-position in relation to x-position some entrainments paths, the trajectory is similar at the beginning for all those tests, and after it become more casual, so the mean position doesn't reflect the characteristic wavy trajectory.
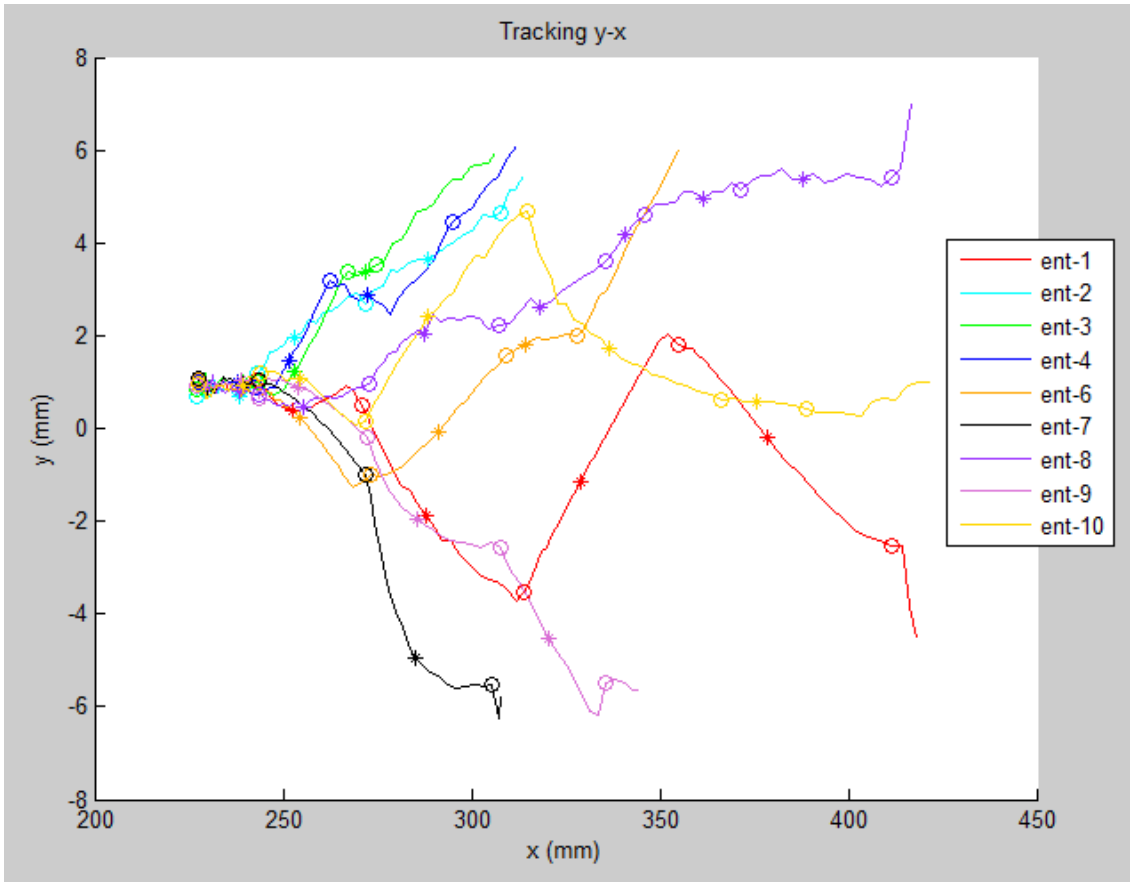
Figure 7-26 (Run A, Delrin) Graph position y-x, shows some entrainments paths, the random movement after the firsts bounces in a span-wise direction.

In the upward direction the motion is regulated by the gravity and this explains the slightly regular pattern of the particle motion, otherwise there are not such strong and persistent forces on the span-wise direction, so here the pattern is more random. It can be pointed out that collisions over the bed can change greatly the particle trajectories, and it is a random phenomenon, but also there are some path deviations that occur during the jumps, these can be attributed to the turbulence in the flow motion. Looking at the previous graph entrainments 7 and 10 present a deviation in the path not caused by any collisions, their shape is a smooth line that represents a continuous deviation; the alternative is that the turbulence caused that deflection. The rest of the deflections caused by collisions show a spike on the graph indicating an instantaneous change of direction.

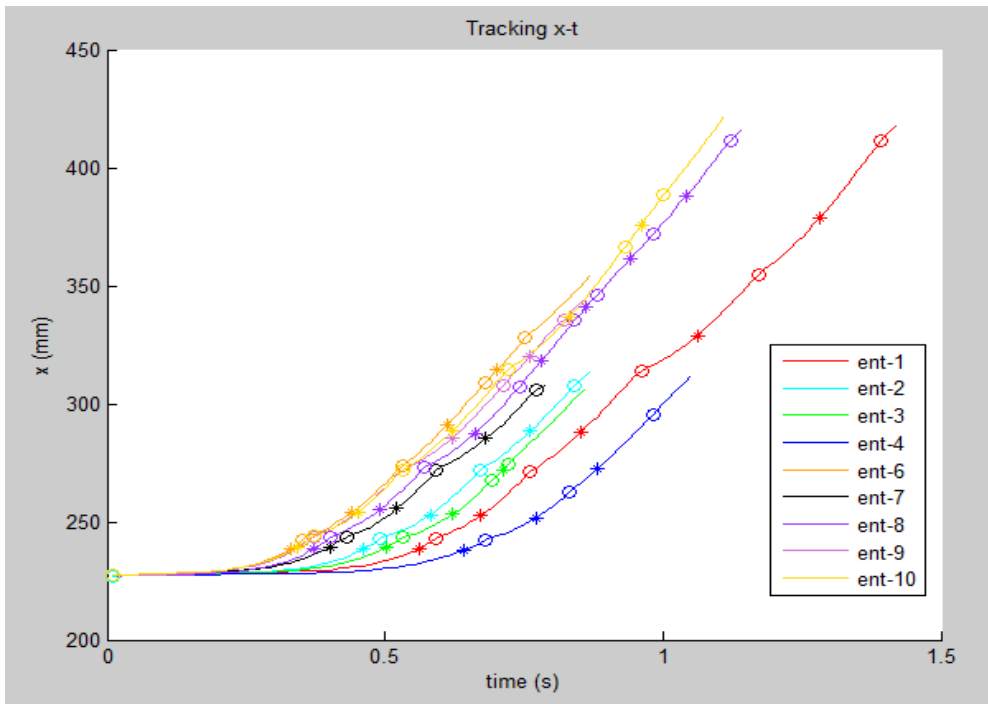*Figure 7-27* (Run A, Delrin) Graph motion x-t, shows x-movements over time, the slope of those lines after the motion start show the trend to keep the same velocity.
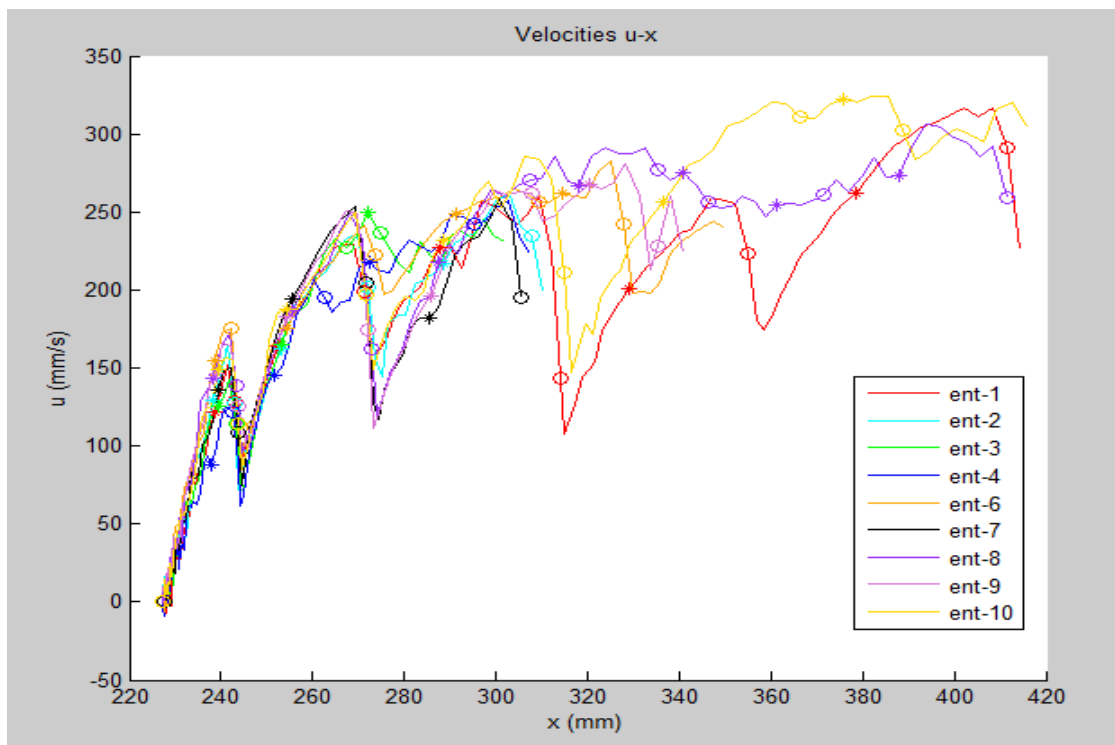
Figure 7-28 (Run A, Delrin) Graph motion u-x, shows u-velocities over x-axis, after entrainment the trend is to keep the same u-velocity, in this case close the value of 250 (mm/s).

The particles are brought downstream by the flow, so they all tend to take the same downstream velocity. The trajectory can suffer variation due to the deviations after the collisions. The variations of the stream wise velocity are still persistent due to the turbulence and the collisions but the mean value is increasing during the motion, it seems to stabilize to a certain value.

Velocities in relations to the upward direction are affected by a cyclic behaviour due to the collision process with the bottom. The w-velocities are positive before entrainment showing a clear lift of the particle and the u-velocities seem to grow with the z-position, following the flow motion upward that present a logarithmic velocity profile.
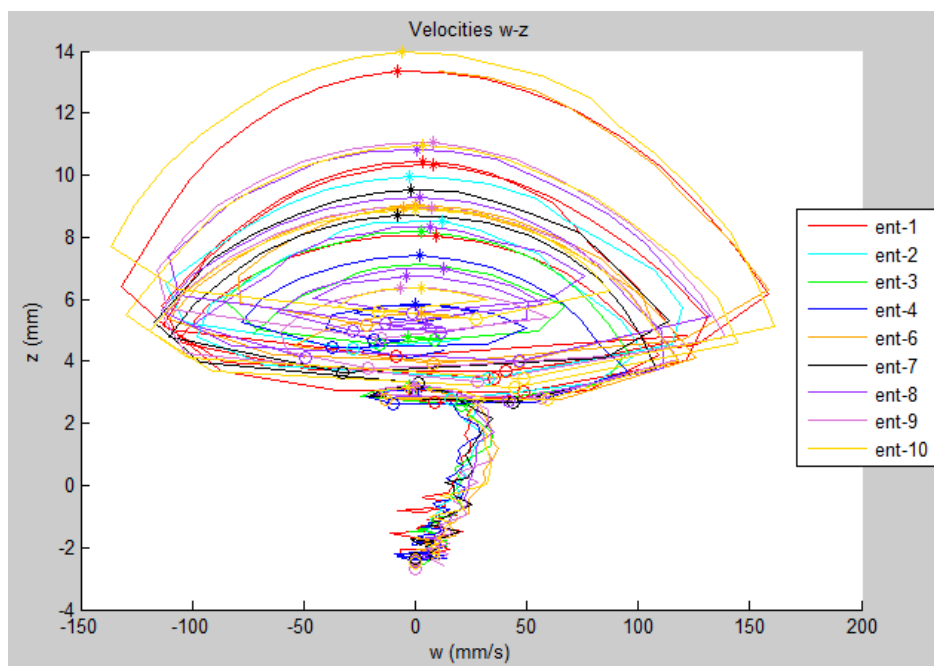
Figure 7-29 (Run A, Delrin) Graph motion z-w, shows w-velocities over z-axis, after entrainment the upward velocities are positive in the ascending part of the jumps and negative in the descending part of the jumps.
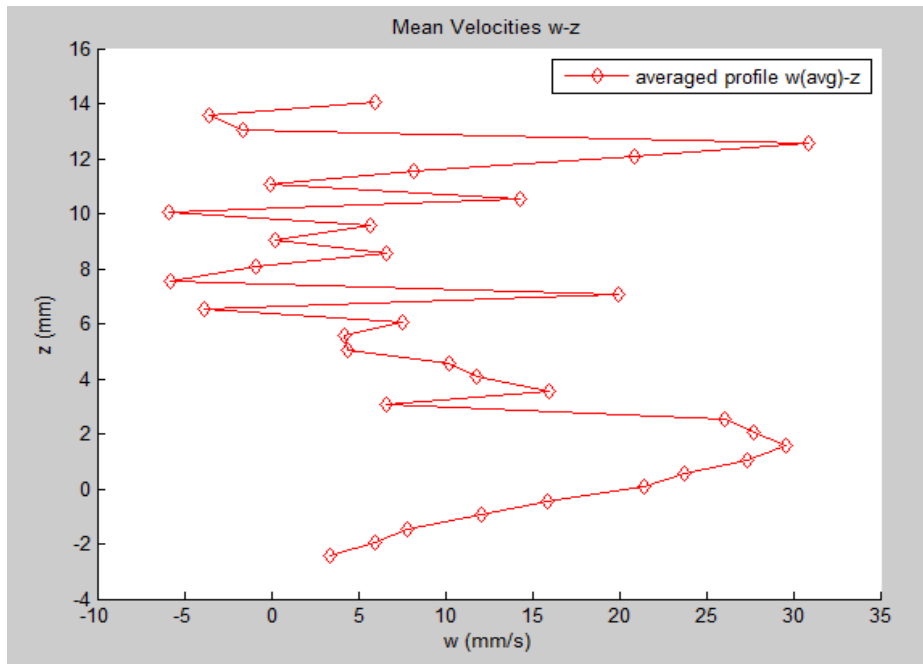
Figure 7-30 (Run A, Delrin) Graph motion z-w, shows the mean of w-velocities in relation to the z-position, upward velocities are clearly positive before entrainment under, for low z-position values, the rest is the result of the cyclic behaviour, the mean value is less and the distribution is more scattered.
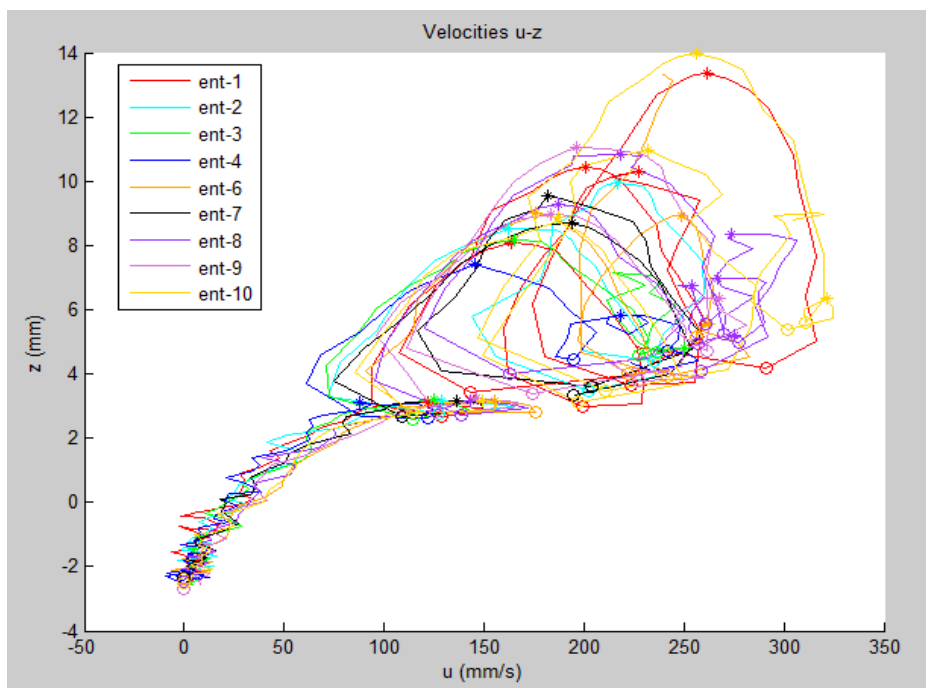
Figure 7-31 (Run A, Delrin) Graph motion z-u, shows u-velocities over z-axis, stream-wise velocities decrease a bit after the collisions and increase moving into the flow upwards.
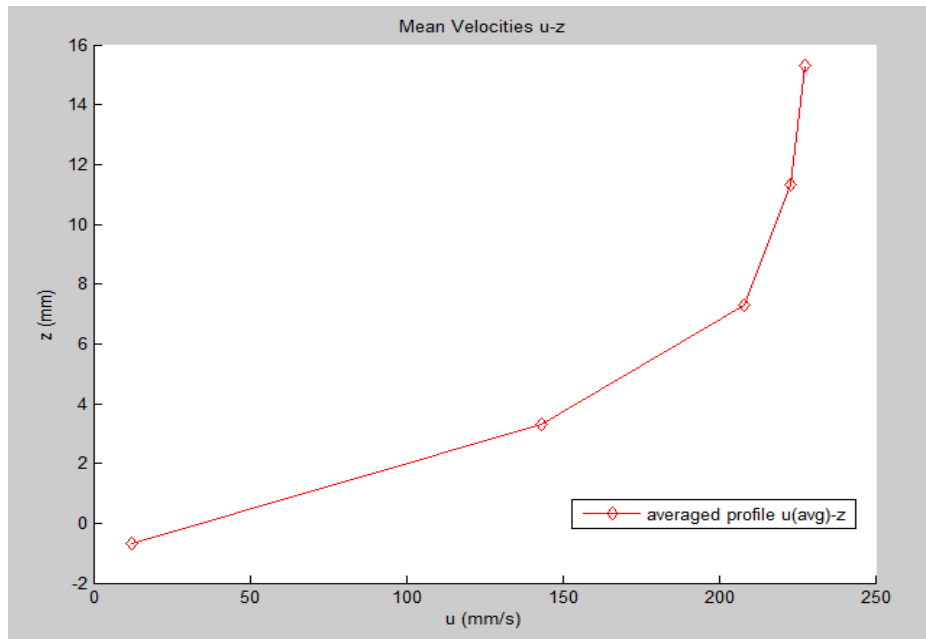
Figure 7-32 (Run A, Delrin) Graph motion z-u, shows the mean of u-velocities in relation to the z-position, stream-wise velocities increase moving into the flow upwards, they seem to describe a logarithmic profile.

The accelerations are the main indication of the forces on the ball, drag forces and lift forces. The flow has to remove the ball form the bottom layer with a magnitude event big enough to overcome its resistance. Looking at the accelerations graph we find out some turbulent force event on the particle before entrainment. In the x-accelerations graph, most of the peaks are negative cause of the collisions on the bed layer, "ent-9" present a positive peak in the collision, but checking the z-x graph the trajectory describe a short flat jump close to the bottom. The positive peaks occur because of the drag events. For the z-accelerations the collision peaks are positive for the almost instantaneous direction change on the upward velocities, the rest are a low magnitude events and the role of the lift forces is not evident in the mean-z-acceleration graph before entrainment.

Figure 7-33 (Run A, Delrin) Graph acceleration du/dt-x, shows x-acceleration over x-axis, most of the negative peaks are related to the collisions, the ball decrease the velocity.

Figure 7-34 (Run A, Delrin) Graph acceleration du/dt-x, shows mean x-acceleration in relation x-position, the section at the beginning is clearly positive due to a sweep event at the entraining point.
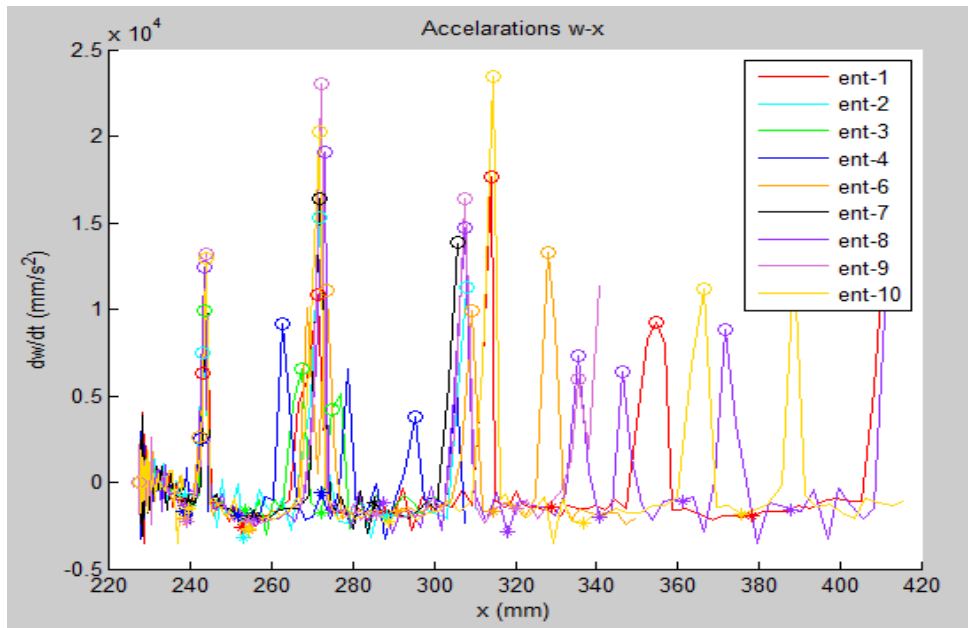
Figure 7-35 (Run A, Delrin) Graph acceleration dw/dt-x, shows z-acceleration over x-axis, the positive peaks are related to the collisions, the ball increase the velocity.
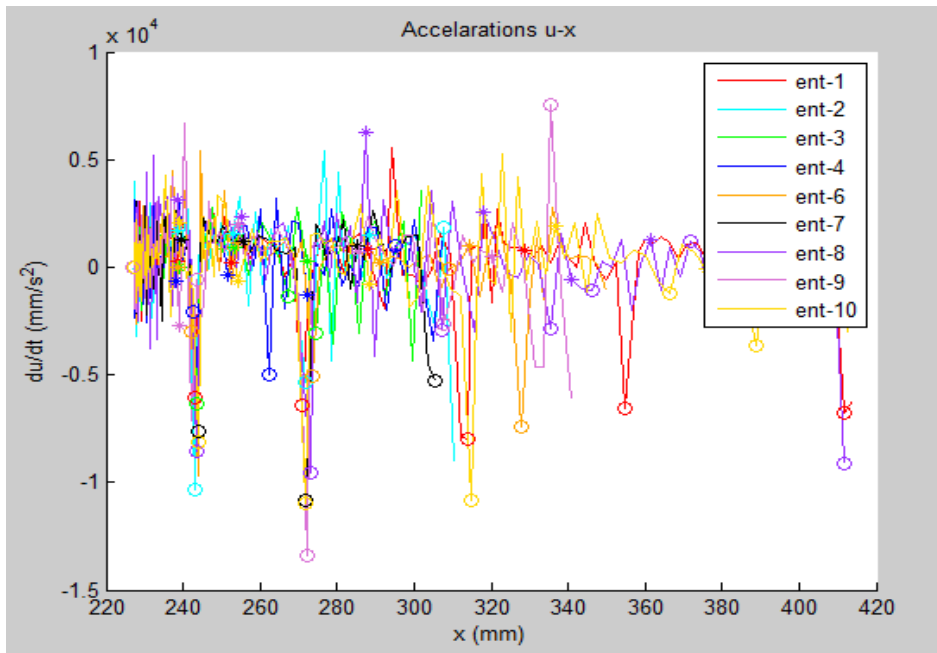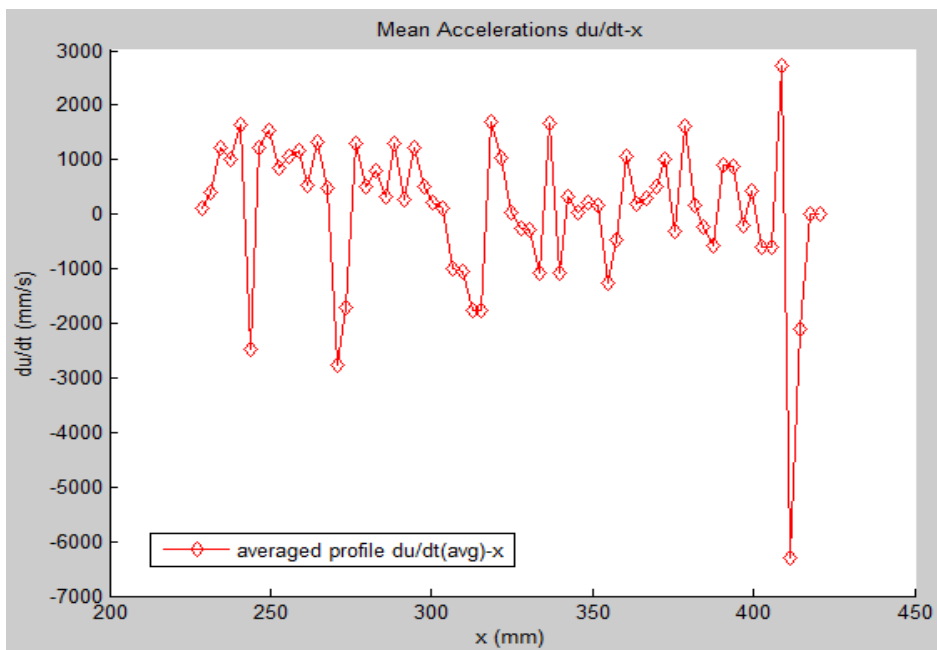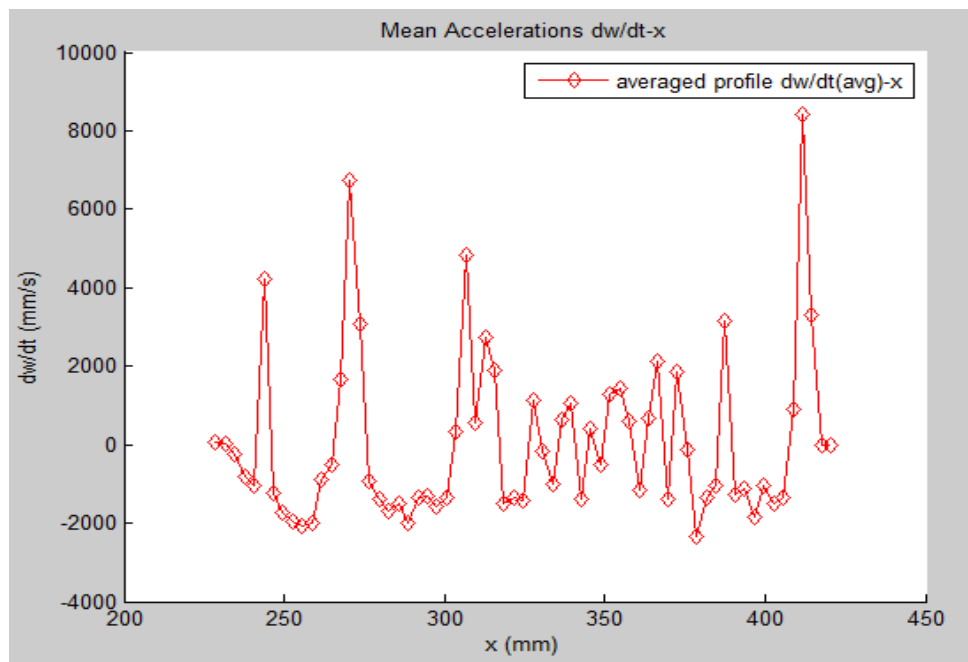

Figure 7-36 (Run A, Delrin) Graph acceleration dw/dt-x, shows w-acceleration over x-axis, the initial section doesn't show any particular behaviour related to the lift forces.

73

7.2.5. Comparisons and discussion

To describe the behaviour of the results of all the 25 entrainments per parameters setting and to try to compare these against one another, it has been summarized the general behaviour with a mean values function, choosing each time one independent variable to create bins and averaging the data related to each bin. Entrainments with more shallow water had a much higher caption frequency. In order not to have empty bins it has been chosen to enlarge the bin size for the deeper flow conditions.

As was previously stated, graphs are referring to a position's variable in order to have a better focus on the activity at the moment of entrainment; this choice involves a mean value's representation of the dependent variable. The representation is influenced by the trajectories of the particle out of the laser plane, causing the short tracking of the ball.

Looking at the x-z plane it seems that Delrin particles have the same mean position also with different flow conditions. Moreover, the Nylon ones present a higher mean position after the motion beginning. This is related to the lighter density of the Nylon that reduces the weight forces over it.
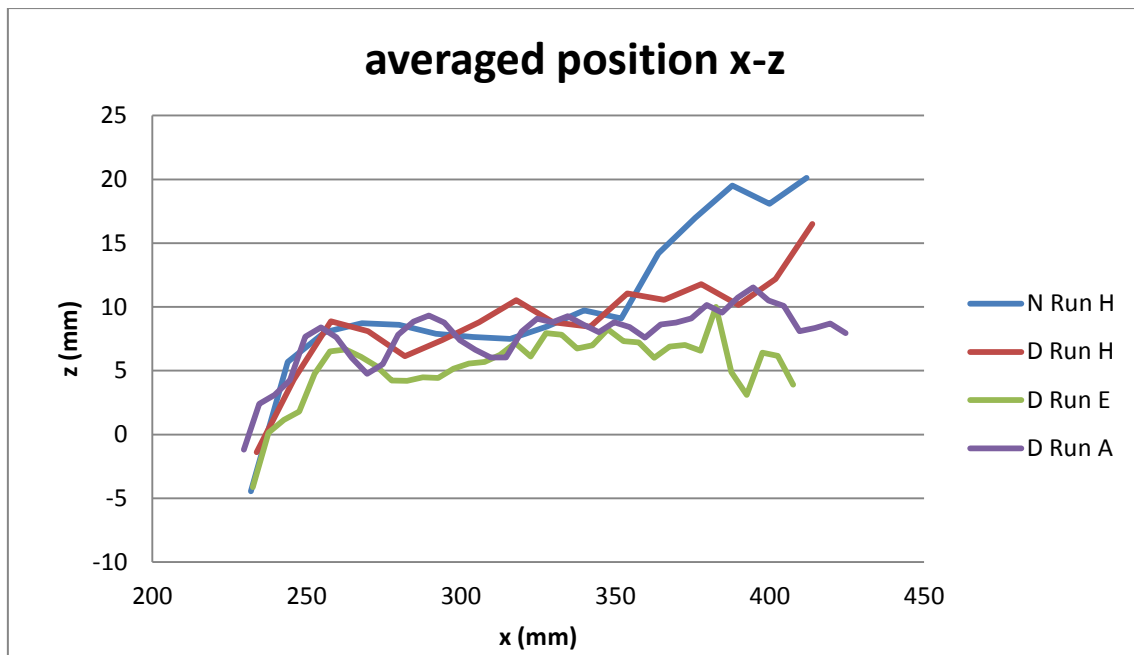
Figure 7-37 Average Graph Comparisons, position x-z, shows z-position over x-axis.

Checking the velocities it can be noticed that the stream-wise velocity is bigger with lower the flow depth. The Nylon seems to have bigger fluctuations and higher x-velocities overall, probably because of the weaker weight forces, thus the motion is more affected from the flow fluctuations. Figure 7-39 aims at showing also the ball velocity profile over the z-axis to check if there are similarities with the near bed fluid's logarithmic velocity profile. It seems so for "Run A" and "Run E", "Run H" presents more fluctuations, they are more frequent for Nylon sediment that reaches higher z-position.

There are considerably higher trajectories for lighter particle as it is showed also in the averaged u-z graph that take into consideration bins along z.
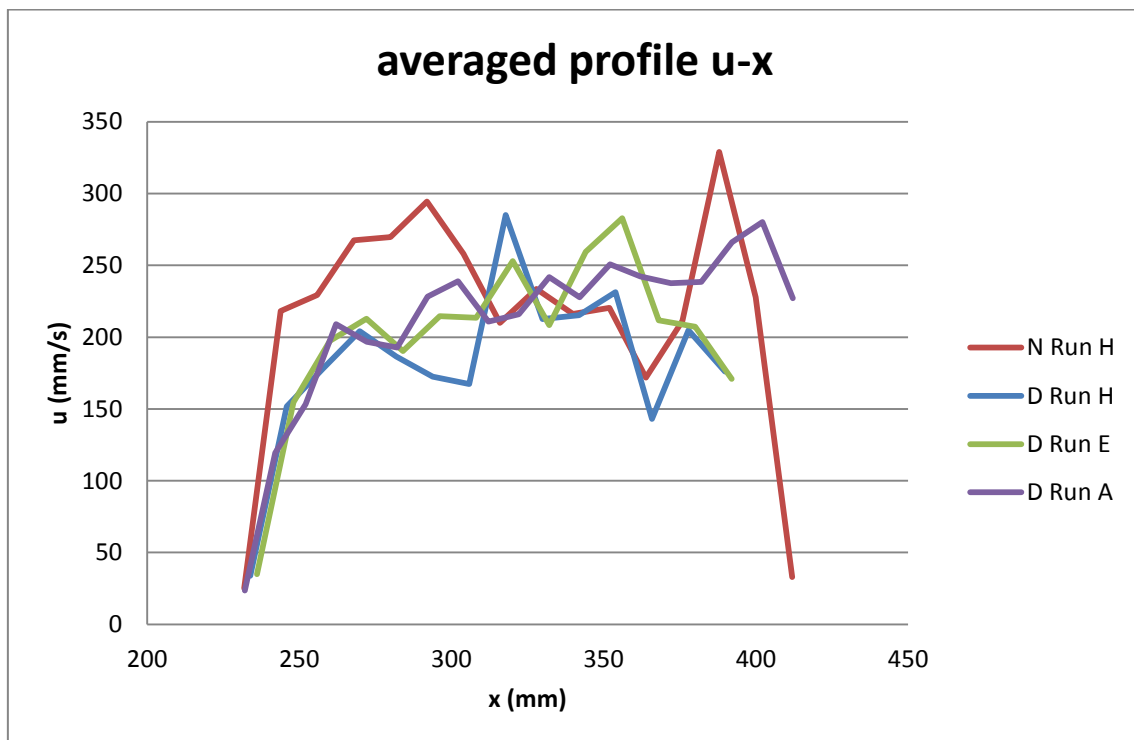
Figure 7-38 Average Graph Comparisons, velocities u-x, shows u-velocity over x-axis.
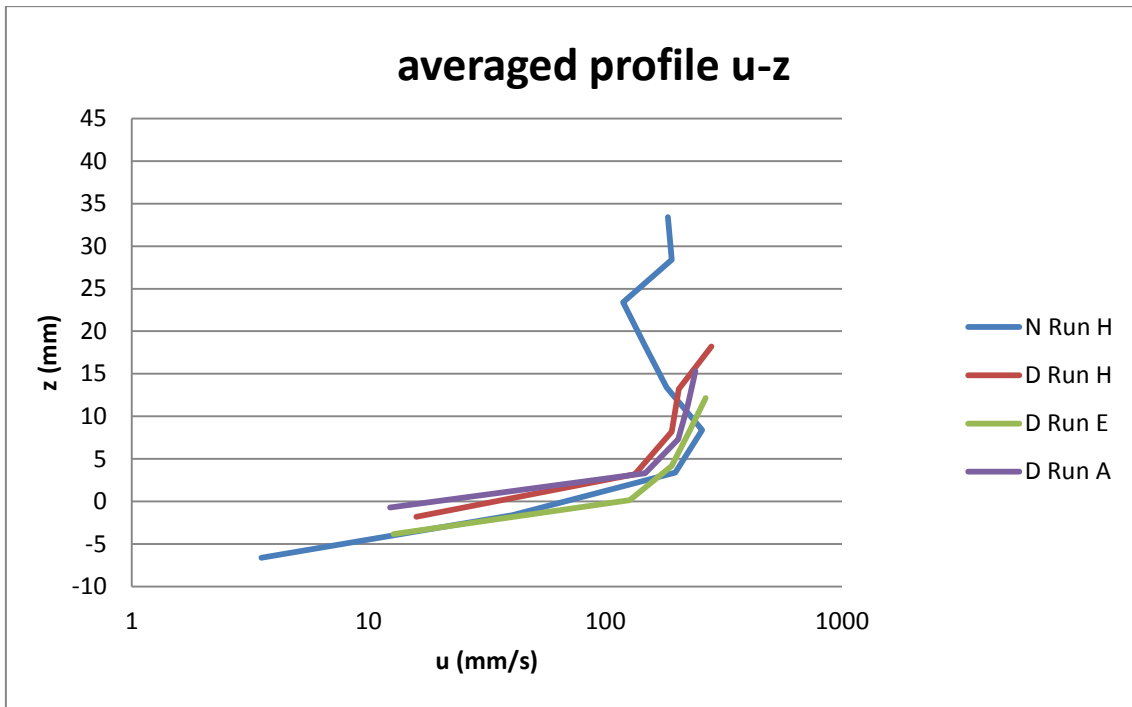
Figure 7-39 Average Graph Comparisons, velocities u-z, shows u-velocity over z-axis.

The average accelerations are important to note if there are some particular forces on the sediment at the position of the entrainment and if those can be related to a lift or drag event caused by the flow. The drag events are more intense compared to the lift ones at the point of entrainment. For deeper flow the mean magnitude of the x-accelerations at the starting point is bigger. The z-accelerations are of the same magnitude on over those flows; moreover in comparison with the previous acceleration component have small values. For lighter density the ratio between accelerations of lift and drag is increased, indeed the lighter particle was placed on the channel's bed with a lower protrusion; as a result it requires to be lifted more before being entrained by the flow. "Run E" for Delrin presents a similar ratio between the two acceleration apparently with no reason. For both, the collision events create bigger acceleration on the motion and the flow effect is not as much evident.

		x (mm)	du/dt (mm/s^2)				x (mm)	dw/dt (mm/s^2)
N	Run H	231,90	391,00		**N**	Run H	231,90	142,57
	Run H	233,84	435,75			Run H	233,84	13,31
D	Run E	232,58	246,29		**D**	Run E	232,58	125,18
	Run A	228,61	110,13			Run A	228,61	67,11

Table 7-5 Mean Accelerations at the point of entrainment, a) x-acceleration, b) z-acceleration

The big peaks at the beginning for "Run A" and "Run E" give a good idea of how much similar is the entrainment trajectory of the same parameter sets, on the other hand "Run H" has a bigger submergence and the trajectories seem to be more random already from the first moments. This is also a consequence of the larger bins used to create the graph for the deep flows, but the peaks are still lower than the ones of the others flows conditions.
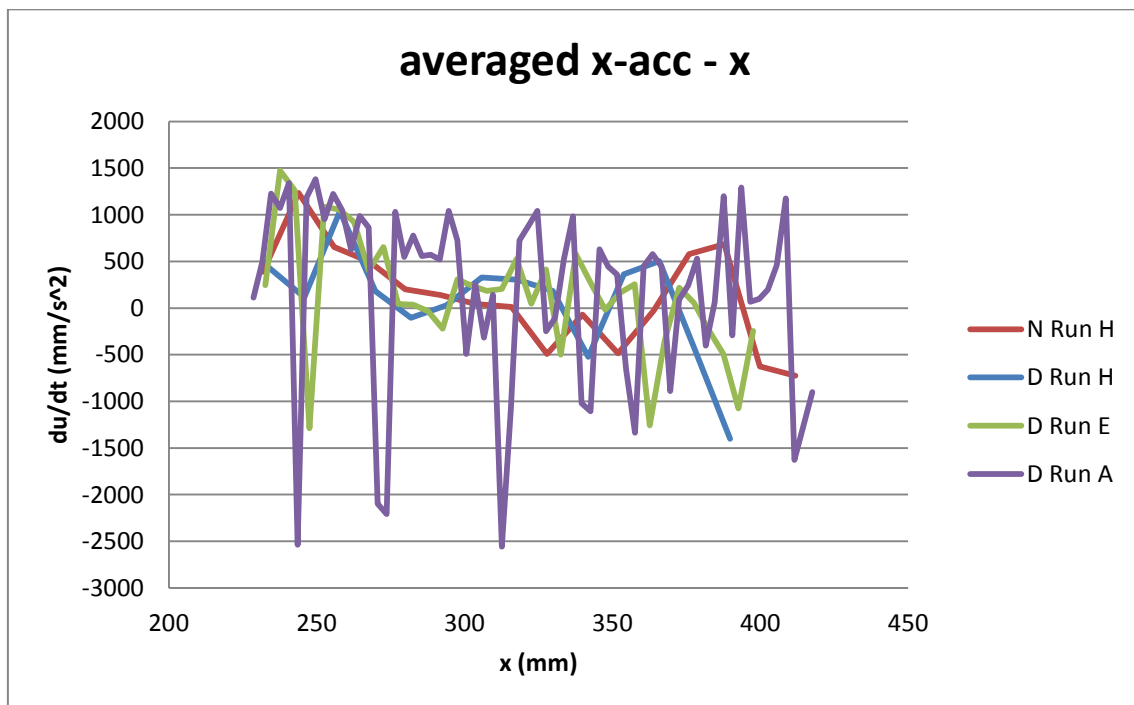
Figure 7-40 Average Graph Comparisons, accelerations du/dt-z, shows x-acceleration over x-axis.
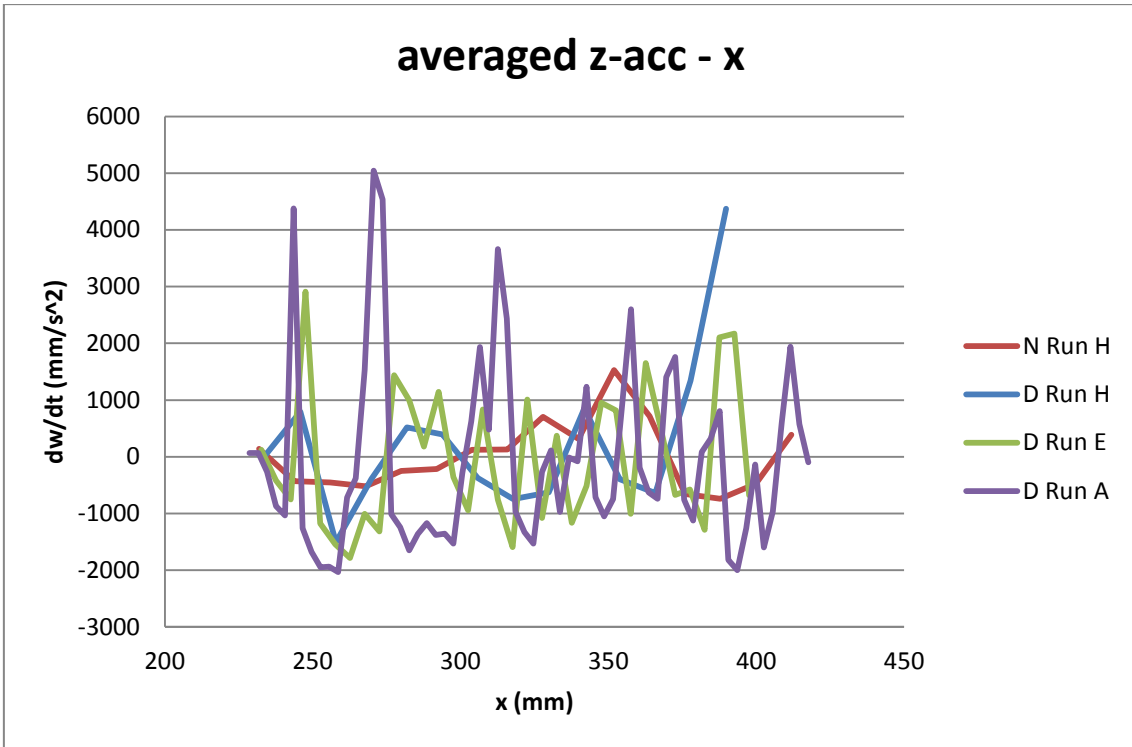
Figure 7-41 Average Graph Comparisons, accelerations dw/dt-x, shows z-acceleration over x-axis.

From the analysis of the jumps, the summary of the different parameter sets' behaviour can be taken out. For each jump detected was measured the length and the height (considered as random variables), highlighting the maximum, the mean and the standard deviation in order to describe the two random variables.

	H jump (mm)			
	N-H	**D-H**	**D-E**	**D-A**
mTot	28,55	16,25	29,17	64,10
σ**Tot**	4,78	3,64	8,02	20,63
MaxTot	37,06	27,67	49,91	124,33
Re_b	61704	61681	32310	11517
ρ_s/ρ	1,11	1,37	1,37	1,37
Max/m	1,30	1,70	1,71	1,94
m/s	7,75	7,61	6,22	6,03

Table 7-6 Jump Height Table, showing mean standard deviation and maximum values, reporting Reynolds Number and relative density, and ratio between maximum and mean value, and mean and standard deviation value.

	L jump (mm)			
	N-H	**D-H**	**D-E**	**D-A**
mTot	89,64	33,48	36,93	28,81
σ**Tot**	25,51	18,08	18,51	12,18
MaxTot	129,48	88,45	73,04	56,84
Re_b	61704	61681	32310	11517
ρ_s/ρ	1,11	1,37	1,37	1,37
Max/m	1,44	2,64	1,98	1,97
m/s	5,08	4,89	3,95	4,67

Table 7-7 Jump Length Table, showing mean standard deviation and maximum values, reporting Reynolds Number and relative density, as well ratio between maximum and mean value, mean and standard deviation value.

Under different flow conditions the jump's height is bigger with smaller depth and standard deviation follows the same trend. The maximum and mean values seem to have a non-linear trend in relation to Reynolds Number. The standard deviation shows a scattering increment for shallow flows. Moreover, the lower the Reynolds Number, the bigger the maximum height, this denote the variability increment. Moreover the jump length does not seem to suffer from these flow variations, the mean jump length remains close to 30 - 40 mm, also the standard deviation seems to remain constant, and on the other hand the maximum value shows a small increment with the flow depth.
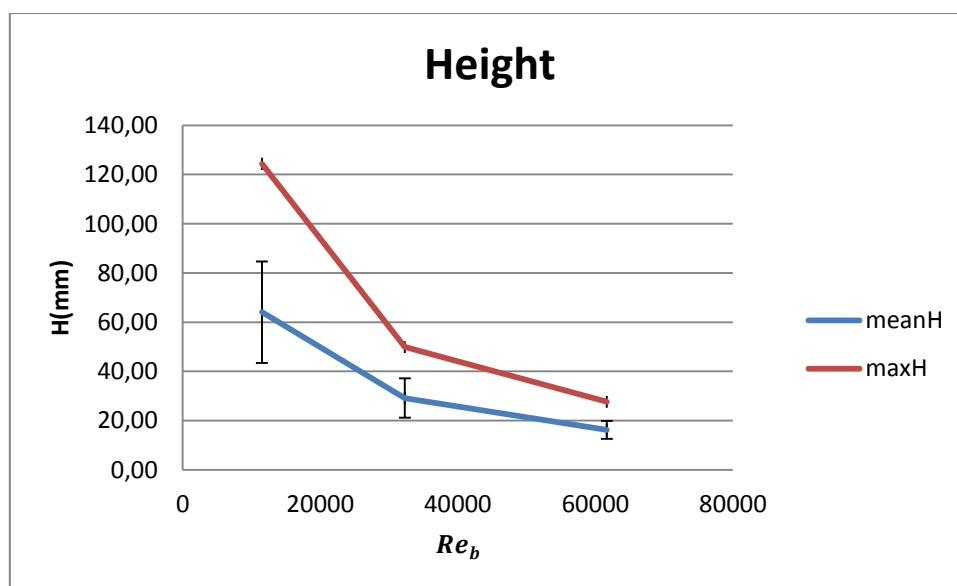
Figure 7-42 Jump Height Graph, different flow conditions, mean and maximum values.
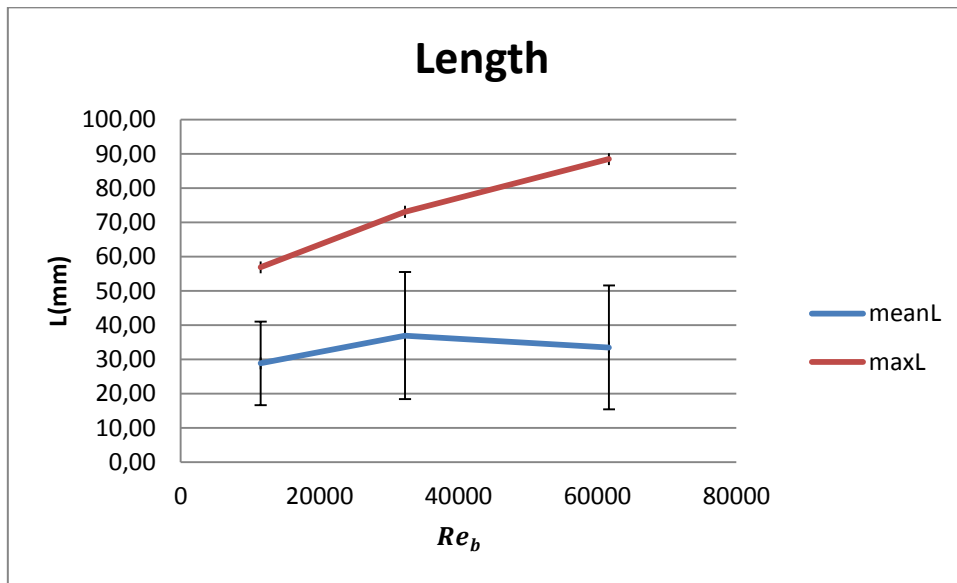
Figure 7-43 Jump Length Graph, different flow conditions, mean and maximum values.

The variation in the particle density shows a clear increment on the jumps height and length for the lighter particle, which is obviously caused by the weight force less intense. This behaviour is clearly represented by comparisons between the trajectories. The standard deviation presents a small increase with lighter particles.
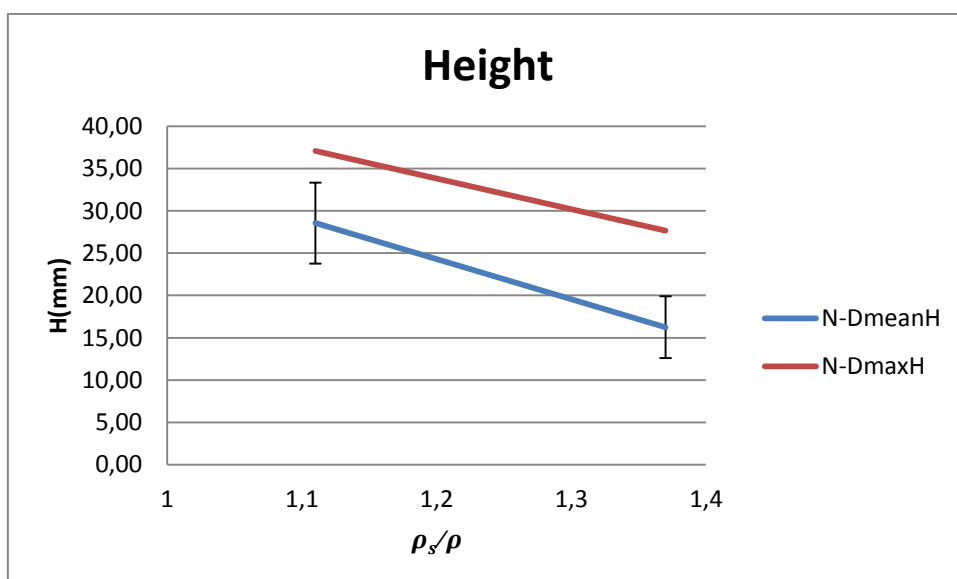
Figure 7-44 Jump Height Graph, different sediment densities, mean and maximum values.
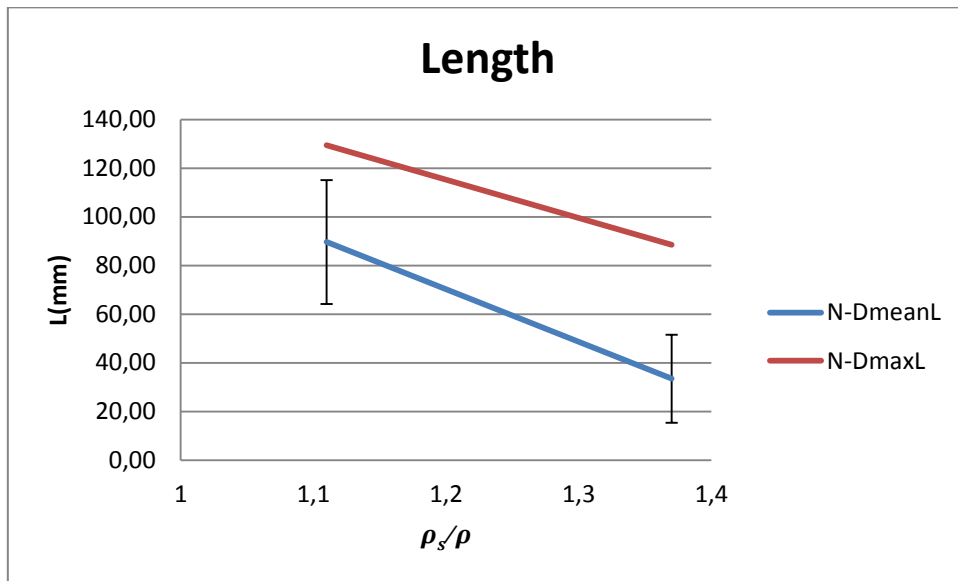
Figure 7-45 Jump Length Graph, different sediment densities, mean and maximum values.
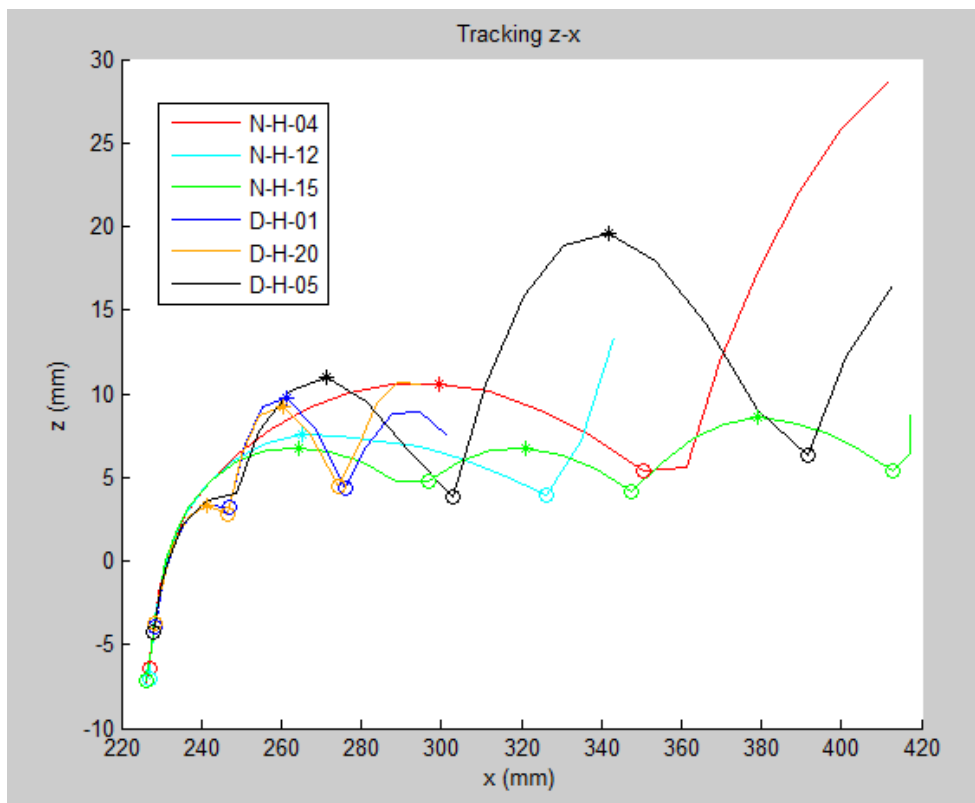
Figure 7-46 Trajectories Comparison Graph, different particle density, the Nylon jumps' shape is more stretched, the "N-H-04" last jump seems to be very high, but it's detected only in its first part, so it's not completely detected. It can be an example of the saltation motion changing into suspended particle motion due to the lower gravity forces.

8. Conclusion and suggestion

The Laboratory experiments were carried out in a rectangular section flume with spherical element on the bottom to reproduce the roughness, only one target particle was allowed to be entrained by the flow, and its motion was recorded by a PIV system for two different particle densities and three flow conditions.

The analysis on the protrusion effect and erosion mean time shows that the z-position of the particle in relation to the nearby bed's tops has a big influence on the occurrence time of entrainment, small variations of a fraction of millimeter on it can change considerably the erosion mean time, the particle density also has a main role in this as it determines the stabilizing forces magnitude (weight force). As a consequence, the magnitude of the destabilizing forces needs to present big enough values in order to move the particle from its position on the bed, hence the protrusion was increased for heavier particles. In the end also the flow condition that modifies the hydrodynamic forces has its role, but compared to the previous two the phenomenon is not so sensitive to flow rate variations. Therefore, the entrainment is more influenced by the particle proprieties as density and protrusion, which are very variable depending on a natural bed stream.

The particle tracking analysis clearly shows the influence of the particle density on the motion, lighter the particles the more stretched the jumps. So height and length of jumps are bigger, due to the less intense weight force and on the other side the more influential the flow turbulence force. After entrainment, particles tend to follow the flow behaviour, which is showed by the mean velocity profile in the near bed region, creating a sort of logarithmic profile. The particle velocity starts to increase into the downstream motion in relation to the flow condition and to the particle density that allow a big variation in the trajectories and the collision frequency.

The bed's erosion can be controlled by working on the stones of the river's bottom, developing a flat bed with heavy particles, to reduce the influence of the hydrodynamic forces, as drag and lift forces, reducing the protrusion of the bed's particles and to increase the weight forces that provide more stability over rivers bed and its stones.

Further studies can focus on the interaction between particle and flow motion, using also the PIV data related to the flow, to highlight the turbulent events at the beginning of the motion, they can also be used to check the events magnitude that influences the particle trajectories. Furthermore try to describe the probability of occurrence for those critical turbulent flow events, looking directly into the flow motion. With a large detection area it is possible to track the particle further in its way downstream to understand if it follows the flow behaviour and if it reaches stability in some motion parameters as the downstream mean velocity. This can be an indicative parameter of the particle's kinetic energy taken from the flow. Further experiments can also investigate the effect of different roughness bed arrangement on the entrainment occurrence and flow motion.

References

- ACARLAR, M.S. and SMITH, C.R., 1987. A study of hairpin vortices in a laminar boundary layer. Part 1. Hairpin vortices generated by a hemisphere protuberance. Journal of Fluid Mechanics.

- ADRIAN, R.J., MEINHART, C.D. and TOMKINS, C.D., 2000. Vortex organization in the outer region of the turbulent boundary layer. Journal of Fluid Mechanics.

- ADRIAN, R.J., 2007. Hairpin vortex organization in wall turbulence. Physics of Fluids.

- BAGNOLD, R. A., The Nature of Saltation and of Bed-Load Transport in Water.

- BOTTACIN-BUSOLIN, A., TAIT, S. J., MARION, A., CHEGINI, A., TREGNAGHI, M., 2008. Probabilistic description of grain resistance from simultaneous flow field and grain motion measurements. Water Resources Research.

- BUFFINGTON, J.M. and MONTGOMERY, D.R., 1997. A systematic analysis of eight decades of incipient motion studies, with special reference to gravel-bedded rivers. Water Resources Research.

- CAMERON, S.M., 2006. Near-boundary flow structure and particle entrainment. Ph.D., the University of Auckland.

- CANNY, J. F., 1986, A computational approach to edge detection. IEEE Transactions on Pattern Analysis and Machine Intelligence.

- CARLING, P.A., KELSE, A. and GLAISTER, M.S., 1992. Effect Of Bed Roughness, Particle Shape and Orientation On Initial Motion Criteria, Third International Workshop on Gravel-Bed Rivers 1992.

- CHEPIL, W.S., 1959. Equilibrium of Soil Grains at the Threshold of Movement by Wind. Soil Science Society of America.

- COLES, D., 1956. The law of the wake in the turbulent boundary layer. Journal of Fluid Mechanics.

- DE BOER, G.M. 1998. Transport of stones on a granular bed-protection. M.Sc. thesis, Delft University of Technology, Delft. In Dutch.

- DEFINA, A., 1996. Transverse Spacing of Low-speed Streaks in a Channel Flow over a Rough Bed. In: P.J. ASHWORTH, S.J. BENNETT, J.L. BEST and S.J. MLELLAND, Coherent Flow Structures in Open Channels. England: John Wiley & Sons Ltd.

- DETERT, M., 2008. Hydrodynamic processes at the water-sediment interface of streambeds, Ph.D., Universität Karlsruhe.

- DIPLAS, P., DANCEY, C.L., CELIK, A.O., VALYRAKIS, M., GREER, K. and AKAR, T., 2008. The Role of Impulse on the Initiation of Particle Movement Under Turbulent Flow Conditions. Science.

- DWIVEDI, A., 2010. Mechanics of sediment entrainment. Ph.D., the University of Auckland.

- DWIVEDI, A., MELVILLE, B.W., SHAMSELDIN, A.Y. and GUHA, T.K., 2011. Flow structures and hydrodynamic force during sediment entrainment. Water Resources Research

- EINSTEIN, H.A. and EL-SAMNI, E.A., 1949. Hydrodynamic Forces on a Rough Wall. Reviews of Modern Physics.

- EMMERLING, R., 1973. The instantaneous structure of the wall pressure under a turbulent boundary layer flow. Max-Planck-Institut fur Stromungsforschung.

- FENTON, J.D. and ABBOTT, J.E., 1977. Initial Movement of Grains on a Stream Bed: The Effect of Relative Protrusion. Proceedings of the Royal Society of London A.

- GIMÉNEZ-CURTO, L.A. and CORNIERO LERA, M.A., 1996. Oscillating turbulent flow over very rough surfaces. Journal of Geophysical Research C: Oceans.

- GRANT, I., 1997. Particle image velocimetry: A review. Proceedings of the Institution of Mechanical Engineers, Part C.

- GRASS, A.J., 1970. Initial instability of fine bed sand. Journal of the Hydraulics Division Proceedings of the American Society of Civil Engineers.

- HILL, R.J. and THORODDSEN, S.T., 1997. Experimental evaluation of acceleration correlations for locally isotropic turbulence, Physical Review.

- HOFLAND, B., and BOOIJ, R., 2004. Measuring the flow structures that initiate stone movement, River Flow 2004, Edited by M. Greco, A. Carravetta, and R. Della Morte.

- HOFLAND, B., BATTJES, J.A. and BOOIJ, R., 2005. Measurement of Fluctuating Pressures on Coarse Bed Material. Journal of Hydraulic Engineering.

- HOFLAND, B., 2005. Rock & Roll. Ph.D., TU Delft.

- KIM, H.T., KLINE, S.J. and REYNOLDS, W.C., 1971. The production of turbulence near a smooth wall in a turbulent boundary layer. Journal of Fluid Mechanics.

- KLINE, S.J., REYNOLDS, W.C., SCHRAUB, F.A. and RUNSTADLER, P.W., 1967. The structure of turbulent boundary layers. Journal of Fluid Mechanics.

- LAVELLE, W. & MOFJELD, H. O., 1987. Do critical stresses for incipient motion and erosion really exist? Journal of Hydraulic Engineering.

- MC EWAN, I., SORENSEN, M., HEALD, J., TAIT, S., CUNNINGHAM, G., GORING, D., WILLETS, B., 2004. Probabilistic modelling of bed-load composition. Journal of Hydraulic Engineering.

- MILLER, M.C., MCCAVE, I.N. and KOMAR, P.D., 1977. Threshold of sediment motion under unidirectional currents. Sedimentology.

- NELSON, J.M., SHREVE, R.L., MCLEAN, S.R. and DRAKE, T.G., 1995. Role of Near-Bed Turbulence Structure in Bed Load Transport and Bed Form Mechanics. Water Resources Research.

- NEZU, I. and NAKAGAWA, H., 1993. Turbulence in Open-Channel Flows. Netherlands: A.A. Balkema.

- NIKORA, V., GORING, D., MCEWAN, I. and GRIFFITH, G., 2001. Spatially averaged open-channel flow over rough bed. Journal of Hydraulic Engineering.

- NIKORA, V., MCEWAN, I., MCLEAN, S., COLEMAN, S., POKRAJAC, D. and WALTERS, R., 2007. Double-Averaging Concept for Rough-Bed

Open-Channel and Overland Flows: Theoretical Background. Journal of Hydraulic Engineering.

- NIKORA, V., 2008. Hydrodynamics of gravel-bed rivers: scale issues. Gravel-Bed Rivers VI: From Process Understanding to Restoration.
- PRASAD, A.K., 2000 a. Particle image velocimetry. Current Science.
- PRASAD, A.K., 2000 b. Stereoscopic particle image velocimetry. Experiments in Fluids.
- RADECKE, H. VAN., and SCHULZ-DU BOIS, E. O., 1988. Linear Response of Fluctuating Forces to Turbulent Velocity Components, 4th International Symposium on Applications of Laser Techniques to Fluid Mechanics.
- RAFFEL, M.,WILLERT, C. E., and KOMPENHANS, J. 1998. Particle Image Velocimetry: A Practical Guide. New York: Springer.
- SCHEWE, G., 1983. On the structure and resolution of wall-pressure fluctuations associated with turbulent boundary-layer flow. Journal of Fluid Mechanics.
- SCHMEECKLE, M.W. and NELSON, J.M., 2003. Direct numerical simulation of bedload transport using a local, dynamic boundary condition. Sedimentology.
- SHIELDS, A., 1936. Application of similarity principles and turbulence research to bed-load movement, translated from Anwendung der Aehnlichkeitsmechanilr und der Turbulenzforschung auf die Geschiebe - bewegung by Ott, W.D. and Von Vcheten, J.C. Mitteilungen der Versuchsanstalt fur Wasserbau und Schiffbau.
- SUMER, M., and DEIGAAR, R., 1980. Particle motions near the bottom in turbulent flow in an open channel. Part 2, Journal of Fluid Mechanics.
- THEODORSEN, T., 1952. Mechanism of turbulence, 2nd Midwestern Conference on Fluid Mechanics 1952, Ohio State University Press.
- VAN RIJN, L. C., 1984. Sediment transport. Part I: Bed load transport. Journal of Hydraulic Engineering.
- WILLERT, C.E. and GHARIB, M., 1991. Digital particle image velocimetry. Experiments in Fluids.

- WILLMARTH, W.W. and LU, S.S., 1972. Structure of the Reynolds stress near the wall. Journal of Fluid Mechanics.
- WILSON, N.R. and SHAW, R.H., 1977. A higher order closure model for canopy flow. Journal of Applied Meteorology.
- XINGKUI, W. and FONTIJN, H.L., 1993. Experimental Study of the Hydrodynamic Forces on a Bed Element in an open Channel with a Backward-Facing Step. Journal of Fluids and Structures.
- ZANKE, U. C. E., 2003. On the influence of turbulence on initiation of sediment motion. International Journal of Sediment Research.

Appendix A. - PIV - Particle detection

The particle detection was performed with an intensity-gradient technique Canny Edge Detector (Canny, 1986). This method looks at the gradient of the pixel in the images checking for edges with a maximum intensity-gradient. Firstly, it uses a Gaussian blur to reduce the noise of the image, looking for the vertical and horizontal gradient, the two information can be combined to get the intensity-gradient magnitude and direction of each pixel and considering only those above a threshold value. The edges composed of those pixels are filtered considering only pixels with maximum gradient on the edge direction, obtaining this way edges of one pixel wide (Non Maximum Suppression). The final step is to remove the lower edges of the ball, those are usually caused by the bed layer before entrainment.
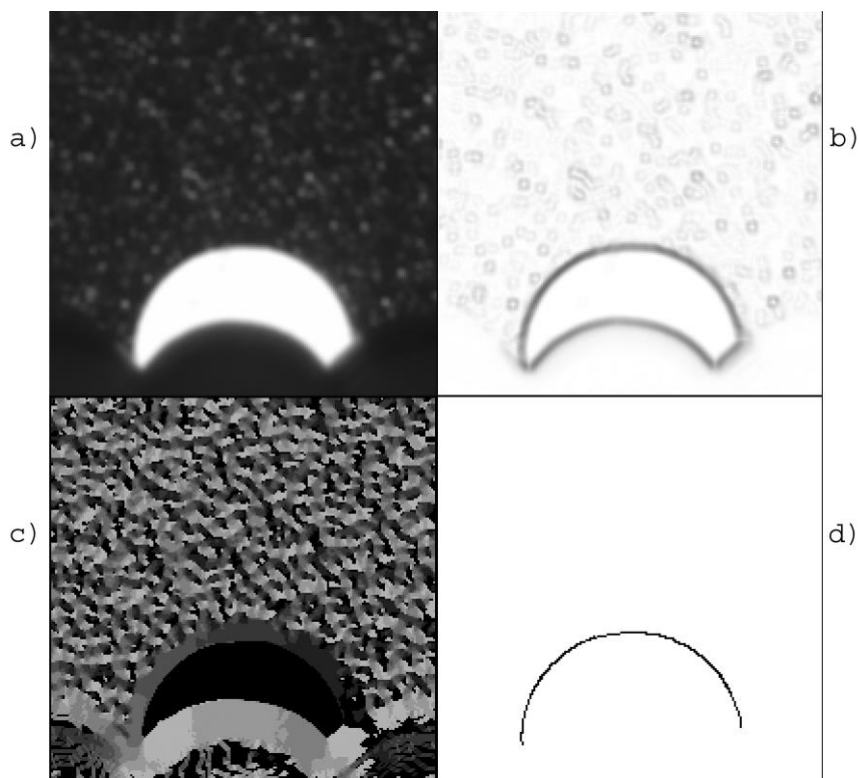

*Figure A-1 (Cameron, 2006),*Canny Edge Detector method: (a) Gaussian Blur, (b) Intensity-gradient Magnitude, (c) Intensity-gradient Direction, (d) Non Maximum Suppression

The edges of the ball are located by the main directions up, down, right, left and their four combinations in diagonal, numbered from 0 to 7 from the top in a clockwise direction. In relation to the analysed camera images the laser system lights only one side of the particle, for this reason focusing the detection only on few edges can be considered a good solution. The detection is carried out only by the top edges of one side of the ball usually 0-1-2 for camera 2 and 0-7-6 for camera 3. This is enough to locate automatically a circle with his center and radius.

Appendix B. - Kolmogorov-Smirnov Test

The Kolmogorov-Smirnov test is a non-parametric test that verifies the samples distribution shapes and can be applied to ordinal dataset. It can be used to compare a sample distribution $F_1(x)$ to a theoretical one $F(x)$ or to compare two sample distributions $F_1(x)$ and $F_2(x)$.

The test checks if the Cumulative Density Functions $F_1(x)$ and $F_2(x)$ can be the same, i.e. if they belong to the same distribution $F(x)$. The test hypotheses are:

$$H_0: \ F_1(x) = F_2(x), \ \ \forall \, x$$

$$H_1: \ F_1(x) \neq F_2(x)$$

Having to estimate the CDF, it is required a good estimator for carrying out the test. For this reason empirical CDFs $F'_1(x)$ and $F'_2(x)$ are created from the samples and later analysed. This function is created from the sample frequencies for every value of the random variable X of the sample $(X_1, \dots, X_n)$.

$$F'(x) = \frac{1}{n} \sum_{i=1}^{n} I_{X_i < x}$$

Where:

$I_{X_i < x}$ = indicator function, equal to 1 if $X_i < x$, 0 otherwise.

The maximum difference between the two estimators is the statistic test, if it is too big the H_0 hypothesis is refused; otherwise, it is accepted. The comparison is made with $c(\alpha)$, its values are tabulate for the test in relation to the degree of reliability α, usually with the value of α=0.05.

$$D_n = sup|F'_1(x) - F'_2(x)|$$

H_0 rejected for $D_n > c(\alpha)$.

Appendix C. - Central Finite Difference

A finite difference is the difference between two function values calculated into two finite points of the independent variable. It is very useful to divide the finite difference by the distance between the two points of the independent variable, it gives an approximation of a derivate. This computation has a main role in the finite difference method. It is used to solve differential equations by numerical approximation.

In partial differential equations, derivatives are approximated by a linear equation with the function values calculated at specifics points. Considering a first order derivatives we can write by definition the following:

$$f'(x) = \lim_{\Delta x \to 0} \frac{f(x + \Delta x) - f(x)}{\Delta x}$$

$$f'(x) = \lim_{\Delta x \to 0} \frac{f(x) - f(x - \Delta x)}{\Delta x}$$

$$f'(x) = \lim_{\Delta x \to 0} \frac{f(x + \Delta x) - f(x - \Delta x)}{2\Delta x}$$

The approximation of those derivatives can be developed using the finite difference method referring to specific values of the function calculated into specific points x_i. If the difference between the independent values Δx is constant we can further simplify.

Forward difference $\qquad f'(x_i) \approx \dfrac{f(x_{i+1}) - f(x_i)}{x_{i+1} - x_i} = \dfrac{f(x_{i+1}) - f(x_i)}{\Delta x}$

Backward difference $\qquad f'(x_i) \approx \dfrac{f(x_i) - f(x_{i-1})}{x_i - x_{i-1}} = \dfrac{f(x_i) - f(x_{i-1})}{\Delta x}$

Central difference $\qquad f'(x_i) \approx \dfrac{f(x_{i+1}) - f(x_{i-1})}{x_{i+1} - x_{i-1}} = \dfrac{f(x_{i+1}) - f(x_{i-1})}{2\Delta x}$
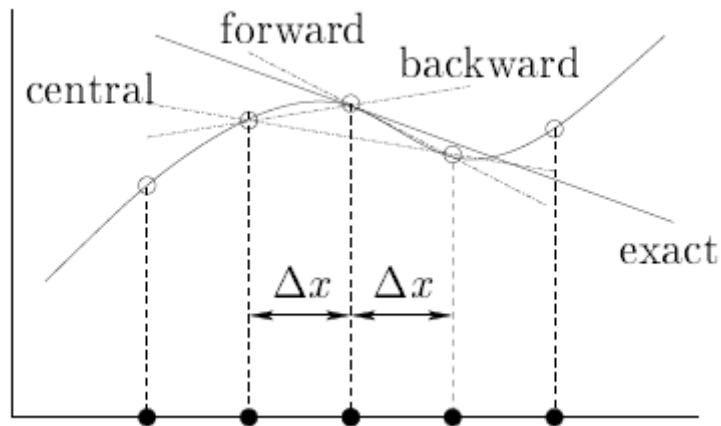
Figure C-1 Geometrical interpretation of the finite difference method

Considering the expansion in Taylor series for the analysed function, they show the error committed by the approximation:

$$f(x_{i+1}) = f(x_i) + \Delta x f'(x_i) + \frac{\Delta x^2}{2!} f''(x_i) + \frac{\Delta x^3}{3!} f'''(x_i) + \cdots$$

$$f(x_{i-1}) = f(x_i) - \Delta x f'(x_i) + \frac{\Delta x^2}{2!} f''(x_i) - \frac{\Delta x^3}{3!} f'''(x_i) + \cdots$$

The error for the central finite difference method is smaller than for the other two. Also, some problems can occur with it in analysing an oscillating discrete function that can bring the derivate to zero.

$$f'(x_i) = \frac{f(x_{i+1}) - f(x_i)}{\Delta x} - \frac{\Delta x}{2!} f''(x_i) - \frac{\Delta x^2}{3!} f'''(x_i) + \cdots \Rightarrow Er = \mathcal{O}(\Delta x)$$

$$f'(x_i) = \frac{f(x_{i+1}) - f(x_i)}{\Delta x} + \frac{\Delta x}{2!} f''(x_i) - \frac{\Delta x^2}{3!} f'''(x_i) + \cdots \Rightarrow Er = \mathcal{O}(\Delta x)$$

$$f'(x_i) = \frac{f(x_{i+1}) - f(x_{i-1})}{2\Delta x} - \frac{\Delta x^2}{3!} f'''(x_i) + \cdots \Rightarrow Er = \mathcal{O}(\Delta x^2)$$